Fibre Optic Sensors Interrogation by Interferometric Illumination

Shivasiddharth Uma (No W20072819)

Department of Engineering Technology

Waterford Institute of Technology

Thesis submitted for the award of degree of

Doctor of Philosophy

Supervisors

Dr Kieran O'Mahoney, Dr Ken Thomas, Dr James Kennedy

Submitted to Waterford Institute of Technology, May 2020

Declaration

I hereby declare that no part of the work described in this thesis has ever been submitted for an award of a degree either in this institution or any others. The work described in this thesis has been entirely performed by the author of this document.

Shivasiddharth Uma

May 2020

Acknowledgements

First and foremost, I would like to thank all the gods, ancestors and my Sadguru Shirdi Sai Baba for keeping me in good health, shape and frame of my mind all these years and this really helped me to focus and concentrate on my work.

Would like to take this opportunity to express my sincere gratitude and thank my supervisor Dr Kieran O'Mahoney for all his training, guidance, and support without which I could not come this far. Also, I would like to thank my co-supervisors Dr Ken Thomas and Dr James Kennedy for their constant and invaluable support throughout my PhD. Would like to thank Dr David Goulding, who acted as the examiner for the transfer from Masters to Doctorate register for his advice, suggestions and insights on the work performed. Also, I would like to thank Dr Philip Walsh, Dr John Houlihan, Mr Frank and other fellow members of CTRG and Optics Research Group for their support all through these years.

Would like to thank Mr Robert Volkamp from Process & Instrumentation Products for helping me with the parts required for setting up the aged fibre workstation. Words fail to describe my gratitude to WIT (where I have spent more time than my home over the last four and a half years) for providing me with this platform. Would also like to thank the Head of the Department of Engineering, the Office of School of Engineering, International Students' Office, the Research Support Unit, and the Postgraduate Support Unit. The porters of WIT need a special mention for helping me at instances when I have gotten locked out of my lab.

Would like to thank Amma and Appa for giving me this life and raising me by always giving the best of what they could. Credit for what I am today partly goes to them and a vast majority to my thatha Pitchan. Even though he is not with me today, I will always have his grace and blessings. Heartfelt thanks to Bajjuma and MLA for co-raising me and for being my second set of parents. Would like to thank Sundarima and Dada for their prayers and for showering all their love and well wishes. These four people have played pivotal roles and have been an integral part of my life all these years. Would also like to thank Bhunima for her prayers.

Out of words for Vinod. Spent my entire childhood with him, and he was my partner in crime as I grew up. Really thankful for all his pooja, prayers and selfless affection and love. Thanks to Harish, the first engineer and doctorate holder of our family for his support during the initial stages of my PhD. Thanks to the only Akka and Athimber, all the Annas and Mannis, for their love towards this Kadaikutty Singam. Would also like to thank my wife Harini for her love and for bearing the brunt of my mood swings towards the end of my PhD. Loads of love to the kids of the family starting from Smrithi (she isn't a kid now) and Sashu to Prasidha.

This section would be incomplete without the mention of my friends Shruthi, Gopi and Purni. They have been with me for the last 25 odd years and are the go-to guys for me. Thanks to my friend Sai Prasad for all his emotional support. Siga Naveen also needs a mention here for the memorable time he has given me over the phone and in-person.

List of Publications

Sections of work reported in this thesis have previously been presented as lectures at conferences and have been published in the conference proceedings. The details of conferences, presentations and publications are as follows.

Conference presentations:

IEEE Sensors 2017, Glasgow

IEEE Sensors 2018, New Delhi

Publications:

[1] S. Uma, K. T. O'Mahoney, and K. Thomas, "Interrogation of fiber Bragg grating arrays by illumination using a low coherence interferogram," in *2017 IEEE SENSORS*, Glasgow, 2017, pp. 1–3.

[2] S. Uma, K. T. O'Mahoney, K. Thomas, and J. Kennedy, "Simultaneous Interrogation of Multiple Tapered Fiber Optic Sensors by Interferometric Illumination," in *2018 IEEE SENSORS*, New Delhi, 2018, pp. 1–4.

Abstract

With the conventional interrogation methods, multiple fibre Bragg gratings (FBG) with similar wavelengths cannot be interrogated simultaneously and, at the most one tapered sensor (TS) can be interrogated in a single scan. This drawback is overcome by interferometric illumination of optical sensors and by interrogating the sensor modulated interferograms. The capability and the efficacy of the different optical fibre sensor classes' interrogation by interferometric illumination and coherence filtering is investigated in this thesis using an all-fibre interferometer. The use of dedicated photodiodes for the interferometer's measurement arms ensures independent processing of the interferograms from the different sensors and sensor classes without spectral overlap. When interrogating multiple arrays of multiple FBGs by interferometric illumination, the sensors subjected to a temperature test demonstrated a ~9pm/^{0}C temperature response, typical of an FBG. The experiment also demonstrated the interrogation of FBGs with similar wavelengths across multiple arrays without spectral overlap. Interferometric interrogation of the TS provides for measurements using both the temporal and spectral fringes. Measurements from processing of the sensor's temporal fringes were found to have a higher accuracy than the ones obtained by processing of the spectral fringes as in the case of an optical spectrum analyser (OSA). Multiple tapered sensors used for sensing glucose solution concentration changes yielded sensitivity values of ~(3.0±1.4)e-7/ppm and ~(5.2±2.3)e-7/ppm, demonstrating the capability and efficacy of the system to interrogate multiple tapered sensors simultaneously even under conditions of reduced spectral fringe visibility unlike an OSA, which uses only the spectral fringes for measurements. Simultaneous interrogation of multiple FBGs and a TS without spectral overlap demonstrated the multi-class sensor interrogation capability of the interferometric illumination scheme. The TS's response to ethanol evaporation and an FBG's temperature response were found to be in concurrence with the respective sensor's typical behaviour.

Table of Contents

List of Figures

List of Tables

List of Abbreviations

AOM	Acoustic-Opto Modulator
AWG	Arrayed Waveguides
BBS	Broadband Source
CFBG	Chirped Fiber Bragg Grating
CMT	Coupled Mode Theory
DC	Direct Current
EM	Electromagnetic
FP	Fabry-Pérot
FPIS	Fabry–Pérot Interferometric Sensor
FFT	Fast Fourier Transform
FBG	Fibre Bragg Grating
FOIS	Fibre Optic Interferometric Sensors
FOS	Fibre Optic Sensors
FTIR	Fourier Transform Infra-Red Spectroscopy
FTS	Fourier Transform Spectroscopy
FSR	Free Spectral Range
FSI	Frequency Shifted Interferometry
FWHM	Full Width at Half-Maximum
HTT	Hilbert Transform Technique
PZT	Lead Zirconate Titanate
LPFBG	Long Period Fiber Bragg Grating
MI	Michelson Interferometer

MZI	Mach-Zehnder Interferometer
MZIS	Mach–Zehnder Interferometric Sensor
NA	Numerical Aperture
OPD	Optical Path Delay
OSA	Optical Spectrum Analyser
PPLN	Periodically Poled Lithium Niobate
PFS	Piezo Fibre Stretcher
RIU	Refractive Index Unit
SNR	Signal to Noise Ratio
SLED	Superluminescent Diode
TFOS	Tapered Fibre Optic Sensor
TIS	Tapered Interferometric Sensor
TS	Tapered Sensor
TFBG	Tilted Fibre Bragg Grating
TDM	Time Division Multiplexing
TIR	Total Internal Reflection
TE	Transverse Electric
TM	Transverse Magnetic
TLS	Tunable Laser Source
UV	Ultraviolet
WDM	Wavelength Division Multiplexing

Chapter 1

Introduction

1.1 Background

Fibre optic sensors are optical fibre devices in which the light propagating within is stimulated in response to one or more measurand fields. Fibre optic sensors in general pose numerous advantages such as, immunity to electromagnetic interference, passiveness, intrinsic safety, ease of multiplexablity. The use of optical fibre sensors has been demonstrated for a number of different applications such as sensing temperature [1]–[3], strain [4]–[6], pressure [7]–[9], gases [10]–[12], refractive index [13]–[17], structural health [4]–[6], etc. There are a number of different fibre optic sensor classes classified based on their structure and mode of operation.

With a focus only on two fibre optic sensors, namely the fibre Bragg grating (FBG) sensor and the tapered fibre optic sensor (TFOS), simultaneous interrogation of sensors from diversified classes is investigated in this thesis, using the interferometric illumination technique.

An FBG sensor when illuminated with a broadband of light, reflects a narrow band of light characteristic to it. FBG sensors are primarily sensitive to strain and temperature. However, they can be used for sensing applications involving other manifestations of the primary parameters such as acceleration, pressure, etc. Due to the typical narrow band of the sensor, the FBGs can be wavelength division multiplexed (WDM) and the small footprint of the sensor enables them to be embedded in structures for structural health monitoring applications.

TFOS is another class of fibre sensor which is fabricated by stretching a fibre whilst heating it to a temperature close to the melting point of the fibre. Sensing using a TFOS is based on the interaction of the evanescent field emanating from the tapered section of the sensor with the surrounding medium. The evanescent wave based TFOS is a modal Mach-Zehnder interferometer (MZI) typically used for sensing refractive index changes [13]–[17] due to its inherent sensitivity to the medium surrounding the sensor. Unlike an FBG, the TFOS takes up the entire bandwidth of the illuminating source, thereby limiting the number of sensors that can be multiplexed.

Fibre optic sensors' appropriate interrogation methods are decided typically based on the sensor type and the measurement requirements. For instance, the FBG sensors are interrogated using tunable filters [18], [19], a tunable laser [20], arrayed waveguides [21]–[23], Fourier transform spectroscopy [24], [25], time division multiplexing method [26], [27], frequency shifted interferometry [28], etc.

However, for commercial or industrial applications, the preferred method of interrogation has been using tunable lasers and tunable filters due to faster scanning rates, picometer resolutions and the ease of packaging of the systems. Interrogation using tunable lasers is limited by the tuning speed of the laser over the tunable wavelength range [29]. The commercially available tunable laser systems have a scanning speed of ~40-130nm/s for a maximum range of ~100nm [30]–[32]. For achieving faster scanning rates, the scanning range and resolution is reduced as in the case of [33] where, the range is reduced to 32nm and resolution is set to 8nm for nanosecond level interrogation. However, reduction in the scanning range reduces the number of FBGs that can be cascaded. The tunable filter based systems on the other hand suffer from limited optical throughput.

As with the FBGs, several methods of TFOS interrogation have been demonstrated using, optical spectrum analyser (OSA) [34], [35], spectrometer or a component test system [16], [36], [37], combination of a photodiode and an oscilloscope [38]–[40].

Commercial or industrial sensing applications have tended to favour TFOS interrogation using an OSA due to the ease of setup and operation. However, limitations of interrogation using an OSA are, it yields only the spectral information of the source and monochromator based OSAs have lower optical throughput at higher resolutions due to the presence of slits. Moreover, interrogation of sensors using a single OSA do not facilitate the interrogation of multiple sensors simultaneously as, TFOS takes up the entire bandwidth of the illuminating source and the multiplexing of sensors result in spectral overlap. Thus, for interrogating multiple tapered sensors simultaneously without spectral overlap, multiple OSAs are required, which thereby increases the overall cost of interrogation per sensor.

The tapered and the FBG sensors have varied operational principles and sensing mechanisms. Interrogation schemes are not capable of accommodating multiple sensing schema due to bandwidth limitations and the interrogation of sensor networks with multiple sensor classes require multiple interrogation units which increases the overall cost of installation significantly. Hence, sensing systems typically consist of only one class of a sensor.

When compared to other interrogation methods, interferometric interrogation of the two optical sensor classes presents key advantages over other interrogation schemes. Interferometry, typically implemented as Fourier transform spectroscopy (FTS) offers the Fellgett advantage [41], the Jacquinot advantage [42] and the Connes advantage [43], which are explained in Section 2.10.3. All-fibre based interrogation schemes have demonstrated the interrogation of FBGs and TFOS capitalising on the inherently fibre based nature of the sensor itself [25], [44]–[46]. However, conventional interferometric interrogation methods have tended to illuminate the sensors prior to interrogation by the interferometer, thereby limiting the interrogation capability to similar type constraints associated with alternative techniques like OSA, etc., where a single array of wavelength division multiplexed (WDM) FBGs and a solitary TFOS can be interrogated by a single unit.

In the work reported in this thesis, simultaneous interrogation of multiple sensor classes in a single network using optical interferometric illumination is investigated. For the purposes of work, the capability and the subsequent efficacy of the interrogation of multiple arrays of both the FBG and the tapered sensors by optical interferometric illumination is independently investigated. The work is then further developed to incorporate both the sensor classes in a single network and the capability, and the efficacy of the interrogation scheme is then investigated.

1.2 Problem definition

The interrogation of fibre optic sensors presents challenges on numerous fronts such as, the cost of the interrogator, individual cost of the sensor, sensor bandwidth of the interrogating unit, etc. An OSA is the most used tool for interrogating fibre optic sensors. However, using an OSA, at the most one array of WDM FBGs can be interrogated. As a result, commercially or industrially, tapered sensors are interrogated using an OSA and arrays of FBG sensors are interrogated using a tunable filter based system. Over the last decade, due to technological advancements, the cost of fibre optic sensors has considerably reduced, but the cost of interrogation systems has however remained high.

Both a monochromator based OSA and a tunable filter based system, suffer from reduced optical throughput. This can be overcome by using interferometry which offers the Jacquinot or higher throughput advantage [42]. Also, unlike an OSA which yields only the spectral information of the sensor, interferometry provides for measurements using the sensor's temporal information as well as the spectral information which can be obtained from the temporal information as per *Wiener–Khinchin theorem* using FTS which is a form of implementation of interferometry [47].

In a typical FTS based interrogation system, one or more sensors are first illuminated with a broadband light source and the light modulated by the sensors is then used to illuminate the interferometer for generating the interferograms which when processed yields the measurement results. This configuration does not permit the interrogation of FBGs with similar wavelengths and multiple TFOS due to spectral overlap. Also, multiple sensors belonging to different classes cannot be interrogated in the same network using FTS due to the overlapping spectrum of the sensors. In addition, with the conventional interrogation systems, the number of FBGs that can be multiplexed is limited when used in conjunction with a tapered sensor due to sensor bandwidth limitations. In the previous instances involving multiple sensor class interrogation [48]–[57], an OSA was used for the interrogation of the sensors. This resulted in a spectral overlap and complex algorithms had to be developed to disseminate the sensor results.

Existing interrogation schemes capable of simultaneously interrogating multiple sensor classes costs tens of thousands of euros. Thus, a lack of a low-cost interrogation unit capable of interrogating: multiple arrays of WDM FBG sensors, multiple TFOS in a single network and multiple sensors of multiple classes in a single unified network is evident.

The existing limitations mentioned above can be overcome by the rearrangement of the position of the interferometer in an optical fibre sensing setup. Illuminating the interferometer first with a broadband light source yields a low coherence interferogram. Then by illuminating the sensors or sensor arrays with the low coherence interferogram of the interferometer and by using dedicated photo diodes for each of the sensing arms or arrays to capture the light modulated by the sensors, multiple arrays of WDM sensors, multiple sensors of same class and multiple sensors of multiple classes can be simultaneously interrogated by coherence filtering. By using dedicated photodiodes for the sensor classes, the number of FBGs that can be multiplexed is not limited by the tapered sensor bandwidth.

Hence, the broader or primary research goal defined is to investigate the capability and the efficacy of simultaneously interrogating multiple sensor types within the same sensing network by interferometric illumination. Research goals leading up to the primary research goal include: the investigation of the capability to interrogate multiple arrays of multiplexed fibre Bragg grating sensors by interferometric illumination, the investigation of the capability and the efficacy of interrogating one and subsequently, multiple tapered sensors by interferometric illumination (also to study the interrogation system’s scalability).

Achievement of the research goals will establish the capability and the efficacy of a unified low-cost portable all-fibre interrogation unit. Portable and low-cost interrogation systems capable of interrogating multiple sensor classes can benefit studies which require simultaneous monitoring of a number of different sensors and sensor classes. With fibre optic sensors gaining popularity in fields such as bio-sensing, structural health monitoring, etc., such an interrogation system can help increase the sample space and reduce testing times as multiple sensors can be simultaneously interrogated.

1.3 Research methodology, objectives and scope

First, a study of the literature on the interrogation of an FBG sensor, TFOS, and a combination of both was made to determine the state-of-the-art in the interrogation of the different sensor classes. Following on, principles of interferometry and Fourier transform spectroscopy were also studied.

Further, bulk optic and fibre optic testbeds were constructed to evaluate the sources of errors and noises, assess the system's hardware capabilities, refine the data capturing and processing practices, study the efficacy of delay calibration, etc.

The operational principle of an FBG sensor was examined by interrogating the sensor using the constructed testbeds. Different windowing techniques were examined for optimum apodization of the FBG peaks. To optimise the interrogation performance, potential sources of reference were examined which included an FBG, a tunable filter and a narrow linewidth telecommunications laser with the wavelength centred at 1550nm.

The operational principle and the characteristics of a tapered sensor were examined by fabricating sensors with varied dimensions on a Fiber Coupler Production Workstation (FCPW) and by characterising them using ethanol vapour at room temperature whilst being interrogated using an OSA. Refractive index measurements using TFOS were obtained as a function of change in phase of the sensor's spectrum. TFOS with lower free spectral range (FSR) were found to have a higher sensitivity when compared to the TFOS with higher FSR.

After gaining operational knowledge on the different fibre optic components, an all-fibre interferometer was constructed for interferometric illumination of the sensors. The heart of the interferometer is a piezo fibre stretcher used for generating the path delay. The range of the stretcher was investigated using a high coherent laser source.

Following the review of literature and the initial experiments conducted, the primary aim was to evaluate the capability and the efficacy of the interferometric illumination technique to interrogate an array of FBG sensors. The sources of error and losses such as back reflections, spectral overlap, coupling issues, attenuation, etc., that may arise from the propagation of light and system hardware related losses or errors such as gain-bandwidth of detector, modulating frequency of fibre stretcher, etc., were investigated.

Subsequently, the interrogation technique was applied to the interrogation of multiple arrays of FBG sensors with sensors of similar or overlapping wavelengths across different arrays. Using this technique, the FBGs with similar wavelengths were clearly resolvable, facilitated by the dedicated photodiodes for each of the sensor arrays. The photodiodes were found to have a limited bandwidth at extremely high gain settings due to the Gain-Bandwidth product factor. This resulted in only a segment of the sensors' Gaussian envelope being recorded. Upon reducing the gain, the entire envelope was obtainable as discussed in Chapter-3. When FBG sensors from different sensing arrays were simultaneously subjected to a temperature test, the results were found to be in line with the typical FBG sensor's values. This demonstrated the simultaneous interrogation of multiple arrays of multiple FBG sensors.

An FBG sensor is typically interrogated in the reflection mode and a TFOS in the transmission mode. Hence, the sensing arms of the interrogator were rearranged to interrogate a tapered sensor. The results obtained from processing of the temporal fringes of the sensor were compared with the results as obtained from the spectral fringes using an OSA. The measurement resolutions obtained using the temporal fringes were found to be greater than the ones obtained just as processing the sensor's spectral fringes from an OSA and, the sensor's reusability was successfully tested as discussed in Chapter-4.

Following the interrogation of a single tapered sensor, the system was expanded to interrogate multiple tapered sensors. The efficacy of the sensing system to measure refractive index changes in different media (air and liquid) was investigated with success. The test also demonstrated the ability of the system to obtain measurements under reduced fringe visibility as described in Chapter-5, which otherwise is infeasible using an OSA.

Lastly, the techniques for interrogating multiple FBG arrays and multiple TFOS were combined to interrogate an array of FBG sensors with a tapered sensor in the same sensing network. This demonstrated the system's multi-class sensor interrogation capability. The dedicated photo diodes for the sensing arms ensured simultaneous and independent interrogation of the different sensor classes as discussed in Chapter-6.

The experimental works conducted demonstrate the efficacy and capability of optical interferometric illumination method of interrogating multiple sensors of same class and multiple sensors of multiple classes simultaneously.

1.4 Thesis overview

Chapter-2: Review of optical fibre sensors and sensor interrogation

The thesis investigates the capability of interrogating TFOS, FBG sensors and a combination of both by optical interferometric illumination. Topics dealt in this document include, optical fibres, optical fibre sensors, interferometry, Fourier transform spectroscopy, etc.

Hence, Chapter-2 reviews: the propagation of light through a step-index optical fibre, fundamental principles of interferometry, optical fibre components' working principles and the theoretical basis of the two optical fibre sensors (TFOS and FBG sensor) used in this research.

In addition, the start-of-the-art in the interrogation of the above mentioned two sensors is reviewed in this chapter. The different interrogation schemes have been compared and their merits and demerits analysed.

The interrogation of sensors using Fourier transform spectroscopy and the associated technique of delay calibration using Hilbert transform processing discussed in Chapter-2 forms the foundation of the experiments described in Chapters 3-6.

Chapter-3: Interrogation of fibre Bragg grating arrays by illumination using a low coherence interferogram

Chapter-3 investigates the capability of an interrogation scheme to interrogate multiple arrays of multiple FBGs as well as FBGs with similar wavelengths across multiple arrays by interferometric illumination. In the context of interferometric interrogation using short scans, the efficacy of Hilbert transform processing for delay calibration is also demonstrated. The capability of this interrogation scheme to interrogate other optical fibre sensors and sensor combinations is examined in the subsequent experimental chapters.

Chapter-4: High-resolution tapered sensor interrogation by interferometric illumination

Chapter-4 investigates the capability of interrogating a tapered sensor with high resolution by interferometric illumination using an unbalanced all-fibre Michelson interferometer. The efficacy of the measurement technique is also ascertained by comparing the measurement resolution obtained using the interferometric technique against the technique typically used for computing the change in phase of the tapered sensor's spectrum obtained using an OSA.

Chapter-5: Simultaneous interrogation of multiple tapered fibre optic sensors by interferometric illumination

The capability of an all fibre interferometer to simultaneously interrogate multiple tapered sensors in investigated in Chapter-5. The efficacy of the constructed interferometer to overcome the limitations of conventional interrogation schemes is also examined. The sensors' measurement results were found to be in line with the results highlighted in Chapter-4 when a sensor was individually interrogated, thus demonstrating the interrogation of multiple sensors with equal and high resolution, unlike the OSA.

Chapter-6: Simultaneous interrogation of multiple sensor classes by interferometric illumination

Tapered sensors take up the entire bandwidth of the illuminating source. Thus, combining multiple sensors or sensor types result in an overlap of sensors' spectra. Hence, in the previously reported studies of simultaneous temperature or strain and refractive index measurements using a combination of an interferometric and a grating based sensor [48]–[57], complex matrices were required to separate the sensors' measurement values due to the overlapping spectra and the cross-sensitivities of the sensors.

The capability of simultaneously interrogating an array of multiplexed FBGs and a tapered sensor is investigated in Chapter-6 of this document. To demonstrate the efficacy of the interrogation system, simultaneous sensing of refractive index and temperature is demonstrated, wherein an array of the FBGs and a tapered sensor is interrogated without spectral overlap. The efficacy of the system to interrogate the sensors without cross-sensitivity is also demonstrated.

Chapter-7: Discussion and conclusion

In Chapter-7, the results from the experimental Chapters 3-6 and the objectives achieved are summarised. Along with the summary of results and the list of objectives achieved, the scope for further study/improvement is also presented.

1.5 References

[1] Z. Bai, W. Zhang, S. Gao, H. Zhang, L. Wang, and F. Liu, 'Bend-insensitive long period fiber grating-based high temperature sensor', *Optical Fiber Technology*, vol. 21, pp. 110–114, Jan. 2015, doi: 10.1016/j.yofte.2014.09.004.

[2] J. Canning *et al.*, 'Optical fibre Bragg gratings for high temperature sensing', Edinburgh, United Kingdom, Oct. 2009, p. 75032N, doi: 10.1117/12.834470.

[3] S. J. Mihailov, 'Fiber Bragg Grating Sensors for Harsh Environments', *Sensors*, vol. 12, no. 2, pp. 1898–1918, Feb. 2012, doi: 10.3390/s120201898.

[4] R. Sundaram, G. M. Kamath, N. Gupta, and M. S. Rao, 'Structural health monitoring of co-cured composite structures using FBG sensors', San Diego, CA, May 2005, p. 559, doi: 10.1117/12.597261.

[5] H. Song, W. Wang, Y. Zhou, and G. Zhou, 'Mechanical properties of composites with embedded FBG sensors in different layer', in *2011 IEEE 5th International Conference on Cybernetics and Intelligent Systems (CIS)*, Qingdao, China, Sep. 2011, pp. 52–56, doi: 10.1109/ICCIS.2011.6070301.

[6] W. Wang, H. Song, J. Xue, W. Guo, and M. Zheng, 'Overview of intelligent composites with embedded FBG sensors', in *2011 IEEE 5th International Conference on Cybernetics and Intelligent Systems (CIS)*, Qingdao, China, Sep. 2011, pp. 47–51, doi: 10.1109/ICCIS.2011.6070300.

[7] K. Bremer *et al.*, 'Fibre optic pressure and temperature sensor for geothermal wells', in *2010 IEEE Sensors*, Kona, HI, Nov. 2010, pp. 538–541, doi: 10.1109/ICSENS.2010.5690125.

[8] S. Poeggel, G. Leen, K. Bremer, and E. Lewis, ‘Miniature Optical fiber combined pressure- and temperature sensor for medical applications’, in *2012 IEEE Sensors*, Taipei, Taiwan, Oct. 2012, pp. 1–4, doi: 10.1109/ICSENS.2012.6411305.

[9] Xiaohui Liu *et al.*, ‘Fiber optic pressure and temperature monitoring system for downhole application’, in *2016 15th International Conference on Optical Communications and Networks (ICOCN)*, Hangzhou, China, Sep. 2016, pp. 1–3, doi: 10.1109/ICOCN.2016.7875606.

[10] B. N. Shivananju *et al.*, ‘CO2 sensing at room temperature using carbon nanotubes coated core fiber Bragg grating’, *Review of Scientific Instruments*, vol. 84, no. 6, p. 065002, Jun. 2013, doi: 10.1063/1.4810016.

[11] S. Saad and L. Hassine, ‘Hydrogen detection with FBG sensor technology for disaster prevention’, *Photonic Sensors*, vol. 3, no. 3, pp. 214–223, Sep. 2013, doi: 10.1007/s13320-013-0109-4.

[12] H. Zhou *et al.*, ‘Study on Fiber-optic Hydrogen Sulfide Gas Sensor’, *Physics Procedia*, vol. 56, pp. 1102–1106, 2014, doi: 10.1016/j.phpro.2014.08.023.

[13] P. Lu, L. Men, K. Sooley, and Q. Chen, ‘Tapered fiber Mach–Zehnder interferometer for simultaneous measurement of refractive index and temperature’, *Applied Physics Letters*, vol. 94, no. 13, p. 131110, Mar. 2009, doi: 10.1063/1.3115029.

[14] P. Wang, H. Zhao, X. Wang, G. Farrell, and G. Brambilla, ‘A Review of Multimode Interference in Tapered Optical Fibers and Related Applications’, *Sensors*, vol. 18, no. 3, p. 858, Mar. 2018, doi: 10.3390/s18030858.

[15] K. Q. Kieu and M. Mansuripur, 'Biconical Fiber Taper Sensors', *IEEE Photonics Technology Letters*, vol. 18, no. 21, pp. 2239–2241, Nov. 2006, doi: 10.1109/LPT.2006.884742.

[16] Y. Tian, W. Wang, N. Wu, X. Zou, and X. Wang, 'Tapered Optical Fiber Sensor for Label-Free Detection of Biomolecules', *Sensors*, vol. 11, no. 12, pp. 3780–3790, Mar. 2011, doi: 10.3390/s110403780.

[17] S. W. Harun, K. S. Lim, C. K. Tio, K. Dimyati, and H. Ahmad, 'Theoretical analysis and fabrication of tapered fiber', *Optik - International Journal for Light and Electron Optics*, vol. 124, no. 6, pp. 538–543, Mar. 2013, doi: 10.1016/j.ijleo.2011.12.054.

[18] M. A. Davis, D. G. Bellemore, M. A. Putnam, and A. D. Kersey, 'Interrogation of 60 fibre Bragg grating sensors with microstrain resolution capability', *Electronics Letters*, vol. 32, no. 15, p. 1393, 1996, doi: 10.1049/el:19960908.

[19] A. D. Kersey, T. A. Berkoff, and W. W. Morey, 'Multiplexed fiber Bragg grating strain-sensor system with a fiber Fabry–Perot wavelength filter', *Optics Letters*, vol. 18, no. 16, p. 1370, Aug. 1993, doi: 10.1364/OL.18.001370.

[20] M. S. Muller *et al.*, 'Fiber-Optic Sensor Interrogation Based on a Widely Tunable Monolithic Laser Diode', *IEEE Transactions on Instrumentation and Measurement*, vol. 59, no. 3, pp. 696–703, Mar. 2010, doi: 10.1109/TIM.2009.2025987.

[21] M. Perry, P. Orr, P. Niewczas, and M. Johnston, 'High-Speed Interferometric FBG Interrogator With Dynamic and Absolute Wavelength Measurement

Capability’, *Journal of Lightwave Technology*, vol. 31, no. 17, pp. 2897–2903, Sep. 2013, doi: 10.1109/JLT.2013.2276391.

[22] Y. Marin, T. Nannipieri, C. Oton, and F. Di Pasquale, ‘Integrated FBG Sensors Interrogation using Active Phase Demodulation on a Silicon Photonic Platform’, *Journal of Lightwave Technology*, pp. 1–1, 2016, doi: 10.1109/JLT.2016.2598395.

[23] D. Pustakhod, E. Kleijn, K. Williams, and X. Leijtens, ‘High-Resolution AWG-Based Fiber Bragg Grating Interrogator’, *IEEE Photonics Technology Letters*, vol. 28, no. 20, pp. 2203–2206, Oct. 2016, doi: 10.1109/LPT.2016.2587812.

[24] M. A. Davis and A. D. Kersey, ‘Application of a fiber Fourier transform spectrometer to the detection of wavelength-encoded signals from Bragg grating sensors’, *Journal of Lightwave Technology*, vol. 13, no. 7, pp. 1289–1295, Jul. 1995, doi: 10.1109/50.400685.

[25] D. A. Flavin, R. McBride, and J. D. C. Jones, ‘Short-scan interferometric interrogation and multiplexing of fibre Bragg grating sensors’, *Optics Communications*, vol. 170, no. 4–6, pp. 347–353, Nov. 1999, doi: 10.1016/S0030-4018(99)00515-5.

[26] Y. Wang, J. Gong, B. Dong, D. Y. Wang, T. J. Shillig, and A. Wang, ‘A Large Serial Time-Division Multiplexed Fiber Bragg Grating Sensor Network’, *Journal of Lightwave Technology*, vol. 30, no. 17, pp. 2751–2756, Sep. 2012, doi: 10.1109/JLT.2012.2205897.

[27] T. A. Berkoff, M. A. Davis, D. G. Bellemore, A. D. Kersey, G. M. Williams, and M. A. Putnam, ‘Hybrid time- and wavelength-division multiplexed fiber

Bragg grating sensor array’, 1995, vol. 2444, pp. 288–294, doi: 10.1117/12.207684.

[28] Y. Ou *et al.*, ‘Large WDM FBG Sensor Network Based on Frequency-Shifted Interferometry’, *IEEE Photonics Technology Letters*, vol. 29, no. 6, pp. 535–538, Mar. 2017, doi: 10.1109/LPT.2017.2663665.

[29] Q. Liu *et al.*, ‘Ultrahigh Resolution Multiplexed Fiber Bragg Grating Sensor for Crustal Strain Monitoring’, *IEEE Photonics J.*, vol. 4, no. 3, pp. 996–1003, Jun. 2012, doi: 10.1109/JPHOT.2012.2201217.

[30] ‘Tunable Laser Source - Apex Technologies’. Apex Technologies, Accessed: Sep. 04, 2020. [Online]. Available: https://www.apex-t.com/optical-tunable-laser-source/.

[31] ‘Tunable Lasers Overview’. Thorlabs, Accessed: Sep. 04, 2020. [Online]. Available: https://www.thorlabs.com/catalogPages/540.pdf.

[32] ‘Microsoft Word - Spec_Sheet_Tunics_Plus_V5.Doc’. Anritsu, Accessed: Sep. 04, 2020. [Online]. Available: https://dl.cdn-anritsu.com/en-us/test-measurement/files/Brochures-Datasheets-Catalogs/datasheet/Tunics_Plus_v5.pdf.

[33] J. Mo, L. He, and C. Lu, ‘A fast tunable semiconductor laser for FBG sensor interrogation systems’, in *IEEE SENSORS 2014 Proceedings*, Valencia, Spain, Nov. 2014, pp. 1348–1351, doi: 10.1109/ICSENS.2014.6985261.

[34] J. Miller *et al.*, ‘Biconically Tapered Fiber Optic Probes for Rapid Label-Free Immunoassays’, *Biosensors*, vol. 5, no. 2, pp. 158–171, Apr. 2015, doi: 10.3390/bios5020158.

[35] W. B. Ji, Y. C. Tan, B. Lin, S. C. Tjin, and K. K. Chow, ‘Nonadiabatically Tapered Microfiber Sensor With Ultrashort Waist’, *IEEE Photon. Technol. Lett.*, vol. 26, no. 22, pp. 2303–2306, Nov. 2014, doi: 10.1109/LPT.2014.2353931.

[36] S. H. Girei, A. A. Shabaneh, P. T. Arasu, S. Painam, and M. H. Yaacob, ‘Tapered multimode fiber sensor for ethanol sensing application’, in *2013 IEEE 4th International Conference on Photonics (ICP)*, Melaka, Malaysia, Oct. 2013, pp. 275–277, doi: 10.1109/ICP.2013.6687137.

[37] D. Tiwari, K. Mullaney, S. Korposh, S. W. James, S.-W. Lee, and R. P. Tatam, ‘An ammonia sensor based on Lossy Mode Resonances on a tapered optical fibre coated with porphyrin-incorporated titanium dioxide’, *Sensors and Actuators B: Chemical*, vol. 242, pp. 645–652, Apr. 2017, doi: 10.1016/j.snb.2016.11.092.

[38] M. Barbu, K. Jovanovich, R. Trahan, and P. Chirlian, ‘The use of tapered fibers in an intensity based single mode temperature sensor’, in *2nd ISA/IEEE Sensors for Industry Conference*, Houston, TX, USA, 2002, pp. 47–50, doi: 10.1109/SFICON.2002.1159806.

[39] B. Li, L. Jiang, S. Wang, L. Zhou, H. Xiao, and H.-L. Tsai, ‘Ultra-Abrupt Tapered Fiber Mach-Zehnder Interferometer Sensors’, *Sensors*, vol. 11, no. 6, pp. 5729–5739, May 2011, doi: 10.3390/s110605729.

[40] Di Wu, Yong Zhao, and Qi Wang, ‘SMF Taper Evanescent Field-Based RI Sensor Combined With Fiber Loop Ring Down Technology’, *IEEE Photon. Technol. Lett.*, vol. 27, no. 17, pp. 1802–1805, Sep. 2015, doi: 10.1109/LPT.2015.2443128.

[41] P. Fellgett, ‘Spectromètre interférentiel multiplex pour mesures infra-rouges sur les étoiles’, *Journal de Physique et le Radium*, vol. 19, no. 3, pp. 237–240, 1958, doi: 10.1051/jphysrad:01958001903023700.

[42] P. Jacquinot, ‘New developments in interference spectroscopy’, *Reports on Progress in Physics*, vol. 23, no. 1, p. 267, 1960.

[43] J. Connes and P. Connes, ‘Near-Infrared Planetary Spectra by Fourier Spectroscopy. I. Instruments and Results’, *J. Opt. Soc. Am.*, vol. 56, no. 7, pp. 896–910, Jul. 1966, doi: 10.1364/JOSA.56.000896.

[44] K. T. O’Mahoney, R. P. O’Byrne, S. V. Sergeyev, Lin Zhang, and I. Bennion, ‘Short-Scan Fiber Interferometer for High-Resolution Bragg Grating Array Interrogation’, *IEEE Sensors Journal*, vol. 9, no. 10, pp. 1277–1281, Oct. 2009, doi: 10.1109/JSEN.2009.2029818.

[45] L. M. N. Amaral, O. Frazao, J. L. Santos, and A. B. Lobo Ribeiro, ‘Fiber-Optic Inclinometer Based on Taper Michelson Interferometer’, *IEEE Sensors Journal*, vol. 11, no. 9, pp. 1811–1814, Sep. 2011, doi: 10.1109/JSEN.2011.2105264.

[46] P. A. S. Jorge, ‘Fiber modal Michelson interferometers with coherence addressing and heterodyne interrogation’, *Opt. Eng*, vol. 47, no. 4, p. 044401, Apr. 2008, doi: 10.1117/1.2903089.

[47] S. G. Lipson, H. Lipson, and D. S. Tannhauser, *Optical physics*, 3rd ed. Cambridge ; New York, NY, USA: Cambridge University Press, 1995.

[48] Q. Yao *et al.*, ‘A sandwich fiber sensor for simultaneous measurement of RI and temperature’, in *2017 16th International Conference on Optical*

Communications and Networks (ICOCN), Wuzhen, Aug. 2017, pp. 1–4, doi: 10.1109/ICOCN.2017.8121353.

[49] Y. Cao, C. Zhao, and Z. Tong, ‘All fiber sensor based on Mach-Zehnder interferometer for simultaneous measurement of temperature and refractive index’, *Optoelectronics Letters*, vol. 11, no. 6, pp. 438–443, Nov. 2015, doi: 10.1007/s11801-015-5175-y.

[50] F. Ahmed, V. Ahsani, A. Saad, and M. B. G. Jun, ‘Bragg Grating Embedded in Mach-Zehnder Interferometer for Refractive Index and Temperature Sensing’, *IEEE Photonics Technology Letters*, vol. 28, no. 18, pp. 1968–1971, Sep. 2016, doi: 10.1109/LPT.2016.2580582.

[51] X. Zhang, W. Peng, Y. Liu, and Q. Yu, ‘Core-offset-based fiber Bragg grating sensor for refractive index and temperature measurement’, *Optical Engineering*, vol. 52, no. 2, p. 024402, Feb. 2013, doi: 10.1117/1.OE.52.2.024402.

[52] C. R. Liao, Y. Wang, D. N. Wang, and M. W. Yang, ‘Fiber In-Line Mach–Zehnder Interferometer Embedded in FBG for Simultaneous Refractive Index and Temperature Measurement’, *IEEE Photonics Technology Letters*, vol. 22, no. 22, pp. 1686–1688, Nov. 2010, doi: 10.1109/LPT.2010.2079924.

[53] X. Yu, X. Chen, D. Bu, J. Zhang, and S. Liu, ‘In-Fiber Modal Interferometer for Simultaneous Measurement of Refractive Index and Temperature’, *IEEE Photonics Technology Letters*, vol. 28, no. 2, pp. 189–192, Jan. 2016, doi: 10.1109/LPT.2015.2489559.

[54] Yanfang Lu, Changyu Shen, Chuan Zhong, Debao Chen, Xinyong Dong, and Jinhui Cai, ‘Refractive Index and Temperature Sensor Based on Double-Pass

M–Z Interferometer With an FBG', *IEEE Photonics Technology Letters*, vol. 26, no. 11, pp. 1124–1127, Jun. 2014, doi: 10.1109/LPT.2014.2315804.

[55] Q. Yao *et al.*, 'Simultaneous measurement of refractive index and temperature based on a core-offset Mach–Zehnder interferometer combined with a fiber Bragg grating', *Sensors and Actuators A: Physical*, vol. 209, pp. 73–77, Mar. 2014, doi: 10.1016/j.sna.2014.01.017.

[56] Y. Bai, B. Yin, C. Liu, S. Liu, Y. Lian, and S. Jian, 'Simultaneous Measurement of Refractive Index and Temperature Based on NFN Structure', *IEEE Photonics Technology Letters*, vol. 26, no. 21, pp. 2193–2196, Nov. 2014, doi: 10.1109/LPT.2014.2350023.

[57] M. Zhou, X. Dong, and X. Liu, 'Simultaneous measurement of temperature and refractive index with thin-core fiber MZI containing fiber Bragg grating', in *2017 16th International Conference on Optical Communications and Networks (ICOCN)*, Wuzhen, Aug. 2017, pp. 1–3, doi: 10.1109/ICOCN.2017.8121291.

Chapter 2

Review of Optical Fibre Sensors and Sensor Interrogation Methods

2.1 Introduction

The fibre optic sensors or optical fibre sensors are waveguides in which the light guided within is modulated in response to an external stimulus. A fibre optic sensor based sensing system typically comprises an optical source, an optical fibre sensor and an unit to demodulate or interrogate the sensor. A number of different fibre based sensing systems have been developed to-date for a variety of sensing applications.

This thesis investigates the capability of interrogating different optical fibre sensors such as the tapered optical fibre sensor and the fibre Bragg grating sensor by interferometric illumination. The areas covered in this thesis are spectroscopy, interferometry, Fourier transform processing, Hilbert transform processing and optical fibre sensing. This chapter will therefore review: fundamental principles of interferometry, propagation of light through an optical fibre, theory and principle working of the fibre Bragg grating and tapered fibre optic sensors, methods of processing interferometric signals and the state-of-the-art in the interrogation of fibre Bragg grating and tapered sensors.

2.2 Chapter overview

Based on the areas covered in this thesis mentioned above, the three main aspects of this review chapter are interferometric principles and interferometry

(Sections 2.3-2.5), principles of single mode optical fibre and fibre optic sensors (Sections 2.6-2.9) and lastly, the interrogation methods of fibre Bragg grating and tapered sensors (Sections 2.10-2.11).

The work reported in the later chapters investigates optical fibre sensor interrogation methods, and therefore the theory and characteristics of light propagation is discussed in Section 2.3. A phenomenon in which two or more light waves overlap to form a resultant wave is called interference. The principle of superposition which governs this interference phenomenon is first elaborated in Section 2.4 and subsequently, the phenomenon of interference is discussed in Section 2.5.

Optical fibres, sensors and components are used and discussed extensively throughout this thesis and therefore, the structure of a typical single mode optical fibre used in this research is outlined in Section 2.6. Following on the introduction to optical fibre in Section 2.6, the theory behind the propagation of light within an optical fibre and the potential causes for propagation losses are presented in Section 2.7. The theories of fibre optic components such as couplers, isolators, fibre stretcher, etc. used in the experiments are explained in Section 2.8.

The fibre optic sensors or optical fibre sensors are devices in which the light propagating through it is modified in response to external forces such as pressure, temperature, refractive index change, strain that act on the fibre. The classification of fibre optic sensors is presented in Section 2.9. The capability and the efficacy of the interferometric illumination interrogation system is assessed using only two types of sensors, namely the fibre Bragg grating (FBG) and the tapered sensor.

An FBG sensor is an optical fibre with a periodic change in the refractive index of its core. When illuminated with a broadband light source, the FBG sensor reflects a narrow band of light characteristic to it and this reflected wavelength of light is called the Bragg wavelength of the sensor, denoted by λ_B [1]. The theoretical principles of an FBG sensor, its operation, manufacturing methods, and types are described in Section 2.9.2.

The tapered optical fibre sensors operate on the principle of modal interference. In a tapered sensor, a section of the fibre's diameter is reduced normally by heating and simultaneously stretching, or by polishing. As the light propagates through the tapered section of the fibre, in accordance with Maxwell's boundary conditions [2], a field called evanescent field extends into the cladding of the fibre. The changes to the medium surrounding the tapered sensor result in changes to the evanescent field characteristics. Thus, by monitoring the evanescent field, the external medium can be assessed. The operational principle of the tapered sensor or the evanescent wave theory and the tapered sensor fabrication methods typically used are discussed in Section 2.9.3.

As previously stated, the aim of this thesis is to investigate the capability and efficacy of interrogating varied fibre optic sensor classes by interferometric illumination using an all-fibre Michelson interferometer. Interferometry, the tool which forms the basis of this research is introduced in Section 2.10.1. The interferometers and interferometer types are discussed in Section 2.10.2. The techniques used for processing the interferometric signals from the interferometers are discussed in Sections 2.10.5 and 2.10.6. The state-of-the-art in the interrogation of FBGs and tapered sensors have been reviewed in Section 2.11 and summarised in Section 2.12.

2.3 Light

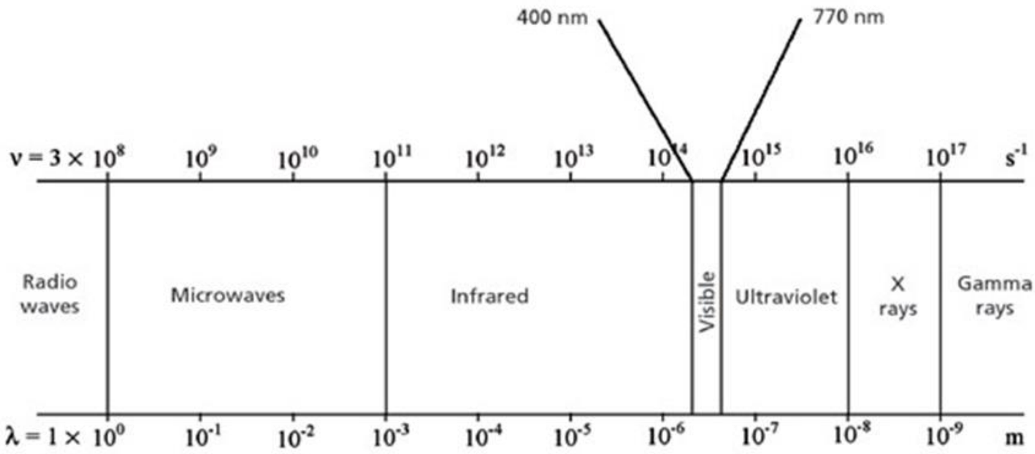

Figure 2-1: Electromagnetic spectrum

When classified in terms of frequency, the "light" part of the EM spectrum is in fact only the narrowband visible subset of a spectrum which covers all frequencies. Figure 2-1 shows the graphical representation of the electromagnetic spectrum. The work reported in this thesis uses the near infrared section of the spectrum centred around the 1550nm wavelength band. This band is widely used by the telecommunication industry and hence due to mass production, optical components operating in this band are cheaper when compared to the mid infrared and far infrared band components.

The light has been pictured as waves, as well as discrete particles carrying discrete amounts of energy called photons and hence, the light is said to have a dual nature.

2.3.1 The particle model

In the particle model, the light is considered to be a particle of energy called the photon. The amount of energy carried by the photon is given by the following equation called the Planck's equation.

$$E = hv \tag{2-1}$$

In the Equation (2-1), E is the quantum of electromagnetic energy and v is the frequency of radiation. The energy and frequency are linked by a constant of proportionality h called the Planck's constant which has a value of 6.63x10^{-34} J-s.

2.3.2 The wave model

A key characteristic of a light wave is its interdependency between the magnetic fields **B** and electric fields **E.** Changes to magnetic fields affects the electric fields and vice versa. The wave nature of light can be expressed by Maxwell's equations given below which also give the relationship between the electric and magnetic fields [2]. This treatment follows closely to that of Hecht [2] and is presented here for completeness.

$$\oint_C \boldsymbol{E}.dl = -\iint_A \frac{\partial \boldsymbol{B}}{\partial t}\, .d\boldsymbol{S} \tag{2-2}$$

$$\oint_C \boldsymbol{B}.dl = \mu_0 \varepsilon_0 \iint_A \frac{\partial \boldsymbol{E}}{\partial t}\, .d\boldsymbol{S} \tag{2-3}$$

$$\oiint_A \boldsymbol{B}.d\boldsymbol{S} = 0 \tag{2-4}$$

$$\oiint_A \boldsymbol{E}.d\boldsymbol{S} = 0 \tag{2-5}$$

Maxwell's treatment in Equations (2-2)-(2-5) is applicable for all electric and magnetic fields in free space, where $\mu = \mu_0$ and $\varepsilon = \varepsilon_0$. Components of the electromagnetic field obey the standard differential wave Equation (2-6) given below where $\nu = \frac{1}{\sqrt{\mu_0 . \varepsilon_0}}$.

$$\nabla^2\psi = \frac{1}{v^2}\frac{\partial^2\psi}{\partial t^2}$$
(2-6)

Equation (2-6) with Laplacian operator ∇^2 is expressed in cartesian coordinates by,

$$\frac{\partial^2\psi}{\partial x^2} + \frac{\partial^2\psi}{\partial y^2} + \frac{\partial^2\psi}{\partial z^2} = \frac{1}{v^2}\frac{\partial^2\psi}{\partial t^2}$$
(2-7)

The sum of the solutions of the differential wave Equation (2-7) is also a solution of the wave equation. Thus, differential wave Equation (2-7) demonstrates the ability of the waves to superimpose on one another as governed by the principle of superposition described in the following section.

2.4 The principle of superposition

When two or more waves of either similar or distinctive characteristics travel through the same medium simultaneously, they superpose one another. The resultant of two or more superposed waves is characterised by the principle of superposition. According to the principle of superposition, the net displacement of the medium is equal to the sum of individual wave displacements.

Assuming $\psi_1$and ψ_2 are independent displacements of two waves, the resultant displacement ψ is the sum of the separate displacements of the constituent waves as given by,

$$\psi = \psi_1 + \psi_2$$
(2-8)

As per the principle of superposition, if $\psi_1$and ψ_2 are independent solutions of the wave Equation (2-7), then their linear combination ψ as given in Equation (2-8) is also a solution of the wave equation.

In the following sections, superposition of waves with the same frequency will be discussed along with superposition of waves with varying frequency [3].

2.4.1 Superposition of waves with the same frequency

A wave with $\boldsymbol{k}$ as the direction of the propagation vector, $\boldsymbol{r}$ as an arbitrary point in space and φ_0 as the initial phase angle is expressed by the following equation,

$$E = E_0 \sin(\boldsymbol{k}.\boldsymbol{r} + \omega t + \varphi_0) \tag{2-9}$$

The behaviour of the wave is studied at a fixed point in space and hence, $\boldsymbol{k}.\boldsymbol{r}$ is treated as a constant. Thus, the above equation becomes,

$$E = E_0 \sin(\omega t + \alpha) \tag{2-10}$$

where the phase angle constant α is given by,

$$\alpha = \boldsymbol{k}.\boldsymbol{r} + \varphi_0 \tag{2-11}$$

When two such waves intersect at a point, the difference in phase angle is given by,

$$\alpha_2 - \alpha_1 = \boldsymbol{k}.(\boldsymbol{r_2} - \boldsymbol{r_1}) + (\varphi_{02} - \varphi_{01}) \tag{2-12}$$

where the path difference is given by $\boldsymbol{k}.(\boldsymbol{r_2} - \boldsymbol{r_1})$ and the phase difference is given by $(\varphi_{02} - \varphi_{01})$. The time variations of the EM waves at a given point is given by,

$$E_1 = E_{01} \sin(\omega t + \alpha_1) \tag{2-13}$$

$$E_2 = E_{02} \sin(\omega t + \alpha_2) \tag{2-14}$$

By superposition principle, the resultant electric field E_R at the point is

$$E_R = E_1 + E_2 = E_{01} \sin(\omega t + \alpha_1) + E_{02} \sin(\omega t + \alpha_2) \tag{2-15}$$

Equation (2-15) can be rewritten as,

$$E_R = (E_{01} \cos \alpha_1 + E_{02} \cos \alpha_2) \sin \omega t + (E_{01} \sin \alpha_1 + E_{02} \sin \alpha_2) \cos \omega t \tag{2-16}$$

Thus, the resultant wave E_R is of the same frequency ω as the two superposing waves E_1 and E_2.

2.4.2 Superposition of waves with varying frequency

The superposition of waves with varying frequency implies, varying wavelength as well as velocity. Superposition of such waves result in periodically large and small resultant amplitudes. Points where individual crests coincide, yields maximum amplitude and points where the crests are out of phase, yields minimum amplitude. Let two waves closely differing in frequency and wavenumber be,

$$E_1 = E_0 \cos(k_1 x - \omega_1 t) \tag{2-17}$$

$$E_2 = E_0 \cos(k_2 x - \omega_2 t) \tag{2-18}$$

Assuming the medium to be the same, by using the superposition principle, the resultant wave is given by,

$$E_R = E_1 + E_2 = E_0[\cos(k_1 x - \omega_1 t) + \cos(k_2 x - \omega_2 t)] \tag{2-19}$$

Simplifying, we get,

$$E_R = 2E_0 \cos\left[\frac{(k_1 + k_2)}{2}x - \frac{(\omega_1 + \omega_2)}{2}t\right] \cos\left[\frac{(k_1 - k_2)}{2}x - \frac{(\omega_1 - \omega_2)}{2}t\right] \tag{2-20}$$

Thus, the wave is represented as a product of two cosine waves. First cosine wave has a frequency and propagation constant that are the averages of frequencies and propagation constants of component waves, respectively. Second cosine wave has a frequency and propagation constant that are smaller than the component waves. The velocity can be calculated from frequency ω and propagation constant k using,

$$\upsilon = \frac{\omega}{k} \tag{2-21}$$

In the Equation (2-20), it's first part corresponds to a wave with almost the same properties as that of the superposing individual waves and the second part corresponds to a wave with a much lower frequency and which acts as the envelope of the sum of the waves. The velocity of the high-frequency wave is called the phase velocity, denoted by υ_p and velocity of the low-frequency wave is called the group velocity or the velocity of the envelope, denoted by υ_g and are given by,

$$\upsilon_p = \frac{\omega_1 + \omega_2}{k_1 + k_2} \cong \frac{\omega}{k} \tag{2-22}$$

$$\upsilon_g = \frac{\omega_1 - \omega_2}{k_1 - k_2} \cong \frac{d\omega}{dk} \tag{2-23}$$

In vacuum, the phase velocity is equal to the group velocity. However, when light propagates through a medium, the phase and group velocities vary. The phenomenon due to which the phase and group velocities vary within the medium is called dispersion. Dispersion is a major limiting factor to the performance of optical fibre systems and is critical to the choice of operational wavelength and fibre.

In the cases discussed above, the waves were assumed to travel in the same medium in the same direction. But when two waves travelling in the opposite direction in a medium superpose, it results in the formation of standing waves. When the travelling waves are in phase, the resultant is the sum of the amplitude of two waves. But when they are 180^0 out of phase, they cancel each other, and the resultant is zero. Thus, they alternate between maximum and zero. This phenomenon is called interference which forms the basis of the experimental work reported in this document. The phenomenon of interference is described in the following section.

2.5 Interference

As per the principle of superposition described in the previous section, if the superposition of waves result in an enhancement or an increase in the amplitude, it is called a constructive interference and if it results in a diminution or a decrease in the amplitude, it is called a destructive interference. The pattern formed by the interference of waves is called an interferogram. Figure 2-2 shows a pictorial representation of constructive and destructive interference. Using the superposition principle, the equation for a two-beam interference is given by [4],

$$I = I_1 + I_2 + 2\sqrt{I_1 I_2 \cos \varphi} \tag{2-24}$$

where I is the irradiance of interference, $I_1$is the irradiance of beam 1 I_2 is the irradiance of beam 2 and φ is the phase difference between the beams. For stable light wave interference, the interfering waves must be coherent. The property of coherence is dealt with in detail in the upcoming section.

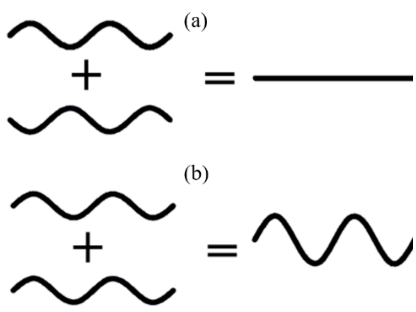

Figure 2-2: (a) Destructive Interference, (b) Constructive Interference

2.5.1 Coherence

The coherence of an optical source is the ability of the source to produce interference fringes when its light is split and recombined. In a strict sense, an optical source is not really monochromatic as it contains components of various wavelengths/frequencies within a range called the linewidth. The optical sources such as He-Ne lasers have a very narrow linewidth and are quasi-monochromatic (close to ideal monochromatic behaviour). On the other hand, the optical sources like the one used in the experiments described in Chapters 3-6, have a very broad linewidth (>100nm) and hence such sources are called broadband sources. The spectral intensity or the intensity spectrum of a source is the squared magnitude of the complex Fourier transform of its real electric field.

When the light from a source is split, a relative delay introduced and the beams recombined, the resulting intensity pattern contains an interference term which is the real part of the degree of temporal coherence. The degree of temporal coherence $\gamma(\tau)$ is given by [5],

$$\gamma(\tau) = \frac{\langle f(t) f^*(t+\tau) \rangle}{\langle f(t) f^*(t) \rangle} = \frac{\langle f(t) f^*(t+\tau) \rangle}{I} \tag{2-25}$$

In the above Equation (2-25), the numerator term $\langle f(t) f^*(t+\tau) \rangle$ is called the temporal coherence correlation function or coherence correlation function or mutual coherence function. If the real part of $\gamma(\tau)$ exhibits oscillations (interference fringes) with constant visibility for large values of τ, then the source is said to have a high coherence. On the other hand, if the visibility of the oscillations decay quickly as τ increases, then the coherence is said to be low. The visibility of the interference fringes V is obtained from the degree of coherence expression as $V = |\gamma(\tau)|$. Thus, for any light wave, a characteristic delay time for the reduction of interference fringes' visibility known as the coherence time can be determined. Based on $V = |\gamma(\tau)|$, coherence time τ_c is a value at which $|\gamma(\tau_c)| = \frac{1}{e}$.

The *Wiener–Khinchin theorem* relates the power spectrum (spectral intensity) of $f(t)$ and the coherence correlation function as follows [5],

$$|F(\omega)|^{2} = I \int_{-\infty}^{\infty} \gamma(\tau) e^{-i\omega\tau} d\tau$$

(2-26)

where, I is the intensity which is equal to $\langle f(t)f^{*}(t)\rangle$ (from Equation (2-25)), $|F(\omega)|^{2}$ is the power spectrum (spectral intensity) of $f(t)$. Thus, as per the *Wiener–Khinchin theorem,* the Fourier transform of a time domain signal's autocorrelation function yields the signal's power spectral density. As the coherence correlation function and intensity spectrum form a Fourier transform pair, there is an inverse relationship between the linewidth of the source and its coherence time. The broader the spectrum the shorter is the coherence time and vice versa.

The coherence of a wave can also be characterised by its length which is given in terms of the coherence time as,

$$L_{coh} = c\tau_{c} = \frac{\lambda_{c}^{2}}{\lambda_{FWHM}}$$

(2-27)

In addition to the coherence time τ_{c} and the speed of light constant c, in Equation (2-27), λ_{c} is the source wavelength, λ_{FWHM} is the full width at half-maximum (FWHM) (approximately one half of the linewidth) of an optical source with a typical gaussian profile.

In optics, a Michelson interferometer is an interferometric autocorrelator of the input beam. Thus, the output of the interferometer is the coherence correlation function $\langle f(t)f^{*}(t+\tau)\rangle$ of the interferometer's input optical beam and is called an interferogram. Fourier transform spectroscopy (FTS) is an implementation of Michelson interferometer that is widely used for spectral analysis. In FTS, the source's optical spectrum is obtained from the Fourier transform of the temporal coherence function [5]. FTS which forms the basis of the interrogation methods described in later sections/chapters thus exploits the *Wiener–Khinchin theorem* for interrogating the sensors.

2.6 Optical fibre

A structure that is used to guide electromagnetic waves is called a waveguide. The waveguides can be either metallic or dielectric. The metallic waveguides are prone to losses in the optical frequencies and hence, dielectric waveguides called optical fibres are used for transmitting light.

Most optical fibres are made of silica or plastic, but for special applications, fibres with special compositions (dopant and material) are used. An optical fibre generally consists of a core with a refractive index higher than that of the surrounding cladding. And a layer of protective coating called the buffer, surrounds the cladding. But depending upon the usage, the fibre could contain several more layers of protection [6]. Figure 2-3 shows the structure of a typical single mode optical fibre.

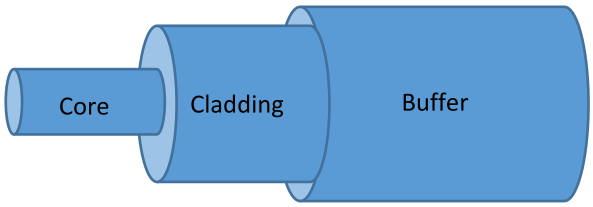

Figure 2-3: Structure of a typical optical fibre

Based on the core-cladding refractive index profile, a fibre may be classified as either a graded-index fibre or a step-index fibre. In addition to the core-cladding refractive index profile, another parameter called numerical aperture *(NA)* can also be used to define the fibre characteristic. The numerical aperture is given by the Equation (2-28) where, n_0 is the refractive index of the medium surrounding the fibre, α is the angle of acceptance of the fibre core, n_{core} and $n_{cladding}$ are the refractive indices of the core and cladding respectively.

$$NA = \sin\alpha = \frac{1}{n_0}\sqrt{{n_{core}}^2 - {n_{cladding}}^2} \tag{2-28}$$

The number of modes permitted for transmission within an optical fibre can be calculated using its numerical aperture value and the wavelength of light used to illuminate the fibre. The equation for computing the maximum number of permitted modes m_{max} is given by,

$$m_{max} = \frac{1}{2}\left(\frac{\pi d}{\lambda} NA\right)^2 \tag{2-29}$$

where λ is the wavelength of light illuminating the fibre, d is the diameter of the fibre core and NA is the fibre's numerical aperture. In addition to classification of an optical fibre based on core-cladding refractive index profile, based on the number of modes supported by an optical fibre, it may be classified as either single mode or multimode.

The optical fibres used in the experiments described in the experimental chapters of this document are of single mode type only with a NA of ~0.14. Hence, references to the term "optical fibre" in this document denote the single mode fibre only. Propagation characteristics of light through a typical single mode fibre is described in the following section.

2.7 Propagation of light through an optical fibre

2.7.1 Total internal reflection

The light entering the optical fibre is contained within it due to a phenomenon called total internal reflection. For total internal reflection to occur, the refractive index of the fibre core must be higher than the refractive index of the fibre cladding and the angle of incidence of light into the fibre should be greater than the critical angle θ_c, which is given by the following expression, where n_2 and n_1 are the refractive indices of cladding and core respectively.

$$\theta_c = \sin^{-1}\left(\frac{n_2}{n_1}\right) \tag{2-30}$$

For a better understanding of the concept of total internal reflection, the electromagnetic wave theory at the core-cladding interface is analysed by assuming the fibre core to be a planar structure with light wave incident on the boundary between two dielectric media with refractive index n_1 and n_2 as shown in Figure 2-4 [7].

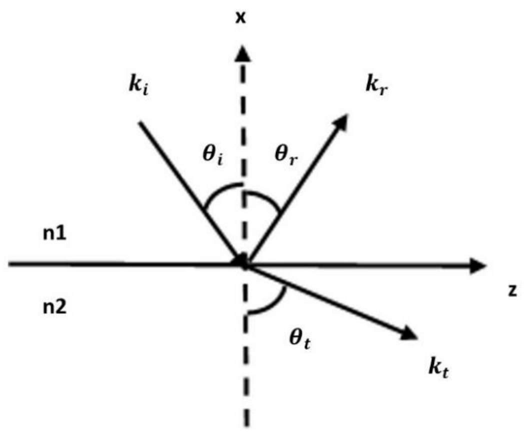

Figure 2-4: Lightwave incident on a planar boundary

A wave incident on the boundary is partially reflected and the rest is transmitted. Equations for the incident, reflected and transmitted waves are given by,

$$E_i = A_i . e^{i(\omega t - k_i . r)} \tag{2-31}$$

$$E_r = A_r . e^{i(\omega t - k_r . r)} \tag{2-32}$$

$$E_t = A_t . e^{i(\omega t - k_t . r)} \tag{2-33}$$

where A stands for the amplitude component, k the propagation vector, ω the angular frequency, r a point on the coordinates and t is the time. Subscripts i, t, and r denote incidence, transmission, and reflection. As per Maxwell's boundary conditions [2], the phase variation along the interface must be the same for the incident, transmitted and reflected electric fields. From Figure 2-4, the phase variation along the interface can be seen to depend only on the z-axis.

Considering only the z components of the propagation vectors and equating the phases of the incident, reflected and transmitted waves, we get,

$$k_i . \sin\theta_i = k_r . \sin\theta_r = k_t . \sin\theta_t \tag{2-34}$$

As the incident and reflected waves are in the same medium, k_i=k_r and, $\theta_i = \theta_r$ which means that reflected and incident angles measured with respect to the normal are equal. The equation for propagation constant of a wave in a medium is given by,

$$k_m = 2\pi n_m / \lambda_0 \tag{2-35}$$

where k_m is the plane wave propagation constant in medium m, n_m is the refractive index of the medium. From Equations (2-34) and (2-35), it can be shown that,

$$n_1 . \sin\theta_i = n_2 . \sin\theta_t \tag{2-36}$$

The above Equation (2-36) is called Snell's law. The critical angle Equation (2-30) is obtained by applying Snell's law at the fibre's core-cladding interface and the Equation (2-28) for numerical aperture is obtained by the application of Snell's law at the air-core interface and from (2-30).

2.7.2 Propagation of rays and modes

A step-index optical fibre described in Section 2.6 is a dielectric cylindrical waveguide. For the sake of discussion, the core and cladding are assumed to have a radius of a and b and a refractive index of n_1 and n_2 respectively. The refractive index variation between the core and the cladding is assumed to be marginal such that $n_1 \cong n_2$. Silica fibres whose core-cladding refractive index contrast is marginal are considered to be weakly guiding [8], [9]. Propagation of rays and modes are discussed in this Section while treating the optical fibre as weakly guiding and the cylindrical coordinates used for the treatment are Radius r, azimuthal angle ϕ, which are along the z axis of the fibre [8], [9].

Rays are guided within the fibre by a phenomenon called total internal reflection previously discussed. The guided rays may be of two types, meridional rays or skew rays. The meridional rays have a plane of incidence along the fibre axis and are guided along the same plane by total internal reflection like travelling in a planar waveguide.

The skew rays on the other hand, have a ϕ component and their plane of incidence is at an angle ϕ to the core-cladding boundary. The skew rays have a helical trajectory reflecting off the planes which make an angle ϕ with the core-cladding boundary. They are confined within a radius R from the fibre axis such that $R < a$ [10], [11]. Figure 2-5 shows the propagation of rays in which meridional and skew rays are depicted in green and blue, respectively.

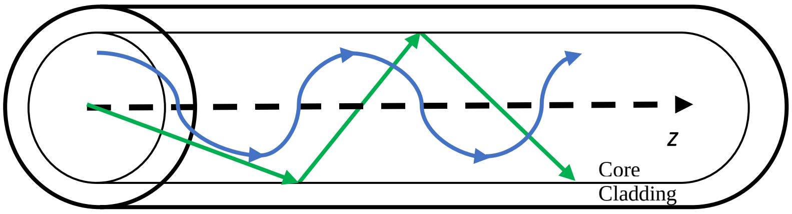

Figure 2-5: Propagation of meridional and skew rays

The optical modes are solutions to the Helmholtz equation that satisfy Maxwell's boundary conditions and are such that their spatial distribution does not change with propagation [6]. The Helmholtz equation is given by,

$$\nabla^2 E + n^2 {k_0}^2 E = 0 \tag{2-37}$$

where $k_0 = \frac{2\pi}{\lambda_0}$ is called the free-space wavenumber and n is the index of refraction. In cylindrical geometry Helmholtz equation is given by the following Equation (2-38) [10],

$$\frac{\partial^2 E}{\partial r^2} + \frac{1}{r}\frac{\partial^2 E}{\partial r^2} + \frac{1}{r^2}\frac{\partial^2 E}{\partial \phi^2} + \frac{\partial^2 E}{\partial z^2} + n^2 {k_0}^2 E = 0 \tag{2-38}$$

In the above equation, $\mathrm{E} = \mathrm{E}(r, \phi, z)$ represents axial components of E_z or H_z in cylindrical coordinates and n takes the value n_1 if $r < a$ and n takes the value n_2 if $r > a$. The waves are assumed to travel along the z axis with a propagation constant β such that [11],

$$\mathrm{E}(r, \phi, z) = F(r) e^{-jl\phi} e^{-j\beta z} \tag{2-39}$$

From equations (2-38) and (2-39), a differential equation for $F(r)$ is obtained which is given as,

$$\frac{d^2 F}{dr^2} + \frac{1}{\mathrm{r}}\frac{dF}{dr} + \left(\mathrm{n}^2 {k_0}^2 - \beta^2 - \frac{\mathrm{l}}{\mathrm{r}^2}\right) F = 0 \tag{2-40}$$

The solutions for the above equation are given by classic Bessel functions [6], [10]–[13] as the following equation,

$$F(r) = \begin{cases} J_l(k_T r), & r < a \\ K_l(\gamma r), & r > a \end{cases} \tag{2-41}$$

where $k_T{}^2 = n_1{}^2 \mathrm{k}_0{}^2 - \beta^2$ and $\gamma^2 = \beta^2 - n_2{}^2 \mathrm{k}_0{}^2$. k_T and γ are called normalized propagation coefficients that determine the rate of change of $F(r)$. $J_l(x)$ is a Bessel function of the first kind, order l and $K_l(x)$ is a modified Bessel function of second kind and order l. The sample plots of the Bessel functions are shown in Figure 2-6 where, the Bessel function $J_l(x)$ is seen to be oscillatory and the Bessel function $K_l(x)$ is seen to be monotonically decreasing.

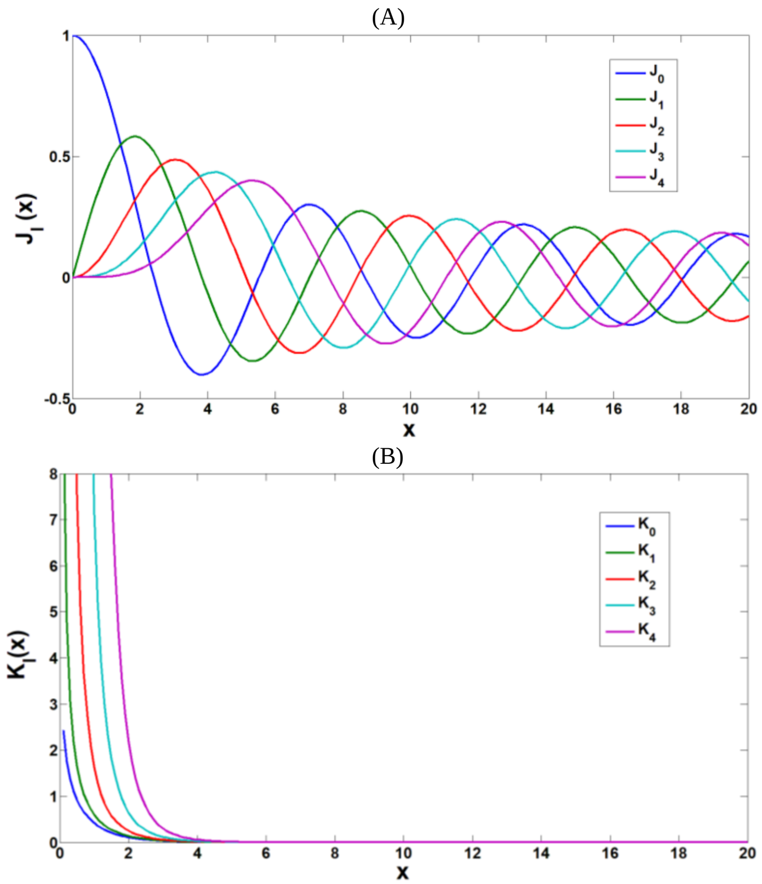

Figure 2-6: Plot of: (A) - Bessel function of the first kind and (B) Modified Bessel function of the second kind

While the function $J_l(x)$ is finite for all values of r and represents the modal fields within the core of an optical fibre, function $K_l(x)$ represents the fields in the cladding and as seen from Figure 2-6, the fields in the cladding decays with increasing distance from the core. This decaying field in the cladding is called the evanescent field. The tapered sensors used in Chapters 4-6 exploit this characteristic of light transmission through the fibre for sensing applications. The theory and operational principle of a tapered sensor is discussed in Section 2.9.3.

From Equation (2-41), solving wave equation for $\boldsymbol{H}$ and $\boldsymbol{E}$ for the z component yields,

$$E_z = \begin{cases} AJ_l(k_T r)e^{jl\phi}e^{-j\beta z}, & r < a \\ CK_l(\gamma r)e^{jl\phi}e^{-j\beta z}, & r > a \end{cases} \tag{2-42}$$

$$H_z = \begin{cases} BJ_l(k_T r)e^{jl\phi}e^{-j\beta z}, & r < a \\ DK_l(\gamma r)e^{jl\phi}e^{-j\beta z}, & r > a \end{cases} \tag{2-43}$$

The coefficients $A, B, C,$ and D are arbitrary constants connected by the boundary conditions. Transverse components E_ϕ, E_r, H_ϕ and H_r are obtained using equations (2-42), (2-43) and Maxwell's equations. The equations for the transverse components can be found in Appendix-A of this document. From the longitudinal and transverse equations and by applying boundary conditions at $r = a$, we get the following Equation (2-44) called the characteristic equation of the mode inside the optical fibre [10].

$$l^2\left(\frac{1}{\gamma^2}+\frac{1}{{k_T}^2}\right)\left(\frac{{n_2}^2 1}{{n_1}^2\gamma^2}+\frac{1}{{k_T}^2}\right) = \left[\frac{J_l'(k_T a)}{k_T J_l(k_T a)}+\frac{K_l'(\gamma r)}{\gamma K_l(\gamma r)}\right]\left[\frac{J_l'(k_T a)}{k_T J_l(k_T a)}+\frac{{n_2}^2 K_l'(\gamma r)}{{n_1}^2\gamma K_l(\gamma r)}\right] \tag{2-44}$$

As mentioned in the beginning of this section, the silica based fibres are considered to be weakly guiding and hence Equation (2-44) is simplified to get the following equation [10].

$$\pm l\left(\frac{1}{\gamma^2}+\frac{1}{{k_T}^2}\right)=\left[\frac{J_l'(k_T a)}{k_T J_l(k_T a)}+\frac{K_l'(\gamma r)}{\gamma K_l(\gamma r)}\right] \tag{2-45}$$

The characteristic equation yields multiple solutions with propagation constants $\beta_{l,m}$ for varied values of azimuthal l and each solution represents a mode [10], [11], [13]. Radial values $k_{l,m}$ and $\gamma_{l,m}$ are obtained from ${k_T}^2 = {n_1}^2{\mathrm{k}_0}^2 - \beta^2$, $\gamma^2 = \beta^2 - {n_2}^2{\mathrm{k}_0}^2$. As a result, each mode is, represented by both azimuthal and radial distributions.

A mode can be characterised by l and m. If $H_z = 0$, all field components are expressed in terms of E_z and the fields do not have any magnetic field component in the direction of propagation. This mode is called Transverse Magnetic mode (TM mode) which is represented by $TM_{l,m}$. Similarly, if $E_z = 0$, the mode is called the Transverse Electric mode (TE mode) represented by $TE_{l,m}$. There is a third category of mode called the Hybrid Mode, i.e. both H_z and E_z are non-zero in such a mode and they are represented as either $EH_{l,m}$ or $HE_{l,m}$ depending upon the dominant field. Modes in a single mode fibre are also denoted using a notation $LP_{l,m}$, where LP denotes Linearly Polarised. Polarisations in the x and y directions result in the orthogonal polarisations and the two polarisations of the same mode propagate with the same propagation constant. Linearly polarised modes may be composed of one or more of the $TE_{l,m}$, $TM_{l,m}$, $EH_{l,m}$ or $HE_{l,m}$ modes superimposed.

2.7.3 Losses in a single mode optical fibre

The attenuation of the light propagating through an optical fibre results in the reduction of signal power reaching the detector or receiver. If P_{in} is the input power of the light launched into a fibre of length L, the output power of the light P_{out} from the end of the fibre is given by [6],

$$P_{out} = P_{in}e^{-\alpha L} \tag{2-46}$$

where α is the attenuation coefficient of the fibre. The above Equation (2-46) can be re-written as shown below to express the attenuation coefficient α in dB/km.

$$\alpha = -\frac{10}{L} log_{10}\left(\frac{P_{out}}{P_{in}}\right) \tag{2-47}$$

The attenuation coefficient α in equations (2-46) and (2-47) is not confined to a particular source of power attenuation in fibre, rather it includes all sources of power attenuation for a given length of the fibre.

The power loss in an optical fibre is wavelength dependent and Figure 2-7 shows the attenuation spectrum of a single mode fibre at different wavelengths [14].

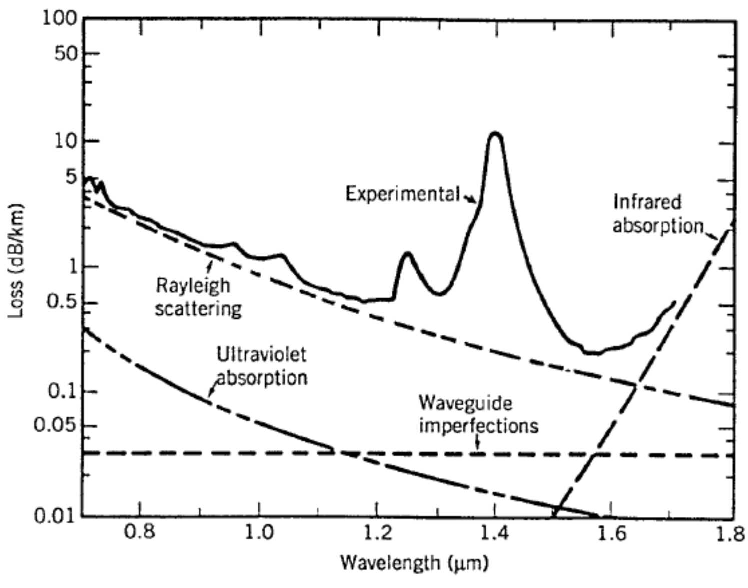

Figure 2-7: Wavelength dependent power loss in silica fibre (from [6] © 2010 Wiley)

In the Figure 2-7, the “Ultraviolet absorption” and the “Infrared absorption” lines are in fact the tails of ultraviolet and infrared absorption spectra which is beyond the scope of the figure. The 1979 study [14] found the attenuation in a silica fibre to be the lowest at 1550nm and the experimental attenuation value of 0.2dB/km was found to be in close concurrence with the theoretical value of 0.16dB/km at 1550nm.

Due to the lowest attenuation, the near infrared band centred at 1550nm is widely used by the telecoms industry. Hence, components operating in this wavelength are cheaper due to mass production. The work reported in the later chapters use this wavelength due to the lowest attenuation and low cost of the components.

The experimental works described in the subsequent chapters have all been conducted in an all-fibre environment due to its robustness and reduced vulnerability to vibrations when compared to the bulk-optic setups. However, all-fibre systems are susceptible to transmission losses that can typically be suitably minimised if not eliminated. Different factors contributing to the losses shown in Figure 2-7 are discussed in the following sections.

Absorption losses

The losses due to absorption are of two types namely, intrinsic absorptive losses and extrinsic absorptive losses. While intrinsic losses are due to the propagating lightwave’s interaction with one or more of the components used in the composition of the fibre, extrinsic losses are due to the propagating lightwave’s interaction with metal ion and OH^- ion impurities that may be present in the fibre [6], [12].

In Figure 2-7 it can be seen that the power loss due to intrinsic absorption is negligible in the 0.8μm-1.55μm (800nm-1550nm) wavelength range but the loss can be seen to be profound in wavelengths beyond 1.6μm (1600nm). The prominent loss peaks seen in Figure 2-7 at 1.24μm (1240nm) and 1.38μm (1380nm) can be attributed to the extrinsic absorptive losses due to the presence of OH^- ion impurities in the fibre. Modern day fibre manufacturing techniques have enabled fabrication of fibres with OH^- ion concentration less than 1 part per billion, thus reducing attenuation due to OH^- ions to values ≤0.2dB/km in the 1.3μm-1.6μm (1300nm-1600nm) wavelength range [12].

Radiation losses

Random variations in the density across the fibre result in refractive index fluctuations. These refractive index nonuniformities result in the scattering of the propagating light. This phenomenon of light scattering due to fibre inhomogeneities is called Rayleigh scattering [15]. The power loss due to Rayleigh scattering is given by [6],

$$\alpha_R = \frac{C}{\lambda^4} \tag{2-48}$$

where C is a constant that takes a value depending on the fibre composition and λ is the wavelength of light propagating through the fibre.

Fibre imperfections

An ideal optical fibre is expected to be a perfect cylindrical waveguide that propagates light with zero or negligible attenuation. However, the light propagating through an optical fibre attenuates due to various imperfections. Imperfections can arise during the fibre manufacturing stage or due to fibre handling related issues.

The variations in the core-cladding refractive indices during manufacturing can result in scattering of the light being transmitted through the fibre and thus result in optical power loss. Micro and macro bends in the fibre can also result in the attenuation of light being propagated. Typically, in fibre, the angle of light incident on the core-cladding interface is greater than the critical angle. However, the bends in fibre can reduce the angle of the incidence to a value lower than the critical angle resulting in the attenuation of light.

Another common source of power loss in a fibre arises from improper splicing of two or more fibres. Improper splicing can result in longitudinal, transverse, and angular misalignments of fibre. Attenuation due to longitudinal, transverse, and angular misalignment is given by the following equations,

$$\alpha = 10\log\left(1 + \left(\frac{D\lambda}{2\pi n w^2}\right)^2\right) \tag{2-49}$$

$$\alpha = 4.34\left(\frac{u}{w}\right)^2 \tag{2-50}$$

$$\alpha = 4.34\left(\frac{\pi n w \theta}{\lambda}\right)^2 \tag{2-51}$$

where D, u and θ are the longitudinal, transverse and angular misalignments, λ is the wavelength of light being transmitted, w is the spot size and n is the refractive index of the medium of gap between the misaligned fibres [12].

The experiments reported in this document are all based on an all-fibre Michelson interferometer. An all-fibre interferometric system typically uses a myriad of components such as couplers, isolators, etc. The principle optical components used in the experimental works are described in the following section.

2.8 Optical fibre components

In-line fibre optic components are critical to optical fibre based systems for the manipulation of optical signals. There are several different passive optical components such as couplers, filters, splitters, attenuators, phase shifters and modulators, wavelength division multiplexers (WDM), isolators, circulators, etc. This section is focussed on the discussion of only the coupler, the isolator, the circulator, and the phase shifter which are used in the construction of the fibre optic interferometric interrogation system described in the experimental sections.

2.8.1 Optical couplers

The fibre optic directional couplers or just fibre optic couplers are one of the most used in-line fibre optic components for splitting or combining of optical signals. Based on the fabrication methods, the couplers may be of several types such as etched couplers, polished couplers, and fused couplers. The characteristics of the different directional couplers have been compared by Digonnet and Kim [16]. Based on the performance characteristics and due to the low cost, fused couplers have been preferred over the other coupler types to be used for the construction of the interferometer described in experimental Chapters 3-6.

The working principle of a coupler is as follows. The mode field of the guided mode in an optical fibre extends beyond the core-cladding interface. As a result, when two fibre cores are fused together laterally, the two fibre's modal fields overlap resulting in the coupling between the two fibre's modes and thus results in a periodic transfer of power between the two fibres [12], [17].

The power of the light; launched into the first fibre is denoted by P_s, transmitted is denoted by P_t, coupled into the second fibre is denoted by P_c, reflected back into the first and second fibres are denoted by P_{ref} and P_{ret} respectively. For a coupler fabricated using fibres with similar propagation constant, the power of light in the first and second fibre is given by,

$$P_t(z) = P_s \cos^2 kz \tag{2-52}$$

$$P_c(z) = P_s \sin^2 kz \tag{2-53}$$

where k is called the coupling coefficient, which is a measure of the strength of the interaction between the fibres used for designing of the coupler [12]. By using different values of k the coupler can be used as a wavelength division multiplexer and couplers for a fixed wavelength band will have the same or similar k values. Another parameter used for characterising the coupler is the coupling ratio, which is the ratio between the optical power from the output port and the input optical power. The coupling ratio is given by,

$$\alpha = \frac{P_c(z)}{P_s(z)} \tag{2-54}$$

The imperfections in the fused region result in the reflections back to the input ports which are given by the following expressions, where $D_r(z)$ and $R_{ref}(z)$ are the directionality and reflection respectively [17].

$$D_r(z) = \frac{P_{ret}(z)}{P_s(z)} \tag{2-55}$$

$$R_{ref}(z) = \frac{P_{ref}(z)}{P_s(z)} \tag{2-56}$$

Typically, couplers have varying coupling ratios such as 50:50, 25:75, 10:90. In addition to coupling ratio, the couplers are characterized by directionality and are either mono-directional or bi-directional. The sensor interrogation schemes described in experimental Chapters 3-6 employ 50:50 bidirectional couplers for illuminating the interferometer with a broadband source and then for illuminating the sensors with the output of the interferometer.

2.8.2 Optical isolators

Optical isolators are fibre components that allow the propagation of light in only one direction. It is often used to stop undesired reflections in a fibre optic setup. The optical isolators are divided into two types, polarisation dependent and polarisation independent [17].

A polarisation dependent isolator is made up of three components, an input polariser, a Faraday rotator, and an output polariser. In a polarisation dependent isolator, the input optical beam first passes through the input polariser whose optical axis is along the vertical direction. The beam then passes through the Faraday rotator which rotates the polarisation of the beam by 45^0. The polarisation rotated beam then passes through the output polariser whose optical axis is at 45^0 to match the beam from the Faraday rotator. In the case of a reflection, the reflected beam passes through the output polariser and gets rotated again by 45^0 in the same direction as before by the Faraday rotator. This beam from the Faraday rotator is now perpendicular to the optical axis of the input polariser and thus gets blocked.

The main drawback of using a polarisation dependent isolator is that the optical axis of the polarisers has to be carefully matched with the state of polarisation of the optical beams which otherwise would lead to attenuation of the signal [17]. This drawback of the polarisation dependent isolator can be overcome by using polarisation independent isolator which uses birefringent beam displacers instead of the polarisers.

In the experiments described in Chapters 3-6, a low coherence interferogram generated by an all-fibre interferometer is used to illuminate the sensing arms and the interferogram modulated by the sensors are then processed for results. To prevent the coupling of back reflections from the downstream sensing arm with the upstream sensing arm, polarization independent isolators have been used in the setups.

2.8.3 Optical circulators

Optical circulators like isolators also operate based on the polarisation of the optical beam using a Faraday rotator. A typically used optical circulator comprises of three ports. Port 1 is the input port for the optical signal, port 2 is the output port and the optical signal reflected into port 2 is directed to port 3. Figure 2-8 shows a diagram of the working of the circulator. The optical circulators are widely used in fibre optic sensor sensing setups where the sensor connected to port 2 is illuminated using an optical source via port 1 and the reflection from the sensor is interrogated using a system such as an optical spectrum analyser connected to port 3.

In the experimental configurations described in the later chapters of this document, the broadband source is connected to Port 1 of the circulator, the all-fibre Michelson interferometer is connected to Port 2 and one of the sensing arms to Port 3. This configuration permits the illumination of the interferometer with the broadband source and allows access to two output arms of the interferometer.

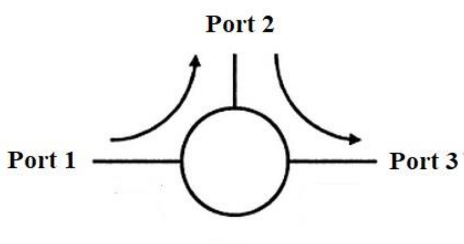

Figure 2-8: Working of a three port optical circulator

2.8.4 Phase modulators

Fibre optic phase modulators have been widely used in the fibre based interferometric setups. They are used for introducing an optical path delay in an interferometer or heterodyning for extremely sensitive measurements. Phase modulation is achieved by axial elongation of the fibre or by inducing radial stress on the fibre.

Most used phase modulator is a lead zirconate titanate (PZT) cylinder with several turns of fibre tightly wound around it. When a voltage is applied across the terminals of the piezoelectric cylinder, the cylinder dilates and induces a phase change by axial elongation of the fibre. This type of phase modulator is also known as a fibre stretcher [16].

(A)

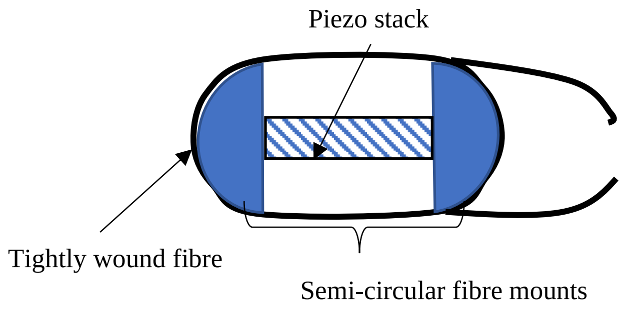

(B)

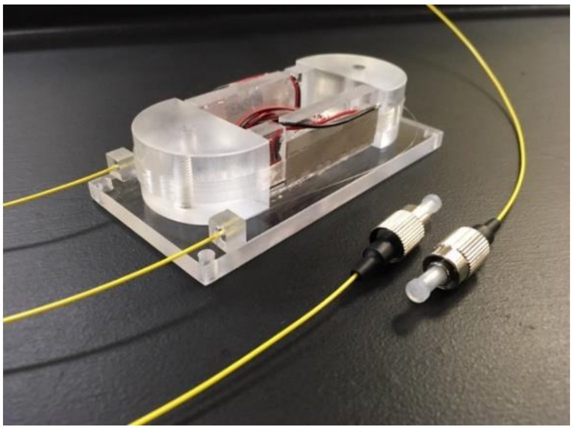

Figure 2-9: Fibre stretcher (A) Diagram and (B) Picture © www.evanescentoptics.com

In the experimental works reported in Chapters 3-6, a fibre stretcher, composed of several rounds of fibre wrapped around two semi-circular structures with a piezo stack placed between them is used to scan the optical path delay in the interferometer. In case of this type of a stretcher, the excitation of the piezo stack elongates and stretches the fibre. Figure 2-9 shows the picture and diagram of one such stretcher, similar to the one used in the experiments.

The phase change induced using the fibre stretchers is given by the Equation (2-57),

$$\Delta\varphi = \frac{2\pi}{\lambda}(n\Delta l + \Delta n l) \tag{2-57}$$

where λ is the wavelength of light used to illuminate the stretcher, n and l are fibre's refractive index and length respectively [16]. In the next section, after a brief introduction to fibre optic sensors' classification and types, the theory, the operational principle, the manufacturing methods, etc. of the two sensor types (FBG sensor and tapered sensor) used in the experimental work is elaborated.

2.9 Optical fibre sensors

Optical fibre sensors, also called as Fibre Optic Sensors (FOS) are optical fibres in which the light guided within can be modulated in response to an external physical, chemical, biological or any other such stimulus [16]. They pose numerous advantages over conventional sensors like small size, high flexibility, immunity from electromagnetic interference, inherent safety, etc.

Depending on the sensing location, a FOS can be classified as either extrinsic or intrinsic and depending on the type of modulation that the light undergoes, a FOS can be classified as a phase sensor, a frequency sensor, an intensity sensor or a polarisation sensor. Based on the operating principles, FOS can be classified as interferometric sensors, distributed sensors, and grating based sensors. The sub-classification is shown below in Figure 2-10. The advantages, disadvantages, and characteristics of the different FOS have been compared by Di Sante [18] and Lee *et al.* [19] have in particular compared the different interferometric sensors. The work reported in this document employs only Fibre Bragg grating sensors and non-adiabatic tapered sensors which belong to the class of grating based sensors and interferometric sensors respectively. The term "tapered sensor" in the experimental chapters denotes the non-adiabatic type tapered sensor which is explained further in Section 2.9.3.

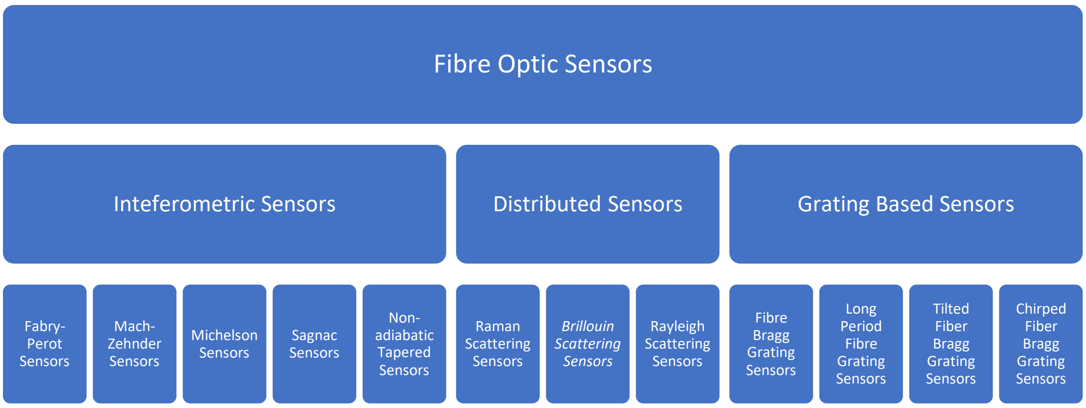

Figure 2-10: Classification of fibre optic sensors

2.9.1 Distributed sensors

The distributed sensors work on the principles of elastic and inelastic scattering. In a distributed sensor, the entire fibre is a sensor and as the name suggests, they are used for sensing the parameter of interest at separate locations along the fibre length. Distributed sensors work on Rayleigh scattering, Brillouin scattering, and Raman scattering. They are more suited for long distance, multi-point sensing and are unsuitable for single-point sensing applications, unlike the interferometric and grating based sensors.

The work reported in this document is extensively based on fibre Bragg grating sensor and tapered sensor interrogation and hence, only these two sensor types are discussed in detail in the following sections.

2.9.2 Fibre Bragg grating sensors

A Bragg grating is an optical device with periodic changes in the refractive index which when illuminated with a broadband of light reflects a bandwidth of light characteristic to the device. The bandwidth of light reflected by a grating is characterised by its pitch and period. A Bragg grating inscribed on a photosensitive optical fibre by exposing the core to an intense optical interference pattern is called a fibre Bragg grating (FBG) [1], [20], [21]. Fibre Bragg gratings are sensitive to strain, temperature, vibration, pressure, etc. and hence used as sensors. The theory behind FBGs and their working are elaborated in the following sections.

Coupled Mode Theory

The working of an FBG sensor is best described by the coupled mode theory [22]. The Coupled mode theory (CMT) in electromagnetics can be dated back to the 1950s when it was first used in the analysis of microwaves [23]. The CMT for optical waveguides was developed in the 1970s [25]–[32] and was later applied to Bragg reflectors and grating waveguides [32]–[35]. For an understanding of CMT with reference to an FBG, the waveguide is assumed cylindrical and the direction of propagation of the wave is assumed to be along the z-axis. The following treatment follows the work reported by Erdogan [36]. The refractive index profile n(z), along the grating, can be given by [36],

$$\delta n_{eff}(z) = \overline{\delta n_{eff}}(z)\left[1 + \cos\left(\frac{2\pi}{\Lambda}\mathrm{z}\right)\right] \tag{2-58}$$

where $\overline{\delta n_{eff}}$ is the refractive index perturbation over the grating period. Based on the above equation, the reflectivity of a grating is given by,

$$r = \frac{\sinh^2(L\sqrt{k^2 - \hat{\sigma}^2})}{\cosh^2\left(L\sqrt{k^2 - \hat{\sigma}^2}\right) - \frac{\hat{\sigma}^2}{k^2}} \tag{2-59}$$

where L is the length of the grating, k is the AC coupling coefficient and $\hat{\sigma}$ is the DC coupling coefficient. The coupling coefficients can be expressed as,

$$k = \frac{\pi\overline{\delta n_{eff}}}{\lambda} \tag{2-60}$$

and

$$\hat{\sigma} = \delta + \sigma \tag{2-61}$$

The σ and δ are given by,

$$\delta = 2\pi n_{eff}\left(\frac{1}{\lambda} - \frac{1}{\lambda_D}\right) \tag{2-62}$$

$$\sigma = \frac{2\pi\overline{\delta n_{eff}}}{\lambda} \tag{2-63}$$

For a uniform grating δn_{eff} is constant and so, σ too is constant. For maximum coupling, detuning δ, is equal to 0 [37] and thus, λ=λ_D, where $\lambda_D = 2n_{eff}\Lambda$ and is called the design wavelength. Thus, now the Equation (2-62) can be re-written as,

$$\lambda = 2n_{eff}\Lambda \tag{2-64}$$

λ in Equation (2-64) is called the Bragg wavelength.

The operational principle of a fibre Bragg grating

An FBG can be compared to an electrical/electronic stop-band filter or band-reject filter. The inscribed grating reflects a wavelength of light characteristic to it while transmitting all other wavelengths. The reflected wavelength is given by the above Equation (2-64) with an added subscript to the λ term. The expression as given in the literature [38] is,

$$\lambda_B = 2n_{eff}\Lambda \tag{2-65}$$

where λ_B is the Bragg wavelength, n_{eff} is the effective refractive index of the fibre and Λ is the period of the grating. Figure 2-11, shows the operation of an FBG in both reflection and transmission mode.

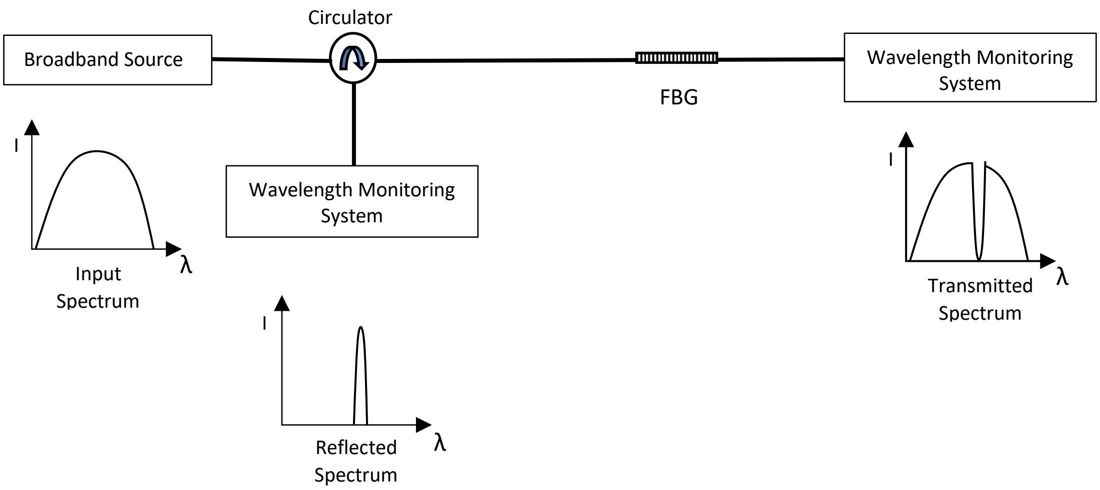

Figure 2-11: FBG system in reflection and transmission mode

Physical forces like temperature and strain acting on an FBG cause a shift in its Bragg wavelength. This wavelength shift is due to a change in the period of the grating. While the strain induced change in period of the grating is caused by the photoelastic effects of fibre, the temperature induced change in period is due to thermal expansion of the fibre and change in refractive index due to temperature. By monitoring the direction and level of shift in the Bragg wavelength, the physical force(s) acting on the grating can be quantified. Hence, the Bragg grating is called a Bragg grating sensor or a fibre Bragg grating sensor.

The sensitivity of the Bragg wavelength to strain and temperature is given by the following Equation (2-66),

$$\frac{\Delta\lambda_B}{\lambda_B} = (1 - \rho_e)\Delta\varepsilon_z + (\alpha + \eta)\Delta T \tag{2-66}$$

where ρ_e is the photoelastic coefficient of the fibre, α is the thermal expansion coefficient of the fibre, η is the thermo-optic coefficient of the fibre [39].

Equation (2-66) can be substituted with the following values of photoelastic coefficient, thermal expansion coefficient and thermo-optic coefficient that correspond to a silica fibre illuminated with a broadband source of 1550nm central wavelength [40].

$$\rho_e = 0.22$$
$$\alpha = 0.55\text{x}10^{-6}/^0\text{C}$$
$$\eta = 8.6\text{x}10^{-6}/^0\text{C}$$

Now, the temperature sensitivity obtained at zero strain is given by,

$$\frac{\Delta\lambda_B}{\Delta T} = 14.18\text{pm}/^0\text{C}$$

and the strain sensitivity at constant temperature is given by,

$$\frac{\Delta\lambda_B}{\Delta\varepsilon} = 1.2\text{pm}/\mu\varepsilon$$

Fabrication of fibre Bragg gratings

Traditionally, FBGs were fabricated from within the fibre core by using a laser in the visible wavelength. This method of an FBG fabrication also called as internal writing was first demonstrated by K. O. Hill and hence the gratings fabricated using this procedure were called “Hill Gratings” [41]–[43]. The main drawback of this method was that the fabricated gratings worked only at the writing wavelength. However, this limitation was later overcome using external grating writing methods.

The external grating writing or fabrication methods are broadly classified as either interferometric or non-interferometric. In the interferometric method of an FBG fabrication first demonstrated by Meltz [44], a beam of UV light is split using a beam-splitter and then combined at an angle on the fibre after being reflected off a pair of mirrors. The wavelength of light reflected by an FBG fabricated using this method is dependent of the wavelength of UV beam used. The Bragg wavelength λ_B of an FBG fabricated using this technique is given by [1],

$$\lambda_B = \frac{\eta_{eff}\lambda_{UV}}{n_{UV}\sin\left(\frac{\theta}{2}\right)} \tag{2-67}$$

where η_{eff} is the effective mode index in the fibre, n_{UV} is the refractive index of the core at ultraviolet (UV) wavelength, λ_{UV} is the wavelength of UV light used for an FBG fabrication and θ is the angle of interference of the UV beams on the fibre. Thus, the Bragg wavelength can be varied by varying the θ. The interferometer is susceptible to vibrations and disturbances and changes to the pathlength of the interfering beams would result in a drift of the interference fringes formed at the fibre. The limitations of the interferometric method of writing gratings can be overcome by using the non-interferometric method.

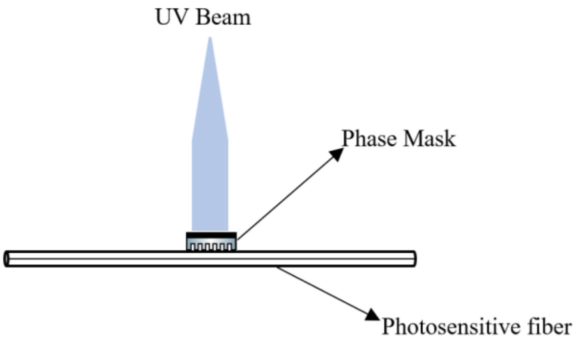

Figure 2-12: Setup to write an FBG using a phase mask.

In the non-interferometric method of an FBG writing, a phase mask permits the writing of FBGs using the principle of diffraction. The phase masks are UV light transmitting silica plates with grooves etched on them. A typical setup for writing FBGs using phase mask is shown in Figure 2-12. After placing the phase mask very close to the photosensitive fibre, when a beam of UV light is incident normal to the phase mask, the diffracted zero order and ±1 order modes of the UV beam write a grating on the photosensitive fibre core. The grating in the fibre core is due to the interference of the zero order, +1 order and -1 order modes of the UV beam diffracted by the phase mask. As a result, the period of the grating inscribed is twice the period of the phase mask grooves. The depth and the spacing of the phase mask grooves determine the period of the grating inscribed on the fibre. The period of the grooves on the phase mask Λ_{pm}, the period of the grating inscribed Λ_g and the Bragg wavelength λ_B of the written FBG are related by the following expression [1].

$$\Lambda_g = \frac{\lambda_B}{2\eta_{eff}} = \frac{\Lambda_{pm}}{2} \tag{2-68}$$

Classification of fibre Bragg gratings

Based on the nature of the inscribed gratings and the photosensitivity of the fibre, the gratings are broadly classified as Type-I, Type-Ia, Type-II, and Type-IIa. The grating types use either a hydrogenated fibre or a non-hydrogenated fibre. Hydrogenation of a fibre is a process by which hydrogen atoms are loaded/diffused into the photosensitive fibre’s core. Hydrogen loading is performed by exposing the photosensitive fibre to pressurized hydrogen gas for prolonged duration.

The commonly used fibre grating that is written on either a hydrogenated or a non-hydrogenated fibre using a low power laser source is called the Type-I grating. A Type- I grating is stable up to a temperature of about 300^0C [45].

A Type-Ia grating is normally written in a hydrogenated fibre. The continued exposure of a Type-I grating to the writing beam results in its growth, which is followed by its saturation, decay, and erasure. The grating that regenerates after the erasure of the Type-I grating is called the Type-Ia grating. The Type-Ia grating has a temperature stability higher than the Type-I grating [45].

Unlike Type-I gratings, which are written using a low power writing beam, a Type-II grating is written using a laser beam of high power ~30mJ such that even the core of the fibre gets damaged during the writing process [46]. As a result of the damage caused to the fibre, Type-II gratings are also called as damaged gratings. Type-II gratings can withstand extremely elevated temperatures in the lines of ~700-800^0C because of the physical damage.

The process of writing the Type-IIa grating is the same as the process of writing the Type-Ia grating where the continued exposure to the writing beam results in the erasure of a saturated Type-I grating and regeneration of another grating. Unlike a Type-Ia grating, a Type-IIa grating is written on a non-hydrogenated fibre.

By varying the angle, period, index, and length of the grating inscribed on a fibre, FBGs with distinctive characteristics can be produced. Distinct types of fibre Bragg gratings or fibre Bragg grating sensors are discussed in the following section.

Types of fibre Bragg gratings

The grating period of a typical FBG is few hundreds of nanometres, but Long Period Fiber Bragg Grating (LPFBG) has a grating period in the range of few microns to a few hundred microns. The larger grating period results in an increased sensitivity to strain, temperature, torsion, bending and changes to the refractive index of the surrounding medium.

Chirped Fiber Bragg Gratings (CFBG) are produced by varying the period of grating along the axis of the fibre core. This results in an increased reflected light bandwidth. CFBGs are commonly used for filtering applications in the telecoms industry.

Tilted Fiber Bragg Gratings (TFBG) are created by inscribing the grating at an angle to the fibre axis. The differential geometry of the grating with respect to the fibre core results in multiple spectral peaks that are sensitive to the refractive index of the surrounding medium.

The refractive index sensitivity of the LPFBG and the TFBG arises due to the coupling of the mode(s) reflected by the grating with the higher order cladding modes. Due to the refractive index sensitivity, LPFBGs and TBGs are widely used in humidity sensing, bio-sensing, liquid sensing applications, etc.

The experimental work described in Chapters 3-6 of this document, uses one or more of the FBG sensors or a combination of FBG sensors and tapered sensors. The FBG sensors used in the experiments described later in this document are typically manufactured using the above discussed non-interferometric phase mask based inscription method and subsequently coated with a polymer coating. A typical FBG sensor's: theory, operational principle, manufacturing methods, and classification were discussed in the above sections. The following section details the theory, operational principle, and manufacturing methods of the tapered sensor.

2.9.3 Tapered fibre optic sensors

The optical fibres that create interferograms whose properties are sensitive to varying physical forces like temperature, strain, etc. are called fibre optic interferometric sensors (FOIS) [21]. FOIS are named after the interferometric principle they are based on. For example, a FOIS using, Fabry–Pérot interferometry is called a Fabry–Pérot Interferometric Sensor (FPIS) and Mach–Zehnder interferometry is called Mach–Zehnder Interferometric Sensor (MZIS). Based on the structure of the fibre there is another type of FOIS called the tapered sensor (TS) which is described below.

In accordance with Maxwell's boundary conditions, in a typical single mode optical fibre, even though the fundamental mode is confined within the fibre core, a field of energy extends beyond the fibre core into the cladding. The field of energy extending beyond the fibre core is called the evanescent field or the evanescent waves as referred to in the literature.

The intensity of the evanescent waves decays exponentially with increasing distance within the cladding as per the Bessel function of second kind described in Section 2.7.2. Thus, to expose the evanescent waves, the diameter of the cladding is reduced by tapering the fibre. The typical structure of a tapered fibre/sensor is shown in Figure 2-13 in which, the fibre can be seen to have a section of reduced diameter. The following section describes the various techniques employed for tapering a fibre.

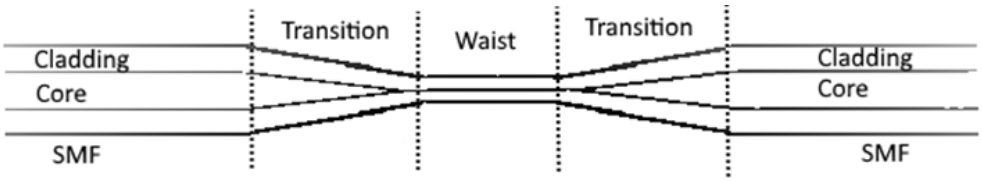

Figure 2-13: Structure of a tapered fibre sensor

Tapered sensor fabrication

The different methods to fabricate tapered sensors include side polishing, etching, stretching while heating, etc. The common and cost-effective methods for fabricating tapered sensors are by vertical and horizontal tapering [47].

The vertical tapering is like the fibre drawing process, the optical fibre is held vertically fixed at one end and a mass is tied on it at the other end. When a section of the buffer stripped fibre is heated, the weights pull the fibre down, thus causing the fibre to taper. A pictorial representation of the vertical tapering process is shown in Figure 2-14.

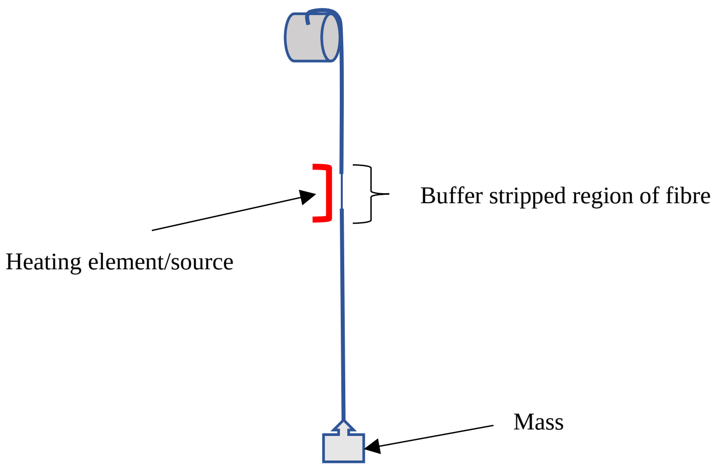

Figure 2-14: Vertical fibre tapering

In the case of horizontal tapering, the buffer stripped section of the fibre is heated to its softening temperature and the ends of the fibre are simultaneously pulled horizontally to produce the taper. Of the two above mentioned tapering methods, the horizontal tapering offers better control of the tapering process, as the taper dimensions can be controlled by controlling the stretcher motor speed, position, and acceleration. A pictorial representation of a horizontal tapering station/process is shown in Figure 2-15.

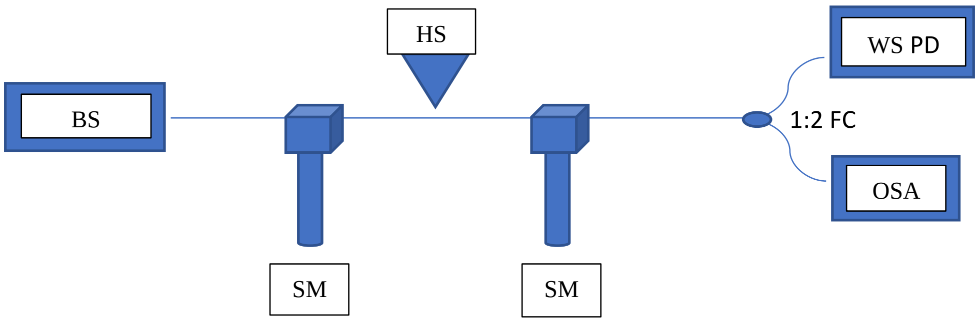

Figure 2-15: Horizontal fibre tapering

In Figure 2-15, BS denotes a broadband light source, SM denotes a stretcher motor (pulling motor), HS denotes the heat source, 1:2 FC denotes a 50:50 fibre coupler WS PD denotes the workstation photodiode which continuously monitors the intensity of light emitted by the fibre and OSA denotes the optical spectrum analyser used for continuous monitoring of the spectra while tapering the fibre. The components of a system may however vary depending on the sophistication and the specification of the tapering system.

The tapered sensors used in the experiments described later in this document were fabricated using the horizontal fabrication process on a fibre coupler workstation (E-TEK FCPW-2000) whose image in shown in the figure below. Tapered sensors with different characteristics can be fabricated with either of the above outlined methods. Classification of the tapered sensors based on the taper characteristics is presented in the next section.

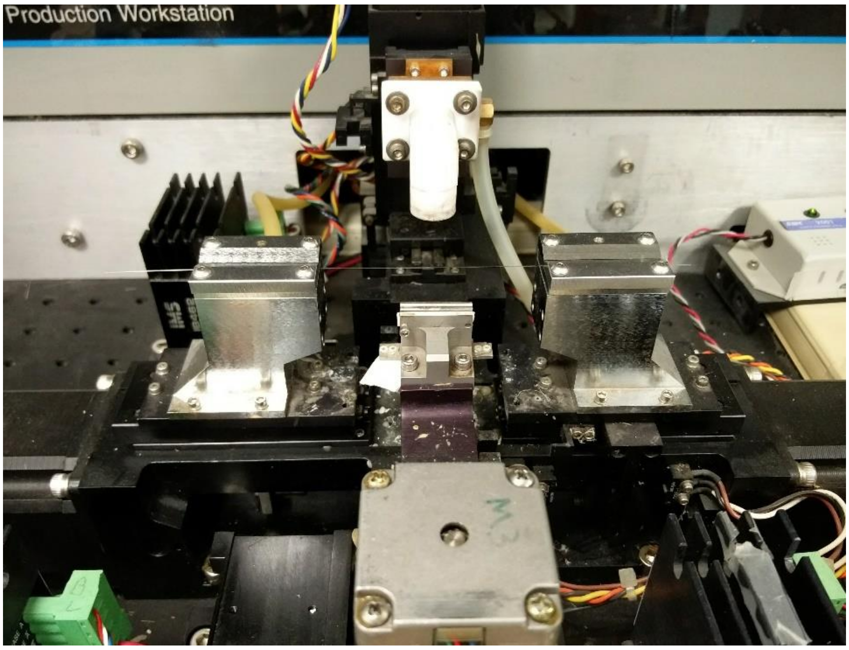

Figure 2-16: Image of the fibre coupler production station used

Tapered sensor types

Irrespective of the method used for tapering a fibre, the tapered sensor based on the taper characteristics is classified as either an adiabatic tapered sensor or a non-adiabatic tapered sensor.

In an adiabatic tapered sensor, the taper transition angle is small and almost all the fundamental mode's energy is confined within the core. As a result of this confinement, energy does not couple into the higher order modes and hence, the losses are lower when compared to the non-adiabatic sensor.

A non-adiabatic tapered sensor when compared to the adiabatic tapered sensor, has a larger taper transition angle. As a result, the energy from the fundamental mode couples with the higher order modes resulting in higher losses to the fundamental mode's energy and interference between the higher order modes and the fundamental mode at the transition region. Due the inter-modal interference, the non-adiabatic tapered sensors are also called as Mach–Zehnder fibre interferometers or modal fibre interferometers or interferometric tapered sensors. The non-adiabatic tapered sensors are characterized by the fringes in their spectrum as shown in Figure 2-17. The free spectral range (FSR) or the fringe width of a non-adiabatic sensor's spectral fringes are dependent on the sensor's taper characteristics.

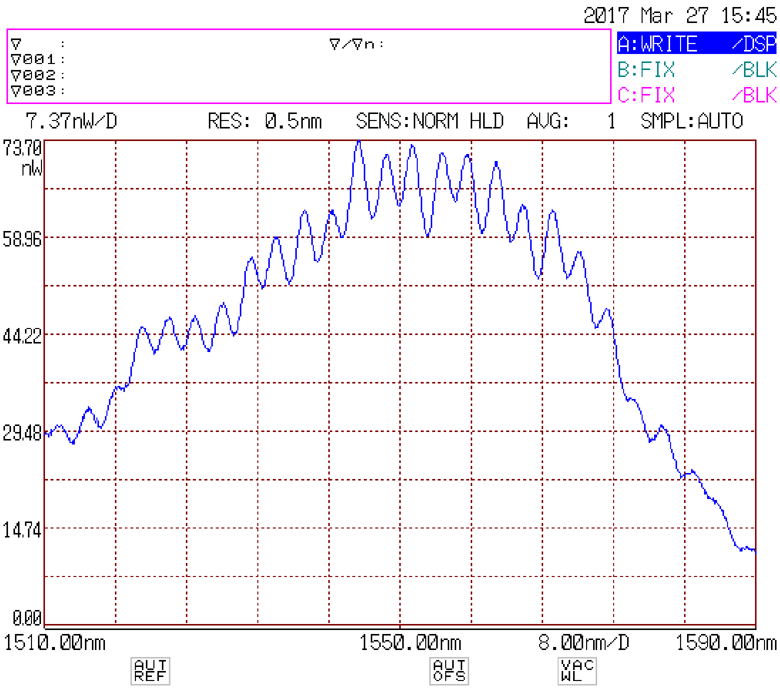

Figure 2-17: A non-adiabatic tapered sensor spectrum

The tapered sensors used in the later experimental chapters are non-adiabatic type with different spectral fringe widths. The measurements using a non-adiabatic tapered sensor are based either on the evanescent wave power loss across the tapered region or on the change in phase of the higher order cladding modes. As a result, by continuously monitoring a tapered sensor's spectrum, changes to the environment surrounding the sensor can be quantified from the changes to the sensor's spectrum. Thus, a tapered optical fibre can be used for varied sensing applications. The principle behind the operation of a tapered sensor i.e. the evanescent wave theory is described in the next section.

Evanescent wave theory

Propagation of the light wave has already been discussed in Section 2.7.2. The treatment of evanescent wave theory in this section closely follows the work of John [48] and O'Keeffe [7]. As discussed previously, the electromagnetic wave incident on the boundary of the media is given by Equation (2-37) [49], [50]. As per Maxwell's boundary conditions, the tangential components of E and H and the normal components of D and B are continuous across the core-cladding boundary. Solutions to the wave equation yields Fresnel's equations that deal with the magnitudes of the transmitted and reflected electric fields with respect to the incident electric field. The Fresnel's equations serve as mathematical proofs for the total internal reflection phenomenon.

$$\frac{E_r^{\perp}}{E_i^{\perp}} = \frac{n_1 \cos\theta_i - n_2 \cos\theta_t}{n_1 \cos\theta_i + n_2 \cos\theta_t} \tag{2-69}$$

$$\frac{E_r^{\parallel}}{E_i^{\parallel}} = \frac{n_1 \cos\theta_t - n_2 \cos\theta_i}{n_1 \cos\theta_t + n_2 \cos\theta_i} \tag{2-70}$$

$$\frac{E_t^{\perp}}{E_i^{\perp}} = \frac{2n_1 \cos\theta_i}{n_1 \cos\theta_i + n_2 \cos\theta_t} \tag{2-71}$$

$$\frac{E_t^{\parallel}}{E_i^{\parallel}} = \frac{2n_1 \cos\theta_i}{n_1 \cos\theta_t + n_2 \cos\theta_i} \tag{2-72}$$

In the above equations, $E^{\parallel}$ and $E^{\perp}$ are the electric field vectors parallel and perpendicular to the plane of incidence, respectively. Under the circumstances of total internal reflection, i.e., when $\theta_i > \theta_c$, where $\theta_c = \sin^{-1}\frac{n_2}{n_1}$, there will be no transmitted wave in the second medium. Although all the energy in the beam is reflected due to total internal reflection, there will still be a disturbance in the second medium, whose electric field amplitude decays exponentially with distance away from the boundary. The expression for the decay of the evanescent wave can be derived by considering the transmitted wave at a point 'r' as per the following equation,

$$P = e^{i(\omega t - k_t . r)} \tag{2-73}$$

where k_t is the wave vector associated with the transmitted wave.

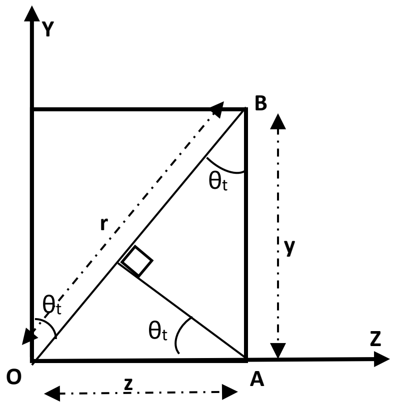

Figure 2-18: Relationship between the rectangular coordinates

From Figure 2-18, r may be written as r = z sin θ_t + y cos θ_t and substituting this in phase vector equation, we get,

$$P = e^{i[\omega t - k_t \,(\mathrm{z} \sin \theta_t + \mathrm{y} \cos \theta_t)]} \tag{2-74}$$

and by substituting Equation (2-35) in the above equation, we get,

$$P = e^{i\left[\omega t - \frac{2\pi n_2}{\lambda_0}\,(z \sin \theta_t + \mathrm{y} \cos \theta_t)\right]} \tag{2-75}$$

where λ_0 is the wavelength of radiation in vacuum and cos θ_t values can be obtained using the mathematical identity of ($sin^2\theta + cos^2\theta = 1$).

$$\cos \theta_t = \sqrt{(1 - \sin^2 \theta_t)} \tag{2-76}$$

Using Snell's Law equation of light ray incident on the boundary in the above equation,

$$\cos\theta_t = \sqrt{\left(1-\left(\frac{n_2}{n_1}\right)^2 \sin^2\theta_i\right)}$$

(2-77)

when $\theta_i > \theta_c$, $\sin\theta_i > \frac{n_2}{n_1}$, $\cos\theta_t$ the becomes imaginary.

$$\cos\theta_t = \pm i\sqrt{\left(1-\left(\frac{n_2}{n_1}\right)^2 \sin^2\theta_i\right)}$$

(2-78)

Substituting, $\sqrt{(1-\left(\frac{n_2}{n_1}\right)^2 \sin^2\theta_i)}$ = B in the above equation, it becomes,

$$\cos\theta_t = \pm iB$$

(2-79)

Substituting Snell's law Equation (2-36) discussed in Section 2.7.1 and $\cos\theta_t$ from Equation (2-79) in the phase (2-74) we get,

$$P = e^{i[\omega t - \frac{2\pi n_2}{\lambda_0}(\mathrm{z}\frac{n_1}{n_2}\sin\theta_i + (\pm iB))\mathrm{y}]}$$

(2-80)

$$P = e^{i\left[\omega t - \frac{2\pi n_1 \sin\theta_i}{\lambda_0}\mathrm{z}\right]}\, e^{\left[\pm B\frac{2\pi n_2}{\lambda_0}\mathrm{y}\right]}$$

(2-81)

Thus, in the y-direction, the wave either grows or decays exponentially with distance, as previously shown with the modified Bessel function of the second kind in Section 2.7.2. The decay is given by factor D(y), where

$$D(y) = e^{\left[-B\frac{2\pi n_2}{\lambda_0}\mathrm{y}\right]}$$

(2-82)

Normally, D(y) decays rapidly with y. But, when θ_i is close to θ_c, the value of B will be close to zero and the wave may extend into the second medium. This part of the wave in the second medium is the evanescent wave. Due to effects like scattering and absorption, the evanescent field power will vary based on its interaction with the external environment. By measuring the evanescent field power loss across the tapered region, information about the external environment can be inferred. Hence, tapered sensors are used for label-free detection of analytes in bio-sensing [51], [52], gas sensing [53]–[58] and chemical sensing [59], [60] applications.

In the following section, after a brief discussion on interferometry and interferometers, key interferometric measurement techniques (FTS and HTT) used in the experimental work are described.

2.10 Fibre optic sensor interrogation

Numerous interrogation schemes for interrogating individual FBGs, and multiplexed FBG arrays, using wavelength division coupler [63], tunable filters [62],[63], tunable laser [64], arrayed waveguides [65]–[67], etc. have been demonstrated with varied resolutions and multiplexing capabilities. The tapered fibre optic sensors are typically interrogated with an OSA, spectrometer, optical power meter [47], [51], [52], [68], [69]. When compared to other fibre optic sensor interrogation techniques, interferometric interrogation offers numerous advantages which are discussed in Section 2.10.3. The following section discusses the concept of interferometry and interferometers in detail.

2.10.1 Interferometry

Interferometry is a measurement technique derived from the phenomenon of interference. The instrument used in interferometry is called an interferometer. Albert Michelson first demonstrated the concept of interferometry in the 1880s using a two-beam interferometer.

Although technology has developed over the years, Michelson interferometers remain at the core of interferometry. Generally, interferometers are classified based on the number of beams and the method of beam separation. Due to scientific advancements, interferometers have evolved over a period. The newer interferometers can be sub-classified based on; source, separation of beams, number of passes and order of correlation [70].

2.10.2 Interferometers

Some of the common two-beam interferometers are either based on wavefront division or amplitude division [20]. In the case of wavefront division interferometers, no beam splitters are used, instead, two slits like in the case of Young’s double-slit experiment, are used for producing interference patterns. Few examples of wavefront division interferometers include Fresnel’s double mirror, Fresnel’s double prism, Rayleigh interferometer, and Lloyd’s mirror. In case of amplitude division interferometers, a single beam is split into two using a beamsplitter. The divided beams are then superposed to form interference patterns. Examples for amplitude division interferometers are Michelson interferometer, Mach-Zehnder interferometer, and Sagnac interferometer. The experimental works described in this thesis make use of Michelson and Mach-Zehnder interferometric principles. Schematic representations of these two interferometer setups are shown in Figure 2-19. In the setups, M, BS, and D denote a mirror, a beam-splitter, and a detector, respectively.

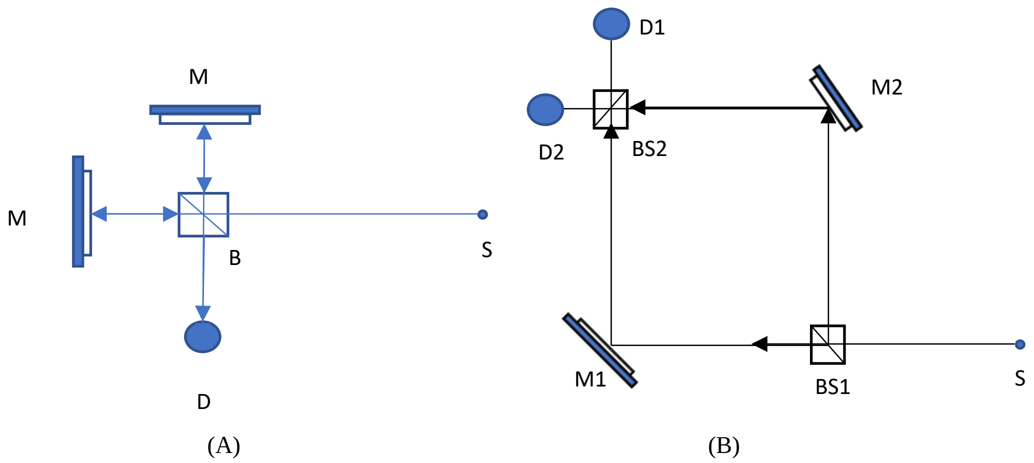

Figure 2-19: (A) - Michelson interferometer, (B) - Mach-Zehnder interferometer

In a Michelson interferometer, displacement of either of the mirrors causes a change in fringe order. The change in fringe order Δm, the wavelength of the incident beam λ and the mirror displacement d are related by the following equation,

$$\Delta m \, \lambda = 2d \tag{2-83}$$

With a known optical path difference created by the mirror and from the observed change in fringe order, the wavelength of the incident beam can be computed using Equation (2-83). This underlying principle of Michelson interferometer forms the basis for the interrogation of optical sensors using interferometry.

In case of the Mach-Zehnder interferometer, the optical path length d of the beams is given by, $d = nL$, where n denotes the refractive index of the medium in which the beams travel and L is the physical path length. With the introduction of an additional component in the path of one of the beams, the physical path length remains the same, but the optical path length changes. The optical path difference Δd created between the two beams is given by, $\Delta d = \Delta nL$, where Δn denotes the difference in the refractive indices of the mediums in which the beams travel and L is the physical path length. This optical path difference created results in a change in the phase of the interference pattern at the detector. This change in phase is given by the following equation [70],

$$\Delta\phi = \frac{2\pi\Delta d}{\lambda} \tag{2-84}$$

where $\Delta\phi$ is the phase difference, Δd is the optical path difference between the beams and λ is the wavelength of the light. Tapered sensors discussed in Section 2.9.3 work on this principle and are often referred to as modal Mach-Zehnder interferometers.

2.10.3 Advantages of interferometers or interferometry

A single scan of the interferometer yields all the frequency components of the source illuminating the interferometer. Hence, several sensors differentiated by frequency can be multiplexed and interrogated in a single interferometric scan. This advantage of the interferometer is called as the multiplexablity advantage or the Fellgett advantage [71].

Unlike a tunable filter or a monochromator based system in which only a part of the illuminating light is used, in interferometry, all the illuminating light is used for measurements resulting in a higher optical throughput. This is called as the Jacquinot advantage or throughput advantage [72].

With an interferometer, frequency components can be accurately resolved. This enables the use of processing techniques like spectral addition, subtraction, etc. Also due to high accuracy, a laser source with high monochromaticity can be used for referencing the interferometric measurements. This advantage is called the high accuracy or Connes advantage [73].

In the context of the experiments discussed in this document, this paragraph throws light on how the advantages of the interferometer have been exploited.

Multiple FBG sensors with different peak values are interrogated based on the Fellgett advantage of the interferometer, as FBGs with different peak values can be interrogated in a single scan. Also, in the interrogation of the tapered sensors, the broadband spectrum of the sensor is resolved by exploiting the Fellgett advantage. The Jacquinot advantage of the interferometer results in an increased detectable energy from the FBGs and the tapered sensors. The use of an FBG sensor for referencing the measurements in the experiments is based on the Connes advantage.

2.10.4 Applications of interferometers

In general interferometers have been used for; distance measurements[74]–[76], refractive index measurements [77]–[79], wavelength monitoring [65], [80]–[84], Sagnac interferometers have high sensitivity to rotation and hence have been used for rotation detection [85], [86] and most recently, a large scale Michelson interferometer has been used for the detection of gravitational waves [87]. One major advantage of the interferometers is their flexibility. They can either be implemented in in an all-fibre setup or a bulk optic setup [88], [89].

The fibre optic systems pose numerous advantages over bulk optic systems. An important practical advantage of all-fibre setups is their robustness. All components are interconnected with each other, so there are fewer chances for misalignment. Sometimes, the fibres do get bent (within the limits of fibre's bend radius) or twisted but without detrimental effects. The various parts need not be rigidly connected and as the light is kept entirely within the fibre cores and closed optical components, there is no or less impact from external forces. The interferometric interrogation setups discussed in the experimental sections have been implemented in an all-fibre environment due to the aforementioned advantages.

2.10.5 Fourier Transform Spectroscopy

The Fourier transform of the coherence function yields the irradiating source's power spectral density, as discussed in Section 2.5.1. Fourier transform spectroscopy (FTS) is an application for obtaining temporal coherence measurements and as it is mainly used in the infra-red section of the spectrum, this technique is also often referred to as Fourier transform infrared spectroscopy (FTIR).

A reference beam sent into a Michelson interferometer with one moving mirror or a stretching fiber, produces an oscillating output whose frequency depends on the wavelength of light and rate of change of length of the arm of the interferometer. In order to sample this signal accurately, the Nyquist condition [90] requires us to sample the interferometric data at a rate greater than twice this frequency. The same condition holds when sampling a broadband interferogram as the main oscillation frequency is determined by the centre wavelength of the spectrum and the rate of change of length of arm of the interferometer.

In the experiments discussed in Chapters 3-6, to satisfy the Nyquist sampling criterion [90] or adequately sample the interferometric fringes, the interferometric signals are logged at the rates mentioned in the chapters. The DAQs used in the experimental Chapters 3-6 sequentially sample the channels and hence, there is an element of time division multiplexing involved. But due to the high sampling rates, the time delay between the channel samples is negligible.

The Michelson interferometer can be assumed to be a frequency transducer that converts optical frequencies to electrical frequencies. Any changes to the wavelength of the incident light can thus be studied by monitoring the frequency of the interferometric signal. Optical sensors such as the FBGs are interferometrically interrogated using the aforementioned property [62], [68]–[70]. The minimum resolvable wavelength of the interferometer is given by [85],

$$\Delta\lambda = n_a \frac{\lambda^2}{c\tau_\Delta} \tag{2-85}$$

where n_a is the group refractive index of air, c is the speed of light in vacuum, $\tau_\Delta$is the difference in path length. One of the main limitations of FTS as seen from Equation (2-85) is that higher measurement resolutions require larger scan lengths or path lengths. Previously, Davis and Kersey [88] using FTS have interrogated an FBG sensor array with a ~15pm resolution by using an OPD of 300mm. According to Equation (2-85), the minimum OPD scan to achieve this would be ~160mm. However, this limitation is due to the Fourier transform processing technique and can be overcome by employing Hilbert transform processing technique (HTT) for processing the interferometric signals [91]. Using HTT results similar to FTS have been obtained for much shorter OPD of ~1.2mm [92].

Conventionally with FTS, the sensor spectrum is obtained from the interferograms by the application of Fourier transform and the changes to sensor peak values are obtained from the sensor's spectrum logged at the different intervals. This method requires higher FTS resolution or larger OPD scans to clearly resolve the changing peak values. However, with HTT, the slopes of the reference and measurement sensors' instantaneous phase vectors are compared for obtaining the sensor measurements. As the slope of a line is constant at any given point along the line, HTT permits the use of shorter scans. The use of HTT has been described in the next section.

2.10.6 Hilbert transform processing technique

The fundamental need or application of the Hilbert transform processing technique is to obtain instantaneous phase vectors from the interferometric signals. The use of Hilbert transform processing technique in sensor interrogation is twofold.

First using HTT, the instantaneous phase vector of the reference interferogram is obtained for optical path delay (OPD) calibration. The OPD calibration is performed by sampling the reference instantaneous phase vector at equal intervals between its minimum and maximum values and this simulates uniform delay sampling. The interval value is obtained by subtracting the minimum value from the maximum and then dividing it by the length of the phase vector (number of samples in the phase vector). Thus, the interval value is not constant and varies depending on the OPD of the scan and the wavelength of the reference source. By the interpolation of the interferometric signals over the simulated delay intervals, the undesired spectral content is removed in the reference and measurement spectra.

Secondly, HTT is used for sensor measurements post delay calibration. Sensor measurements are obtained by comparing the instantaneous phase vectors of the reference and measurement sensors which are in turn obtained from the delay calibrated interferometric signals. The process of obtaining sensor measurements using HTT is described in the following paragraphs.

Hilbert transform of an interferogram yields its analytic signal, which is a generalisation of the phasor. The efficacy of Hilbert transform processing in demodulating FBGs has been previously demonstrated by Rochford and Dyer [91]. Applying FFT to a continuous time series interferogram S_i yields both positive and non-positive frequencies. The complex data set H_i is obtained by setting all non-positive frequencies of the FFT data to zero and thereafter taking an inverse Fourier transform of the FFT data with only the positive frequencies. The analytic data H_i thus obtained is given by the following expression [91],

$$H_i = A_i e^{j\phi_i} \tag{2-86}$$

where i is the uniformly sampled data point and ϕ_i is the instantaneous phase at i. The analytic data has two parts, a real part, and an imaginary part. While the real part is the original sinusoidal signal picked up by the detector minus the negative frequencies, the imaginary component is the 90^0 phase shifted version of the real component. Figure 2-20 shows the plot of the analytic signal of a section of an interferogram.

At each data point i the instantaneous phase ϕ_i can be obtained using the following equation [85].

$$\phi_i = \tan^{-1}\frac{Im(H_i)}{Re(H_i)} \tag{2-87}$$

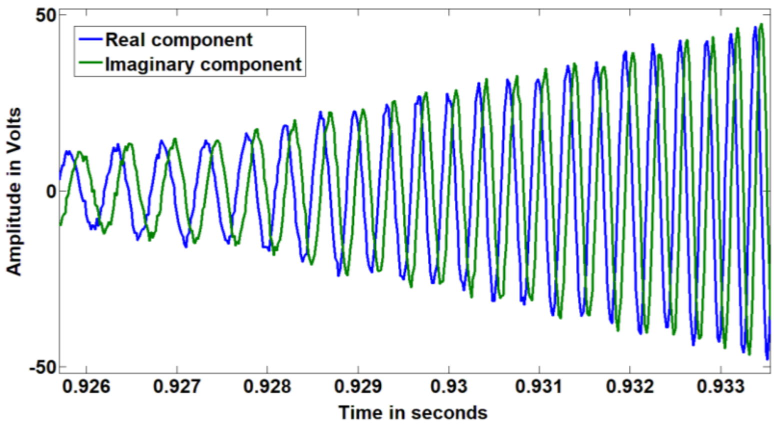

Figure 2-20: Plot of analytic signal sample

From Equation (2-87), the frequency can be determined by using [85],

$$\omega_i = \frac{d\phi_i}{dt} \tag{2-88}$$

As ω=2πc/λ, the above equations can be represented in terms of wavelength. If the time series interferogram S_i contains interferograms from multiple light beams, then individual wavelengths can be obtained by windowing specific frequency components in the FFT of S_i data. The measurement wavelength can be obtained from the ratio of optical frequencies of the measurement and reference wavelengths as shown in the equation below.

$$\frac{\lambda_M}{\lambda_R} = \frac{\omega_R}{\omega_M} = \frac{d\phi_R}{d\phi_M} \tag{2-89}$$

In the above Equation (2-89), subscript M and R denote measurement and reference components respectively. As seen from the equation above, measurements using HTT involves a comparison of the temporal phase vectors of the reference and the measurement wavelengths.

2.11 Review of fibre optic sensor interrogation methods

Notwithstanding the above mentioned interferometric interrogation of sensors and the HTT of processing sensor's interferometric signals, to-date, a number of different approaches have been taken for interrogating different optical sensors. As the scope of this study involves only the FBG and tapered optical fibre sensor, only the interrogation schemes used for interrogating these two sensor types have been reviewed in the sections below.

2.11.1 FBG interrogation schemes

Interrogation of individual FBG sensors has been demonstrated using a wavelength division coupler with ± 3µstrain resolution [65] and using a matched-filter with a high resolution of 0.01µstrain [93]. Using tunable filters multiple FBGs have been interrogated with microstrain resolutions [62], [63], [94], [95], [96], [97]. If not all, most of the interrogators based on a tunable filter use a Fabry-Perot (FP) filter. In the demonstration of multiple FBG interrogation [63], Kersey and Berkoff have used an FP filter of .38nm bandwidth for a source bandwidth of 36nm. The filter's bandwidth is a fraction of the scanned width resulting in a drop in the optical throughput. This drop in the optical throughput of scanned filter based systems can be avoided with the use of optical interferometry [16].

Numerous schemes for FBG array demodulation using, tunable laser diode [64], bulk optic [89], and static interferometry [83] have been implemented in the past. FBGs have also been interrogated with sub pico-meter resolution using arrayed waveguides (AWG) [65]–[67], but the number of sensors that can be interrogated using AWG is constrained by the number of channels and FBG separation bandwidth. Fourier transform spectroscopy (FTS) offers the Fellgett advantage for multiplexing multiple FBG sensors. A resolution of ~15pm for 300mm OPD has been reported by Davis and Kersey [88] using FTS. When interferograms are processed using FTS, the resolution of the system is a function of OPD and for high resolution interrogation, OPD needs to be accordingly high.

However, using Hilbert Transform processing Technique (HTT) resolutions comparable to that obtained using FTS have been reported for much shorter OPD of 1.2mm[92]. HTT involves a comparison of temporal phase vectors of the reference beam and the measurand beam thus cutting the need for complex delay processing circuits. Using an all-fibre Michelson interferometer and HTT, an accuracy of ±0.5pm for ~6mm delay scans has been reported by O'Mahoney *et al*. while interrogating an array of FBGs [98]. In the above mentioned all-fibre setup, the FBG array is illuminated using a broadband source and the reflections from FBGs are used to generate a superposition of multiple narrow bandwidth interferograms. As a result, FBGs of similar wavelengths cannot be interrogated and the number of FBGs that can be interrogated is limited by the spectral bandwidth of the source, spectral spacing between the FBGs and their individual bandwidths.

Recently, high-resolution measurements of arrays of FBGs using time division multiplexing (TDM) have been reported [99], [100]. In a TDM based system, a pulsed light source is used to illuminate the FBGs and the wavelength of reflected pulses are processed as a function of a time delay between the arrival of source pulses at the FBG and the arrival of pulses reflected by the FBG at the detector. TDM technique does not allow simultaneous measurement of all the FBGs across multiple arrays in a single scan. A TDM based system requires pulsed light and complex time-gated detectors are needed. Moreover in a TDM based system, due to the time-bandwidth factor, pulses of short duration give rise to wider spectral bandwidth, which in turn results in low reflected power from narrowband gratings and consequently, low signal-to-noise ratio (SNR).

Another interferometric technique alternative to TDM is the Frequency Shifted Interferometry (FSI). The interferometer used in FSI is a Mach-Zehnder interferometer with an acoustic-opto modulator (AOM) in one of the arms. By sweeping AOM through a set frequency range and tunable laser source (TLS) through a set wavelength bandwidth, two dimensional FFT spectra are obtained. The reflectivity of FBGs is encoded in the amplitude of FFT spectra and their location in the phase of FFT spectra [101].

Using FSI 65 closely spaced weak FBGs have been interrogated [102] and recently, a potential for interrogating thousands of sensors at high resolution has been reported using a combination of WDM and the abovementioned FSI. Though FSI allows for simultaneous interrogation of multiple arrays of multiple sensors that the other techniques have failed to achieve, FSI relies on the use of FBGs with low reflectivity and the low reflectivity is known to limit the sensor bandwidth [103]. The light propagating to the downstream sensor passes through a number of upstream sensors. As a result, the input light to the downstream sensor will possess characteristics of the upstream sensors called shadows. In FSI where the sensors' wavelengths are similar, the effect of shadowing is more pronounced resulting in crosstalk. Also, FSI is susceptible to crosstalk between sensors due to the side lobes generated by the FFT process and due to the interference from counter-propagating beams.

2.11.2 Tapered sensor interrogation schemes

Interferometric tapered sensors have been primarily used for refractive index based sensing of various solutions, liquids, and bio-molecules [51], [104], [105]. They have also been used for measuring, temperature [106]–[108], strain [106], [109], curvature [110], liquid level [111], chemicals such as ammonia, hydrogen and ethanol [69], [112], [113]. For most if not all of the above-mentioned measurements, an optical spectrum analyser (OSA) was used for measuring the change in phase of the sensor's spectrum or a change to the sensor's peak wavelength, but certain studies have used a spectrometer or a component test system in place of an OSA for measuring the sensor's spectral response [52], [69], [112]. For measurements involving changes to the intensity of sensor's spectra an optical power meter or a combination of a photodiode and an oscilloscope have been used in the past [108], [114], [115].

From Section 2.9.2 it can be seen that the FBGs are typically operated in the reflection mode and the reflection spectrum of FBGs have a very narrow linewidth when compared to the illuminating superluminescent diode light source. As a result of the narrow linewidth, several FBGs can be cascaded and hence, FBG interrogation schemes are influenced by factors such as the number of FBG arrays and sensor density in an array, etc. Unlike FBGs, tapered sensors take up the entire bandwidth of the illuminating light source and as a result, multiple sensors cannot be cascaded. Thus, for tapered sensor interrogation, systems less complex than the ones used for FBG interrogation are used.

2.12 Summary

Ever since the FBG sensing was first demonstrated [38], FBG sensors have been gradually gaining prominence for use in sensing applications mainly due to the ease of multiplexablity and their fundamental principle of working. FBG and other grating based sensors are extremely sensitive to a number of physical parameters like strain, temperature, pressure, etc., but require special treatment (known as labelling) for sensing parameters like gas concentration, refractive index, etc., [116]–[120]. Special treatments to FBG sensors change their inherent sensitivity to primary parameters like temperature and strain, thus limiting provisions for cross-sensitivity compensation.

Thus, for label-free refractive index measurements, i.e., refractive index measurements without markers or specialized coatings, a second type of fibre optic sensor called the tapered sensor is used. A tapered sensor works on the principles of evanescent wave sensing and is inherently sensitive to refractive index changes without special treatments. In a day-to-day scenario, an efficient sensing system should quantify or estimate multiple parameters. For example, in a civil structure, a number of parameters like carbonation in concrete, temperature, structural fatigue, etc. need to be studied for effective structural health monitoring. Thus, multi-parameter sensing calls for the use of varied sensor types for monitoring different parameters.

Existing FBG interrogation systems reviewed in Section 2.12, are capable of interrogating at the most an array of sensors without forgoing optical throughput and sensor bandwidth, in a single scan. Interferometry typically implemented as FTS permits multiple arrays of FBG sensor interrogation with sub-picometer resolutions. But high-resolution measurements using FTS requires long scan lengths which lead to non-uniform delay sampling and, key measurement events tend to get missed when using long scan lengths. However, measurement resolutions similar to FTS have been previously obtained for a much shorter scan lengths using HTT. The efficacy of demodulating FBGs using HTT has been previously demonstrated by Rochford and Dyer [91], Flavin *et al.* [92] and O'Mahoney *et al.* [98]. The approach demonstrated in [91], [92], [98] has been adopted in this study for interrogation of sensors using an all-fibre Michelson interferometer with a short scan length described in the experimental chapters.

In the conventional interferometric FBG interrogation setup, the FBG is first illuminated using a broadband light source and the light reflected by the FBG is fed into the interferometer which then yields a high coherence interferogram. The resulting high coherence interferogram is then processed for measurement results. In the conventional setup, FBGs with similar wavelengths cannot be interrogated and as a result, the sensor density is limited by the bandwidth of the optical source and bandwidth of separation between the multiplexed sensors.

The limitation of the conventional interferometric setups can be overcome by the reversal of the order of illumination of the sensors and the interferometer.

Illuminating the interferometer first results in the generation of a low coherence interferogram and when an FBG sensor is illuminated with this low coherence interferogram, it results in the reflection of an interferogram with a coherence length greater than that of the source. The reflected higher coherence interferograms are then processed for measurement results. Using this process of filtering high coherence interferogram from a low coherence interferogram, FBGs with similar wavelengths can be simultaneously interrogated and by coherence filtering tapered sensors can also be interrogated in addition to the FBGs.

To-date, numerous studies have been carried out using a combination of fibre Bragg grating sensors and interferometric sensors [116], [120]–[132]. In the works [116], [120]–[131], an OSA was used for interrogating the sensor combination and in [132], a commercial FBG interrogator (SM125, Micron Optics) was used. Both the equipment (OSA and SM125) costs several tens of thousands of euros which increases the cost of interrogation per sensor. The work reported in this document investigates the feasibility of using one portable interferometric interrogation setup to interrogate multiple fibre optic sensor classes, with an aim to effectively reduce the overall cost of interrogation per fibre optic sensor. Efficacy of the described interrogation scheme is studied by interrogating: multiple arrays of multiple FBGs simultaneously, one or more tapered sensors, and a combination of FBGs and a tapered sensor.

In the following chapter, the interrogation of multiple arrays of wavelength division multiplexed FBG sensors by interferometric illumination is presented. The experiment described will demonstrate the capability of the interferometric illumination interrogation scheme to simultaneously interrogate multiple FBG sensors within a single array and multiple FBG sensors with similar wavelengths across multiple arrays.

2.13 References

[1] R. Kashyap, *Fiber Bragg gratings*. Burlington, MA: Academic Press, 2010.

[2] E. Hecht, *Optics*, 4th ed. Reading, Mass: Addison-Wesley, 2002.

[3] F. L. Pedrotti, L. M. Pedrotti, and L. S. Pedrotti, *Introduction to optics*, 3rd ed. Upper Saddle River, N.J: Pearson/Prentice Hall, 2007.

[4] E. P. Goodwin and J. C. Wyant, *Field Guide to Interferometric Optical Testing*. 1000 20th Street, Bellingham, WA 98227-0010 USA: SPIE, 2006.

[5] S. G. Lipson, H. Lipson, and D. S. Tannhauser, *Optical physics*, 3rd ed. Cambridge ; New York, NY, USA: Cambridge University Press, 1995.

[6] G. P. Agrawal, *Fiber-optic communication systems*. New York: Wiley-Interscience, 2002.

[7] D. G. O'Keeffe, 'Development of fibre optic evanescent-wave fluorescent-based sensors', PhD Thesis, Dublin City University, 1995.

[8] D. Gloge, 'Weakly Guiding Fibers', *Appl. Opt.*, vol. 10, no. 10, p. 2252, Oct. 1971, doi: 10.1364/AO.10.002252.

[9] A. W. Snyder and W. R. Young, 'Modes of optical waveguides', *J. Opt. Soc. Am.*, vol. 68, no. 3, p. 297, Mar. 1978, doi: 10.1364/JOSA.68.000297.

[10] J. A. Buck, *Fundamentals of optical fibers*, 2nd ed. Hoboken, N.J: John Wiley & Sons, 2004.

[11] B. E. A. Saleh, *Fundamentals of photonics*. 2019.

[12] A. Ghatak and K. Thyagarajan, *Introduction to fiber optics*. Cambridge: Cambridge University Press, 1998.

[13] K. Okamoto, *Fundamentals of optical waveguides*, 2nd ed. Amsterdam ; Boston: Elsevier, 2006.

[14] T. Miya, Y. Terunuma, T. Hosaka, and T. Miyashita, 'Ultimate low-loss single-mode fibre at 1.55 μm', *Electron. Lett.*, vol. 15, no. 4, p. 106, 1979, doi: 10.1049/el:19790077.

[15] M. Born *et al.*, *Principles of Optics: Electromagnetic Theory of Propagation, Interference and Diffraction of Light*, 7th ed. Cambridge: Cambridge University Press, 1999.

[16] J. Dakin and B. Culshaw, *Optical fiber sensors: Principles and components. Volume 1*, vol. 1. 1988.

[17] R. Hui and M. S. O'Sullivan, *Fiber optic measurement techniques*. Amsterdam; London: Elsevier/Academic Press, 2009.

[18] R. Di Sante, 'Fibre Optic Sensors for Structural Health Monitoring of Aircraft Composite Structures: Recent Advances and Applications', *Sensors*, vol. 15, no. 8, pp. 18666–18713, Jul. 2015, doi: 10.3390/s150818666.

[19] B. H. Lee *et al.*, 'Interferometric Fiber Optic Sensors', *Sensors*, vol. 12, no. 12, pp. 2467–2486, Feb. 2012, doi: 10.3390/s120302467.

[20] P. Hariharan, *Basics of interferometry*, 2nd ed. Amsterdam ; Boston: Elsevier Academic Press, 2007.

[21] R. Kashyap, 'Photosensitive Optical Fibers: Devices and Applications', *Optical Fiber Technology*, vol. 1, no. 1, pp. 17–34, Oct. 1994, doi: 10.1006/ofte.1994.1003.

[22] K. T. V. Grattan and B. T. Meggitt, Eds., *Optical Fiber Sensor Technology*. Boston, MA: Springer US, 2000.

[23] J. R. Pierce, ‘Coupling of Modes of Propagation’, *Journal of Applied Physics*, vol. 25, no. 2, pp. 179–183, Feb. 1954, doi: 10.1063/1.1721599.

[24] D. Marcuse, ‘The Coupling of Degenerate Modes in Two Parallel Dielectric Waveguides’, *Bell System Technical Journal*, vol. 50, no. 6, pp. 1791–1816, Jul. 1971, doi: 10.1002/j.1538-7305.1971.tb02582.x.

[25] D. Marcuse, ‘Coupled Mode Theory of Round Optical Fibers’, *Bell System Technical Journal*, vol. 52, no. 6, pp. 817–842, Jul. 1973, doi: 10.1002/j.1538-7305.1973.tb01992.x.

[26] A. W. Snyder, ‘Coupled-Mode Theory for Optical Fibers’, *Journal of the Optical Society of America*, vol. 62, no. 11, p. 1267, Nov. 1972, doi: 10.1364/JOSA.62.001267.

[27] A. W. Snyder, ‘Coupling of Modes on a Tapered Dielectric Cylinder’, *IEEE Transactions on Microwave Theory and Techniques*, vol. 18, no. 7, pp. 383–392, Jul. 1970, doi: 10.1109/TMTT.1970.1127247.

[28] A. Yariv, ‘Coupled-mode theory for guided-wave optics’, *IEEE Journal of Quantum Electronics*, vol. 9, no. 9, pp. 919–933, Sep. 1973, doi: 10.1109/JQE.1973.1077767.

[29] H. F. Taylor and A. Yariv, ‘Guided wave optics’, *Proceedings of the IEEE*, vol. 62, no. 8, pp. 1044–1060, 1974, doi: 10.1109/PROC.1974.9569.

[30] H. Kogelnik, ‘Coupled Wave Theory for Thick Hologram Gratings’, *Bell System Technical Journal*, vol. 48, no. 9, pp. 2909–2947, Nov. 1969, doi: 10.1002/j.1538-7305.1969.tb01198.x.

[31] H. Kogelnik, ‘2. Theory of dielectric waveguides’, in *Integrated Optics*, Berlin, Heidelberg: Springer Berlin Heidelberg, 1975, pp. 13–81.

[32] R. V. Schmidt, D. C. Flanders, C. V. Shank, and R. D. Standley, ‘Narrow-band grating filters for thin-film optical waveguides’, *Applied Physics Letters*, vol. 25, no. 11, pp. 651–652, Dec. 1974, doi: 10.1063/1.1655346.

[33] T. Koch, E. Burkhardt, F. Storz, T. Bridges, and T. Sizer, ‘Vertically grating-coupled ARROW structures for III--V integrated optics’, *IEEE Journal of Quantum Electronics*, vol. 23, no. 6, pp. 889–897, Jun. 1987, doi: 10.1109/JQE.1987.1073443.

[34] C. Cremer, G. Heise, R. Marz, M. Schienle, G. Schulte-Roth, and H. Unzeitig, ‘Bragg gratings on InGaAsP/InP waveguides as polarization independent optical filters’, *Journal of Lightwave Technology*, vol. 7, no. 11, pp. 1641–1645, Nov. 1989, doi: 10.1109/50.45883.

[35] R. R. A. Syms, ‘Optical directional coupler with a grating overlay’, *Applied Optics*, vol. 24, no. 5, p. 717, Mar. 1985, doi: 10.1364/AO.24.000717.

[36] T. Erdogan, ‘Fiber grating spectra’, *Journal of Lightwave Technology*, vol. 15, no. 8, pp. 1277–1294, Aug. 1997, doi: 10.1109/50.618322.

[37] W. J. Bock, I. Gannot, and S. Tanev, Eds., *Optical waveguide sensing and imaging*. Dordrecht: Springer, 2008.

[38] W. W. Morey, G. Meltz, and W. H. Glenn, ‘Fiber Optic Bragg Grating Sensors’, Feb. 1990, p. 98, doi: 10.1117/12.963022.

[39] A. Othonos and K. Kalli, *Fiber Bragg gratings: fundamentals and applications in telecommunications and sensing*. Boston, Mass: Artech House, 1999.

[40] M. M., R. C. S. B. Allil, B. A., and F. V. B. de Nazar, ‘A Guide to Fiber Bragg Grating Sensors’, in *Current Trends in Short- and Long-period Fiber Gratings*, C. Cuadrado-Laborde, Ed. InTech, 2013.

[41] K. O. Hill, Y. Fujii, D. C. Johnson, and B. S. Kawasaki, ‘Photosensitivity in optical fiber waveguides: Application to reflection filter fabrication’, *Applied Physics Letters*, vol. 32, no. 10, pp. 647–649, May 1978, doi: 10.1063/1.89881.

[42] K. O. Hill, B. Malo, F. Bilodeau, and D. C. Johnson, ‘Photosensitivity in Optical Fibers’, *Annu. Rev. Mater. Sci.*, vol. 23, no. 1, pp. 125–157, Aug. 1993, doi: 10.1146/annurev.ms.23.080193.001013.

[43] J. Lapierre, J. Bures, and G. Chevalier, ‘Fiber-optic integrated interference filters’, *Opt. Lett.*, vol. 7, no. 1, p. 37, Jan. 1982, doi: 10.1364/OL.7.000037.

[44] G. Meltz, W. W. Morey, and W. H. Glenn, ‘Formation of Bragg gratings in optical fibers by a transverse holographic method’, *Opt. Lett.*, vol. 14, no. 15, p. 823, Aug. 1989, doi: 10.1364/OL.14.000823.

[45] B.-O. Guan, Y. Ran, F.-R. Feng, and L. Jin, ‘Formation and Applications of the Secondary Fiber Bragg Grating’, *Sensors*, vol. 17, no. 2, p. 398, Feb. 2017, doi: 10.3390/s17020398.

[46] J.-L. Archambault, L. Reekie, and P. J. Russell, ‘High reflectivity and narrow bandwidth fibre gratings written by single excimer pulse’, *Electronics Letters*, vol. 29, no. 1, pp. 28–29, Jan. 1993, doi: 10.1049/el:19930018.

[47] S. W. Harun, K. S. Lim, C. K. Tio, K. Dimyati, and H. Ahmad, ‘Theoretical analysis and fabrication of tapered fiber’, *Optik - International Journal for*

Light and Electron Optics, vol. 124, no. 6, pp. 538–543, Mar. 2013, doi: 10.1016/j.ijleo.2011.12.054.

[48] S. M. John, 'Evanescent wave fibre optic sensors: design, fabrication and characterization', Cochin University of Science and Technology, 2000.

[49] V. Ruddy, 'An effective attenuation coefficient for evanescent wave spectroscopy using multimode fiber', *Fiber and Integrated Optics*, vol. 9, no. 2, pp. 143–151, Apr. 1990, doi: 10.1080/01468039008202901.

[50] G. Stewart and B. Culshaw, 'Optical waveguide modelling and design for evanescent field chemical sensors', *Optical and Quantum Electronics*, vol. 26, no. 3, pp. S249–S259, Mar. 1994, doi: 10.1007/BF00384677.

[51] J. Miller *et al.*, 'Biconically Tapered Fiber Optic Probes for Rapid Label-Free Immunoassays', *Biosensors*, vol. 5, no. 2, pp. 158–171, Apr. 2015, doi: 10.3390/bios5020158.

[52] Y. Tian, W. Wang, N. Wu, X. Zou, and X. Wang, 'Tapered Optical Fiber Sensor for Label-Free Detection of Biomolecules', *Sensors*, vol. 11, no. 12, pp. 3780–3790, Mar. 2011, doi: 10.3390/s110403780.

[53] Y. L. Hoo, W. Jin, H. L. Ho, D. N. Wang, and R. S. Windele, 'Evanescent wave gas sensing using microstructure fibre', 2001, pp. 8–9, doi: 10.1109/CLEOPR.2001.968008.

[54] C. Consani, C. Ranacher, A. Tortschanoff, T. Grille, P. Irsigler, and B. Jakoby, 'Evanescent-Wave Gas Sensing Using an Integrated Thermal Light Source', *Proceedings*, vol. 1, no. 4, p. 550, Aug. 2017, doi: 10.3390/proceedings1040550.

[55] H. Tai, T. Yoshino, and H. Tanaka, 'Fiber-optic evanescent-wave methane-gas sensor using optical absorption for the 3392-μm line of a He–Ne laser', *Optics Letters*, vol. 12, no. 6, p. 437, Jun. 1987, doi: 10.1364/OL.12.000437.

[56] R. Siebert and J. Müller, 'Infrared integrated optical evanescent field sensor for gas analysis', *Sensors and Actuators A: Physical*, vol. 119, no. 1, pp. 138–149, Mar. 2005, doi: 10.1016/j.sna.2004.11.001.

[57] G. Stewart, F. A. Muhammad, and B. Culshaw, 'Sensitivity improvement for evanescent-wave gas sensors', *Sensors and Actuators B: Chemical*, vol. 11, no. 1–3, pp. 521–524, Mar. 1993, doi: 10.1016/0925-4005(93)85297-N.

[58] S. Sekimoto *et al.*, 'A fiber-optic evanescent-wave hydrogen gas sensor using palladium-supported tungsten oxide', *Sensors and Actuators B: Chemical*, vol. 66, no. 1–3, pp. 142–145, Jul. 2000, doi: 10.1016/S0925-4005(00)00330-0.

[59] M. Morisawa, Y. Amemiya, H. Kohzu, C. X. Liang, and S. Muto, 'Plastic optical fibre sensor for detecting vapour phase alcohol', *Measurement Science and Technology*, vol. 12, no. 7, pp. 877–881, Jun. 2001, doi: 10.1088/0957-0233/12/7/322.

[60] D. Liu *et al.*, 'High sensitivity optical fiber sensors for simultaneous measurement of methanol and ethanol', *Sensors and Actuators B: Chemical*, vol. 271, pp. 1–8, Oct. 2018, doi: 10.1016/j.snb.2018.05.106.

[61] A. D. Kersey and M. A. Davis, 'All-fibre Bragg grating strain-sensor demodulation technique using a wavelength division coupler', *Electronics Letters*, vol. 30, no. 1, pp. 75–77, Jan. 1994, doi: 10.1049/el:19940059.

[62] M. A. Davis, D. G. Bellemore, M. A. Putnam, and A. D. Kersey, 'Interrogation of 60 fibre Bragg grating sensors with microstrain resolution capability', *Electronics Letters*, vol. 32, no. 15, p. 1393, 1996, doi: 10.1049/el:19960908.

[63] A. D. Kersey, T. A. Berkoff, and W. W. Morey, 'Multiplexed fiber Bragg grating strain-sensor system with a fiber Fabry–Perot wavelength filter', *Optics Letters*, vol. 18, no. 16, p. 1370, Aug. 1993, doi: 10.1364/OL.18.001370.

[64] M. S. Muller *et al.*, 'Fiber-Optic Sensor Interrogation Based on a Widely Tunable Monolithic Laser Diode', *IEEE Transactions on Instrumentation and Measurement*, vol. 59, no. 3, pp. 696–703, Mar. 2010, doi: 10.1109/TIM.2009.2025987.

[65] M. Perry, P. Orr, P. Niewczas, and M. Johnston, 'High-Speed Interferometric FBG Interrogator With Dynamic and Absolute Wavelength Measurement Capability', *Journal of Lightwave Technology*, vol. 31, no. 17, pp. 2897–2903, Sep. 2013, doi: 10.1109/JLT.2013.2276391.

[66] Y. Marin, T. Nannipieri, C. Oton, and F. Di Pasquale, 'Integrated FBG Sensors Interrogation using Active Phase Demodulation on a Silicon Photonic Platform', *Journal of Lightwave Technology*, pp. 1–1, 2016, doi: 10.1109/JLT.2016.2598395.

[67] D. Pustakhod, E. Kleijn, K. Williams, and X. Leijtens, 'High-Resolution AWG-Based Fiber Bragg Grating Interrogator', *IEEE Photonics Technology Letters*, vol. 28, no. 20, pp. 2203–2206, Oct. 2016, doi: 10.1109/LPT.2016.2587812.

[68] K. Q. Kieu and M. Mansuripur, 'Biconical Fiber Taper Sensors', *IEEE Photonics Technology Letters*, vol. 18, no. 21, pp. 2239–2241, Nov. 2006, doi: 10.1109/LPT.2006.884742.

[69] S. H. Girei, A. A. Shabaneh, P. T. Arasu, S. Painam, and M. H. Yaacob, 'Tapered multimode fiber sensor for ethanol sensing application', in *2013 IEEE 4th International Conference on Photonics (ICP)*, Melaka, Malaysia, Oct. 2013, pp. 275–277, doi: 10.1109/ICP.2013.6687137.

[70] W. H. Steel, *Interferometry*, 2nd ed., 1st paperback ed. Cambridge [Cambridgeshire] ; New York: Cambridge University Press, 1986.

[71] P. Fellgett, 'Spectromètre interférentiel multiplex pour mesures infra-rouges sur les étoiles', *Journal de Physique et le Radium*, vol. 19, no. 3, pp. 237–240, 1958, doi: 10.1051/jphysrad:01958001903023700.

[72] P. Jacquinot, 'New developments in interference spectroscopy', *Reports on Progress in Physics*, vol. 23, no. 1, p. 267, 1960.

[73] J. Connes and P. Connes, 'Near-Infrared Planetary Spectra by Fourier Spectroscopy. I. Instruments and Results', *J. Opt. Soc. Am.*, vol. 56, no. 7, pp. 896–910, Jul. 1966, doi: 10.1364/JOSA.56.000896.

[74] D. Xiaoli and S. Katuo, 'High-accuracy absolute distance measurement by means of wavelength scanning heterodyne interferometry', *Measurement Science and Technology*, vol. 9, no. 7, pp. 1031–1035, Jul. 1998, doi: 10.1088/0957-0233/9/7/004.

[75] F. Gouaux, N. Servagent, and T. Bosch, 'Absolute distance measurement with an optical feedback interferometer', *Applied Optics*, vol. 37, no. 28, p. 6684, Oct. 1998, doi: 10.1364/AO.37.006684.

[76] J. Thiel, T. Pfeifer, and M. Hartmann, ‘Interferometric measurement of absolute distances of up to 40 m’, *Measurement*, vol. 16, no. 1, pp. 1–6, Sep. 1995, doi: 10.1016/0263-2241(95)00010-I.

[77] M. Ohmi, T. Shiraishi, H. Tajiri, and M. Haruna, ‘Simultaneous Measurement of Refractive Index and Thickness of Transparent Plates by Low Coherence Interferometry’, *Optical Review*, vol. 4, no. 4, pp. 507–515, Jul. 1997, doi: 10.1007/s10043-997-0507-1.

[78] Z. Bor, K. Osvay, B. Rácz, and G. Szabó, ‘Group refractive index measurement by Michelson interferometer’, *Optics Communications*, vol. 78, no. 2, pp. 109–112, Aug. 1990, doi: 10.1016/0030-4018(90)90104-2.

[79] D. Iyer, ‘A Michelson interferometric technique for measuring refractive index of sodium zinc tellurite glasses’, Lehigh University.

[80] A. D. Kersey, W. W. Morey, and T. A. Berkoff, ‘Fiber-optic Bragg grating strain sensor with drift-compensated high-resolution interferometric wavelength-shift detection’, *Optics Letters*, vol. 18, no. 1, p. 72, Jan. 1993, doi: 10.1364/OL.18.000072.

[81] K. P. Koo and A. D. Kersey, ‘Bragg grating-based laser sensors systems with interferometric interrogation and wavelength division multiplexing’, *Journal of Lightwave Technology*, vol. 13, no. 7, pp. 1243–1249, Jul. 1995, doi: 10.1109/50.400692.

[82] T. A. Berkoff and A. D. Kersey, ‘Fiber Bragg grating array sensor system using a bandpass wavelength division multiplexer and interferometric detection’, *IEEE Photonics Technology Letters*, vol. 8, no. 11, pp. 1522–1524, Nov. 1996, doi: 10.1109/68.541570.

[83] D. F. Murphy, D. A. Flavin, R. McBride, and J. D. C. Jones, ‘Interferometric Interrogation of In-Fiber Bragg Grating Sensors Without Mechanical Path Length Scanning’, *J. Lightwave Technol.*, vol. 19, no. 7, p. 1004, Jul. 2001.

[84] W. Gornall and T. R. Amarel, ‘Accurate wavelength interrogation of fiber Bragg grating sensors using Michelson interferometry’, Mar. 2004, p. 56, doi: 10.1117/12.519110.

[85] B. Culshaw and I. Giles, ‘Frequency modulated heterodyne optical fiber Sagnac interferometer’, *IEEE Journal of Quantum Electronics*, vol. 18, no. 4, pp. 690–693, Apr. 1982, doi: 10.1109/JQE.1982.1071570.

[86] T. L. Gustavson, P. Bouyer, and M. A. Kasevich, ‘Precision Rotation Measurements with an Atom Interferometer Gyroscope’, *Physical Review Letters*, vol. 78, no. 11, pp. 2046–2049, Mar. 1997, doi: 10.1103/PhysRevLett.78.2046.

[87] B. P. Abbott *et al.*, ‘Observation of Gravitational Waves from a Binary Black Hole Merger’, *Physical Review Letters*, vol. 116, no. 6, Feb. 2016, doi: 10.1103/PhysRevLett.116.061102.

[88] M. A. Davis and A. D. Kersey, ‘Application of a fiber Fourier transform spectrometer to the detection of wavelength-encoded signals from Bragg grating sensors’, *Journal of Lightwave Technology*, vol. 13, no. 7, pp. 1289–1295, Jul. 1995, doi: 10.1109/50.400685.

[89] Y. J. Rao, D. J. Webb, D. A. Jackson, L. Zhang, and I. Bennion, ‘High-resolution, wavelength-division-multiplexed in-fibre Bragg grating sensor system’, *Electronics Letters*, vol. 32, no. 10, p. 924, 1996, doi: 10.1049/el:19960589.

[90] H. Nyquist, ‘Certain Topics in Telegraph Transmission Theory’, *Trans. Am. Inst. Electr. Eng.*, vol. 47, no. 2, pp. 617–644, Apr. 1928, doi: 10.1109/T-AIEE.1928.5055024.

[91] K. B. Rochford and S. D. Dyer, ‘Demultiplexing of interferometrically interrogated fiber Bragg grating sensors using Hilbert transform processing’, *Journal of Lightwave Technology*, vol. 17, no. 5, pp. 831–836, May 1999, doi: 10.1109/50.762900.

[92] D. A. Flavin, R. McBride, and J. D. C. Jones, ‘Short-scan interferometric interrogation and multiplexing of fibre Bragg grating sensors’, *Optics Communications*, vol. 170, no. 4–6, pp. 347–353, Nov. 1999, doi: 10.1016/S0030-4018(99)00515-5.

[93] M. A. Davis and A. D. Kersey, ‘Matched-filter interrogation technique for fibre Bragg grating arrays’, *Electronics Letters*, vol. 31, no. 10, pp. 822–823, May 1995, doi: 10.1049/el:19950547.

[94] T. Yamaguchi and Y. Shinoda, ‘Multichannel High-Speed Fiber Bragg Grating Interrogation System Utilizing a Field Programmable Gate Array’, *IEEE Sens. Lett.*, vol. 2, no. 1, pp. 1–4, Mar. 2018, doi: 10.1109/LSENS.2017.2782670.

[95] I. Drazic-Segrt, A. Krnjak, M. Sprem, M. Bosiljevac, and Z. Sipus, ‘Portable FBG based optical sensor array’, Apr. 2015, pp. 1–5, doi: 10.1109/SAS.2015.7133657.

[96] P. Tsai, F. Sun, G. Xiao, Z. Zhang, S. Rahimi, and D. Ban, ‘A New Fiber-Bragg-Grating Sensor Interrogation System Deploying Free-Spectral-Range-Matching Scheme With High Precision and Fast Detection Rate’, *IEEE*

Photon. Technol. Lett., vol. 20, no. 4, pp. 300–302, Feb. 2008, doi: 10.1109/LPT.2007.915638.

[97] Y.-L. Lo, T.-H. Tsai, and P.-F. Shih, ‘Fiber sensing scanner system based on A-thermal fiber bragg gratings’, *Sensors and Actuators A: Physical*, vol. 242, pp. 32–42, May 2016, doi: 10.1016/j.sna.2016.02.027.

[98] K. T. O’Mahoney, R. P. O’Byrne, S. V. Sergeyev, Lin Zhang, and I. Bennion, ‘Short-Scan Fiber Interferometer for High-Resolution Bragg Grating Array Interrogation’, *IEEE Sensors Journal*, vol. 9, no. 10, pp. 1277–1281, Oct. 2009, doi: 10.1109/JSEN.2009.2029818.

[99] M. Njegovec and D. Donlagic, ‘Interrogation of FBGs and FBGs Arrays Using Standard Telecom DFB Diode’, *Journal of Lightwave Technology*, vol. 34, no. 22, pp. 5340–5348, Nov. 2016, doi: 10.1109/JLT.2016.2616725.

[100] J. Chen, Q. Liu, X. Fan, and Z. He, ‘Sub-Nano-Strain Multiplexed Fiber Optic Sensor Array for Quasi-Static Strain Measurement’, *IEEE Photonics Technology Letters*, vol. 28, no. 21, pp. 2311–2314, Nov. 2016, doi: 10.1109/LPT.2016.2592506.

[101] F. Ye, L. Qian, Y. Liu, and B. Qi, ‘Using Frequency-Shifted Interferometry for Multiplexing a Fiber Bragg Grating Array’, *IEEE Photonics Technology Letters*, vol. 20, no. 17, pp. 1488–1490, Sep. 2008, doi: 10.1109/LPT.2008.927898.

[102] Y. Ou *et al.*, ‘Large WDM FBG Sensor Network Based on Frequency-Shifted Interferometry’, *IEEE Photonics Technology Letters*, vol. 29, no. 6, pp. 535–538, Mar. 2017, doi: 10.1109/LPT.2017.2663665.

[103] M. El-Mashade, A. Abdelnaiem, W. El-Deeb, and N. Tawfik, 'Analysis of Weak and Strong Fiber Bragg Grating', *British Journal of Applied Science & Technology*, vol. 10, no. 6, pp. 1–17, Jan. 2015, doi: 10.9734/BJAST/2015/18898.

[104] Z. Tian *et al.*, 'Refractive Index Sensing With Mach–Zehnder Interferometer Based on Concatenating Two Single-Mode Fiber Tapers', *IEEE Photon. Technol. Lett.*, vol. 20, no. 8, pp. 626–628, Apr. 2008, doi: 10.1109/LPT.2008.919507.

[105] T. K. Yadav, R. Narayanaswamy, M. H. Abu Bakar, Y. M. Kamil, and M. A. Mahdi, 'Single mode tapered fiber-optic interferometer based refractive index sensor and its application to protein sensing', *Opt. Express*, vol. 22, no. 19, p. 22802, Sep. 2014, doi: 10.1364/OE.22.022802.

[106] M. Z. Muhammad, A. A. Jasim, H. Ahmad, H. Arof, and S. W. Harun, 'Non-adiabatic silica microfiber for strain and temperature sensors', *Sensors and Actuators A: Physical*, vol. 192, pp. 130–132, Apr. 2013, doi: 10.1016/j.sna.2012.12.036.

[107] P. Lu, L. Men, K. Sooley, and Q. Chen, 'Tapered fiber Mach–Zehnder interferometer for simultaneous measurement of refractive index and temperature', *Applied Physics Letters*, vol. 94, no. 13, p. 131110, Mar. 2009, doi: 10.1063/1.3115029.

[108] M. Barbu, K. Jovanovich, R. Trahan, and P. Chirlian, 'The use of tapered fibers in an intensity based single mode temperature sensor', in *2nd ISA/IEEE Sensors for Industry Conference*, Houston, TX, USA, 2002, pp. 47–50, doi: 10.1109/SFICON.2002.1159806.

[109] Zhaobing Tian and S. S.-H. Yam, ‘In-Line Abrupt Taper Optical Fiber Mach–Zehnder Interferometric Strain Sensor’, *IEEE Photon. Technol. Lett.*, vol. 21, no. 3, pp. 161–163, Feb. 2009, doi: 10.1109/LPT.2008.2009360.

[110] D. Monzon-Hernandez, A. Martinez-Rios, I. Torres-Gomez, and G. Salceda-Delgado, ‘Compact optical fiber curvature sensor based on concatenating two tapers’, *Opt. Lett.*, vol. 36, no. 22, p. 4380, Nov. 2011, doi: 10.1364/OL.36.004380.

[111] J.-M. Hsu, C.-L. Lee, H.-P. Chang, W. C. Shih, and C.-M. Li, ‘Highly Sensitive Tapered Fiber Mach–Zehnder Interferometer for Liquid Level Sensing’, *IEEE Photon. Technol. Lett.*, vol. 25, no. 14, pp. 1354–1357, Jul. 2013, doi: 10.1109/LPT.2013.2265738.

[112] D. Tiwari, K. Mullaney, S. Korposh, S. W. James, S.-W. Lee, and R. P. Tatam, ‘An ammonia sensor based on Lossy Mode Resonances on a tapered optical fibre coated with porphyrin-incorporated titanium dioxide’, *Sensors and Actuators B: Chemical*, vol. 242, pp. 645–652, Apr. 2017, doi: 10.1016/j.snb.2016.11.092.

[113] Z. Yu, L. Jin, L. Sun, J. Li, Y. Ran, and B.-O. Guan, ‘Highly Sensitive Fiber Taper Interferometric Hydrogen Sensors’, *IEEE Photonics J.*, vol. 8, no. 1, pp. 1–9, Feb. 2016, doi: 10.1109/JPHOT.2015.2507369.

[114] B. Li, L. Jiang, S. Wang, L. Zhou, H. Xiao, and H.-L. Tsai, ‘Ultra-Abrupt Tapered Fiber Mach-Zehnder Interferometer Sensors’, *Sensors*, vol. 11, no. 6, pp. 5729–5739, May 2011, doi: 10.3390/s110605729.

[115] Di Wu, Yong Zhao, and Qi Wang, ‘SMF Taper Evanescent Field-Based RI Sensor Combined With Fiber Loop Ring Down Technology’, *IEEE Photon.*

Technol. Lett., vol. 27, no. 17, pp. 1802–1805, Sep. 2015, doi: 10.1109/LPT.2015.2443128.

[116] T. Osuch, K. Markowski, and K. Jedrzejewski, 'Temperature Independent Tapered Fiber Bragg Grating-Based Inclinometer', *IEEE Photonics Technology Letters*, vol. 27, no. 21, pp. 2312–2315, Nov. 2015, doi: 10.1109/LPT.2015.2462334.

[117] L. Liu, H. Zhang, Q. Zhao, Y. Liu, and F. Li, 'Temperature-independent FBG pressure sensor with high sensitivity', *Optical Fiber Technology*, vol. 13, no. 1, pp. 78–80, Jan. 2007, doi: 10.1016/j.yofte.2006.09.001.

[118] B. N. Shivananju *et al.*, 'CO2 sensing at room temperature using carbon nanotubes coated core fiber Bragg grating', *Review of Scientific Instruments*, vol. 84, no. 6, p. 065002, Jun. 2013, doi: 10.1063/1.4810016.

[119] S. Saad and L. Hassine, 'Hydrogen detection with FBG sensor technology for disaster prevention', *Photonic Sensors*, vol. 3, no. 3, pp. 214–223, Sep. 2013, doi: 10.1007/s13320-013-0109-4.

[120] F. Ahmed, V. Ahsani, A. Saad, and M. B. G. Jun, 'Bragg Grating Embedded in Mach-Zehnder Interferometer for Refractive Index and Temperature Sensing', *IEEE Photonics Technology Letters*, vol. 28, no. 18, pp. 1968–1971, Sep. 2016, doi: 10.1109/LPT.2016.2580582.

[121] Q. Yao *et al.*, 'A sandwich fiber sensor for simultaneous measurement of RI and temperature', in *2017 16th International Conference on Optical Communications and Networks (ICOCN)*, Wuzhen, Aug. 2017, pp. 1–4, doi: 10.1109/ICOCN.2017.8121353.

[122] Y. Cao, C. Zhao, and Z. Tong, ‘All fiber sensor based on Mach-Zehnder interferometer for simultaneous measurement of temperature and refractive index’, *Optoelectronics Letters*, vol. 11, no. 6, pp. 438–443, Nov. 2015, doi: 10.1007/s11801-015-5175-y.

[123] C. R. Liao, Y. Wang, D. N. Wang, and M. W. Yang, ‘Fiber In-Line Mach–Zehnder Interferometer Embedded in FBG for Simultaneous Refractive Index and Temperature Measurement’, *IEEE Photonics Technology Letters*, vol. 22, no. 22, pp. 1686–1688, Nov. 2010, doi: 10.1109/LPT.2010.2079924.

[124] X. Yu, X. Chen, D. Bu, J. Zhang, and S. Liu, ‘In-Fiber Modal Interferometer for Simultaneous Measurement of Refractive Index and Temperature’, *IEEE Photonics Technology Letters*, vol. 28, no. 2, pp. 189–192, Jan. 2016, doi: 10.1109/LPT.2015.2489559.

[125] J. Li *et al.*, ‘Long-Period Fiber Grating Cascaded to an S Fiber Taper for Simultaneous Measurement of Temperature and Refractive Index’, *IEEE Photon. Technol. Lett.*, vol. 25, no. 9, pp. 888–891, May 2013, doi: 10.1109/LPT.2013.2255035.

[126] P. Niu, J. Zhao, C. Zhang, H. Bai, X. Sun, and J. Bai, ‘Reflective Intensity-Demodulated Refractometer Based on S Fiber Taper’, *IEEE Photonics Technology Letters*, vol. 30, no. 1, pp. 55–58, Jan. 2018, doi: 10.1109/LPT.2017.2773638.

[127] Yanfang Lu, Changyu Shen, Chuan Zhong, Debao Chen, Xinyong Dong, and Jinhui Cai, ‘Refractive Index and Temperature Sensor Based on Double-Pass M–Z Interferometer With an FBG’, *IEEE Photonics Technology Letters*, vol. 26, no. 11, pp. 1124–1127, Jun. 2014, doi: 10.1109/LPT.2014.2315804.

[128] Q. Yao *et al.*, ‘Simultaneous measurement of refractive index and temperature based on a core-offset Mach–Zehnder interferometer combined with a fiber Bragg grating’, *Sensors and Actuators A: Physical*, vol. 209, pp. 73–77, Mar. 2014, doi: 10.1016/j.sna.2014.01.017.

[129] Y. Bai, B. Yin, C. Liu, S. Liu, Y. Lian, and S. Jian, ‘Simultaneous Measurement of Refractive Index and Temperature Based on NFN Structure’, *IEEE Photonics Technology Letters*, vol. 26, no. 21, pp. 2193–2196, Nov. 2014, doi: 10.1109/LPT.2014.2350023.

[130] Y. Cao, H. Liu, Z. Tong, S. Yuan, and S. Zhao, ‘Simultaneous measurement of temperature and refractive index based on a core-offset Mach-Zehnder interferometer cascaded with a long-period fiber grating’, *Optoelectron. Lett.*, vol. 11, no. 1, pp. 69–72, Jan. 2015, doi: 10.1007/s11801-015-4127-x.

[131] M. Zhou, X. Dong, and X. Liu, ‘Simultaneous measurement of temperature and refractive index with thin-core fiber MZI containing fiber Bragg grating’, in *2017 16th International Conference on Optical Communications and Networks (ICOCN)*, Wuzhen, Aug. 2017, pp. 1–3, doi: 10.1109/ICOCN.2017.8121291.

[132] Z. Shao, X. Qiao, W. Bao, and Q. Rong, ‘Temperature-independent gas refractometer based on an S-taper fiber tailored fiber Bragg grating’, *Optics Communications*, vol. 374, pp. 34–38, Sep. 2016, doi: 10.1016/j.optcom.2016.04.051.

Chapter 3

Interrogation of Fiber Bragg Grating Arrays by Illumination Using a Low Coherence Interferogram

3.1 Introduction

Conventional interferometric interrogation schemes for fibre Bragg grating (FBG) sensors are limited in terms of the number of sensors that can be simultaneously interrogated. Moreover, the conventional schemes cannot simultaneously interrogate multiple FBG sensors with similar wavelengths due to spectral overlap. This chapter investigates the capability of an interferometric interrogation scheme to interrogate multiple arrays of multiple Bragg grating sensors simultaneously. By the unique approach of illuminating the sensors with a low coherence interferogram, the simultaneous interrogation of sensors with similar peak wavelengths across multiple arrays is permitted along with the added benefit of scalability of the number of sensors that can be interrogated.

A Bragg grating is an optical device with periodic changes in the refractive index which results in the reflection of a bandwidth of light characteristic to the device. The bandwidth of light reflected by a Bragg grating is characterised by the period of the grating. A Bragg grating inscribed on an optical fibre by exposing the core to an intense optical interference pattern is called an FBG. The FBGs can be used to measure several parameters such as temperature, pressure, strain, vibration, displacement, etc. Numerous interrogation schemes have been reported for interrogation of a single [1], dual [2] and multiplexed arrays of sensors with varied resolutions and multiplexing capabilities [3]–[10]. Other similar interrogation schemes have been reviewed in Section 2.11.1.

When compared to alternative interrogation techniques, interferometric interrogation techniques offer advantages of multiplexing and throughput [11]. Interferometric spectroscopy is typically implemented as Fourier transform spectroscopy and requires long scans, and consequently long scan times, to provide high resolution [12]. High-resolution measurement has also been demonstrated from much shorter scans using Hilbert transform processing technique (HTT) [13]. The HTT has been shown to achieve high-resolution interferometric interrogation of an FBG array using an all-fibre interferometer, where the scanning was done by stretching a fibre spool using a piezoelectric fibre stretcher [14].

In a typical interferometric system, broadband light illuminates the sensors being interrogated and the reflected light is directed into an interrogating interferometer. This method of implementation cannot interrogate sensors of similar (or identical) wavelengths due to spectral overlap. The work reported here describes the implementation of an all-fibre interferometric interrogation technique which is capable of interrogation of both similar wavelength sensors and multiple arrays of sensors in a single interferometric scan.

Unlike the typical interferometric systems described above, this system illuminates the arrays of FBGs with the broadband interferogram generated by an all-fibre Michelson interferometer scanning through an optical path difference (OPD) of ~13mm. The FBGs then reflect (filter) narrow band interference patterns from the illuminating broadband interference patterns. These narrowband interference patterns are processed to provide a high-resolution measurement of all the FBGs across all the arrays. This unique approach makes the number of sensor arrays scalable unlike the other FBG interrogation schemes reviewed and it also permits the use of FBGs with similar wavelengths across the different arrays.

3.2 Theory

The working of an FBG sensor has already been discussed in Section 2.9.2 of Chapter-2 of this document. When illuminated with a broadband of light, an FBG reflects a very narrow wavelength of light characteristic to it. The wavelength of light reflected by a Bragg grating is given by Equation (2-65) as follows,

$$\lambda_B = 2n_{eff}\Lambda \tag{2-65}$$

where, λ_B is the Bragg wavelength, n_{eff} is the effective refractive index of the grating and Λ is the grating's period.

Changes to the grating's period will result in a corresponding change in the Bragg wavelength. By making use of this property, FBGs are used in sensing applications. FBGs are primarily sensitive to strain and temperature and sensitivities to other physical forces such as pressure, acceleration, etc., are derived from the sensitivities to primary forces.

The change in wavelength of light reflected by an FBG can be expressed as a function of strain, *l* and temperature, *T*. The reflected wavelength change, strain and temperature dependency is given by the following equation [15],

$$\Delta\lambda = 2\left(\Lambda\frac{\partial n_{eff}}{\partial T} + n_{eff}\frac{\partial \Lambda}{\partial T}\right)\Delta T + 2\left(\Lambda\frac{\partial n_{eff}}{\partial l} + n_{eff}\frac{\partial \Lambda}{\partial l}\right)\Delta l \tag{3-1}$$

While the strain dependency is due to the coefficient of elasticity, the temperature dependency is due to the thermo-optic coefficient and the coefficient of thermal expansion of the fibre. In a two-beam interferometer, interference can be expressed as the superposition of two waves and the interference is given by [16],

$$S(\tau) = A(\tau) \cos \phi(\tau) \tag{3-2}$$

where A(τ) is the slowly varying function of τ, ϕ(τ) is the instantaneous phase of the sinusoidal fringe.

The broadband interferogram of the source generated by the interferometer is spectrally filtered by each FBG which reflect narrowband interferograms characterized by the FBG's operational wavelength. The interferogram from the multiplexed FBGs is due to the superposition of individual FBG interferograms as given by the following equation.

$$S(\tau) = \sum_i S_i(\tau) \tag{3-3}$$

According to the *Wiener-Khinchin theorem*, the Fourier transform of the interferogram yields the spectral distribution of the source and as a result, interferometry which is typically implemented as Fourier transform spectroscopy is used for interrogation of FBG sensors. The wavelength resolution of FTS is given by,

$$\Delta\lambda = \frac{\lambda_c^2}{OPD} \tag{3-4}$$

where λ_c^2 is operating source wavelength and OPD is optical path delay or the scan length of the interferometer.

The analytic signal of the measurement FBGs is obtained by applying inverse Fourier transform to the spectrum of the FBG peaks.

$$H_i(\tau) = F^{-1}[2u(\omega)(F\{S_i(\tau)\}] \tag{3-5}$$

In Equation (3-5), $H_i(\tau)$ denotes the analytic signal, F the Fourier transform and 2u(ω) the Heaviside step function. The analytic signal has an imaginary and a real part, where the imaginary component is a 90-degree phase shifted version of the real component. The instantaneous phase values of individual FBGs $\phi_i(\tau)$ and thereafter the wavelengths are obtained from imaginary and real components [17] as described in Section 2.10.6.

3.3 Experimental Setup

The interferometer constructed is an unbalanced all-fibre Michelson interferometer in which an OPD of ~13mm is generated by the piezo fibre stretcher (PFS) (Evanescent Optics, Fibre Stretcher, Model 916B), when modulated with a 1Hz sine wave with a 5V DC offset. The Faraday rotor mirrors FRM1 and FRM2 are used to reduce polarization induced fading in the fibre. Circulator (C) directs the light from a broadband source (BBS) with a centre wavelength of 1550nm into the interferometer, and the interferogram generated by the interferometer towards the FBG arrays. The Isolators I1, I2, and I3 prevent narrow bandwidth interferograms reflected by the FBGs from coupling into other arrays.

While the directional coupler DC1 is used to illuminate the arms of the interferometer, FBG arrays are illuminated with the interferogram generated by the Michelson interferometer via the directional couplers DC2, DC3. The light reflected from FBG arrays is detected using photodiodes, PD1, PD2, and PD3. 600k samples of interferometric signals from PDs are logged on a PC using a high-speed data acquisition unit (DAQ) (NI-PCI-6023E) at a sampling frequency of 60kHz.

FBG1 (~1549nm) is used for referencing the measurement sensors FBG2(~1549nm) and FBG3(~1566nm) in array one and measurement sensors

FBG4(~1549nm), FBG5(~1555nm) and FBG6(~1560nm) in array two. All the FBGs had an FWHM of ~0.19nm.

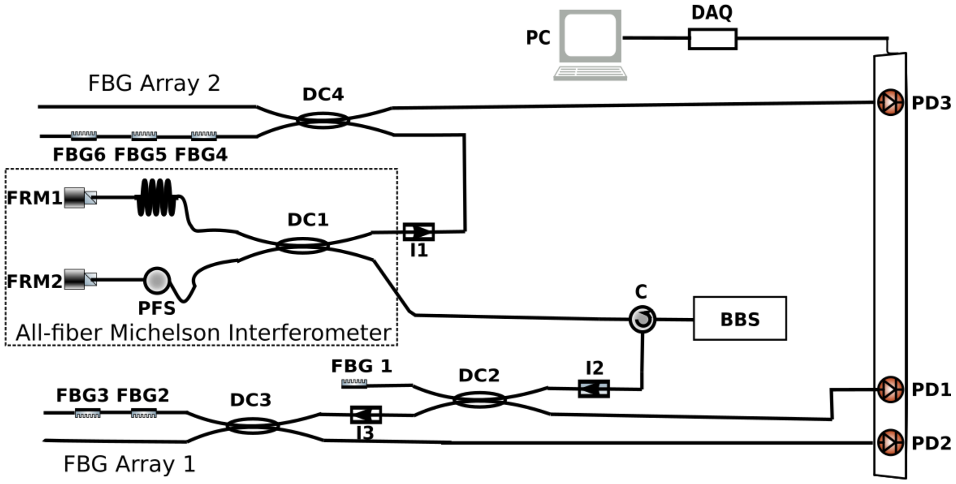

Figure 3-1: Interferometer setup

Sensing capabilities of the system were investigated by subjecting FBGs 5 and 6 to a change in temperature ranging from 30^{0}C to 150^{0}C in steps of 10^{0}C using a Periodically Poled Lithium Niobate (PPLN) oven. Throughout the test, reference FBG was stabilised on a Peltier module.

3.4 Results

A single scan of the all-fibre Michelson interferometer yields a broadband interferogram of the illuminating broadband superluminescent diode (SLED). Figure 3-2(A) shows a sample plot of the interferogram. The generated interferogram is transmitted to one measurement arm through the circulator and the other arm through the isolator I1.

When illuminated with a broadband interferogram, the FBG arrays reflect back narrowband interferograms. The narrowband interferograms reflected by the reference FBG1 and one array of measurement sensors FBG4, FBG5 and FBG6 can be seen in Figure 3-2 (B) and Figure 3-2 (C) respectively. Similar narrowband interferogram was also obtained for the array of FBG2 and FBG3 sensors.

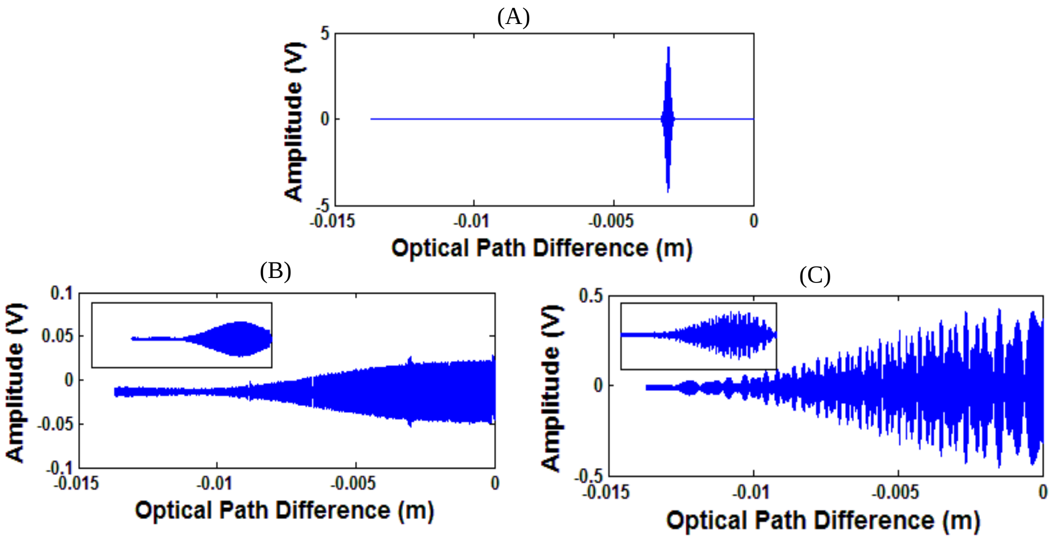

Figure 3-2: Plots of (A) Broadband interferogram of the source, (B) Narrowband interferogram from the reference sensor and (C) Narrowband interferogram from the sensor array

Due to the Gain-Bandwidth product of the detector, the operational frequency bandwidth of the detector reduces with increasing gain. For the experiment, the PDs were operated under reduced frequency bandwidth as seen in Figure 3-2 (B) and Figure 3-2 (C). Subsequently, frequency bandwidth was increased to capture the interferogram envelope, which can be seen in the insets of Figure 3-2 (B) and Figure 3-2 (C).

Due to the non-linear motion of the PFS and uneven delay sampling, the Fourier transform of the measurement interferograms yields additional spectral content. Hence, the gratings' individual spectra are not clearly visible in the plot shown in Figure 3-3. After delay calibration using HTT as outlined in Chapter-2, the FBG peaks become clearly resolvable as seen in Figure 3-4. The spectrum of sensors in Figure 3-4 (C) is noisier than the other spectra due to the fibre to free space arrangement used to illuminate the free space photodiode PD2

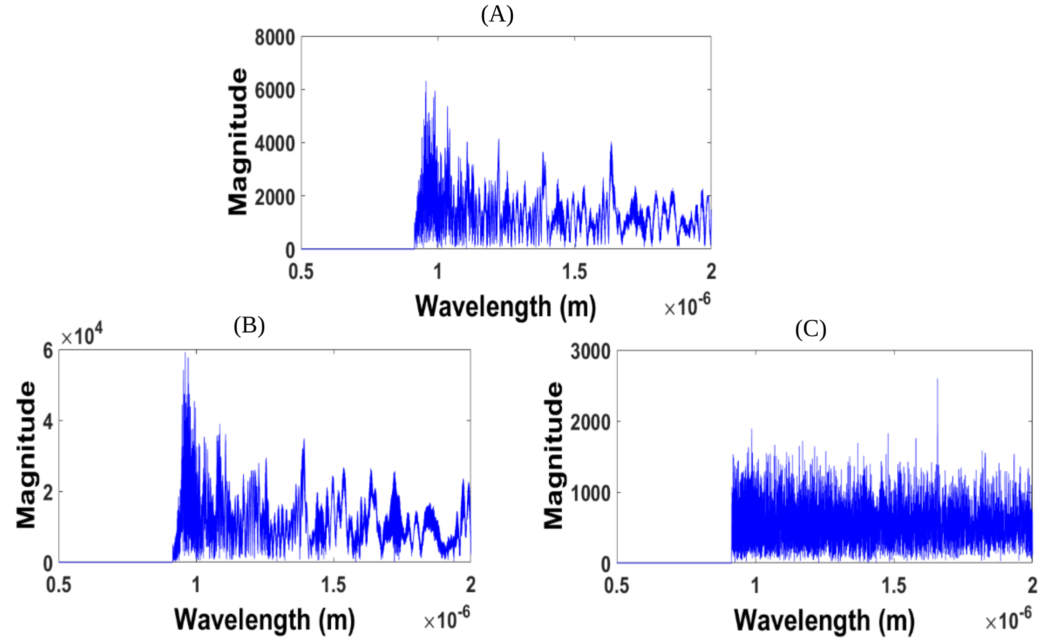

Figure 3-3: Uncalibrated spectrum of (A) Reference FBG, (B) Measurement sensor array 2 and (C) Measurement sensor array 1

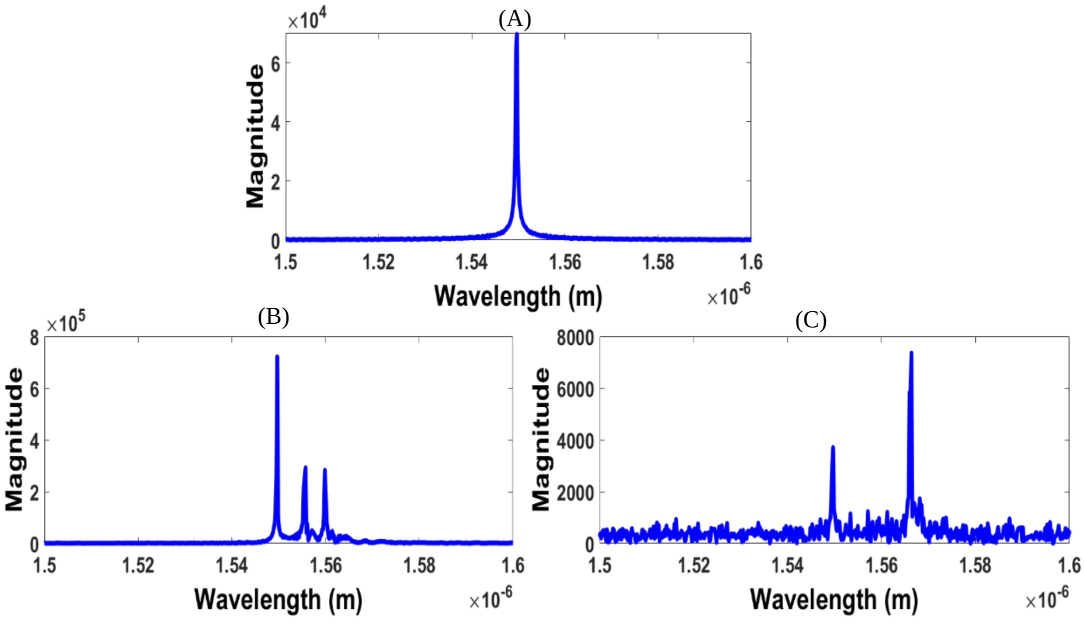

Figure 3-4: Spectra of (A) Reference FBG, (B) Sensors from measurement array 2 and (C) Sensors from measurement array 1

Following calibration, the individual FBG peaks are segmented by windowing and then their respective phase vectors are obtained using Equation (2-87).

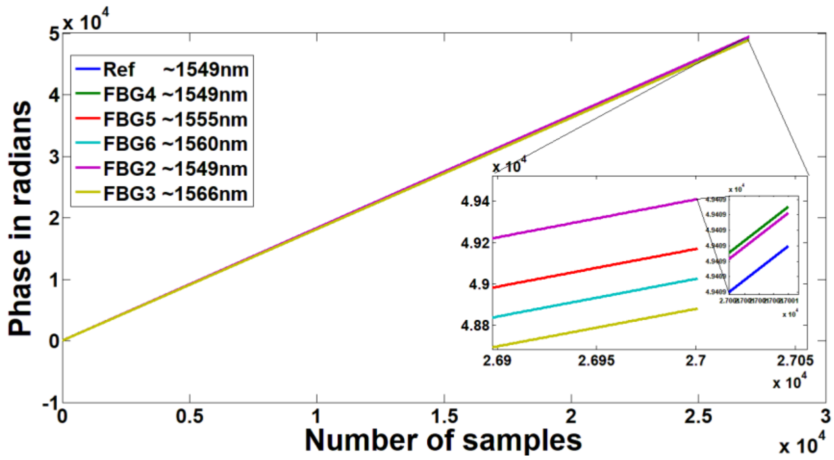

Figure 3-5: Temporal phase vectors of the sensors

The wavelengths of the measurement sensors at various temperature instances were calculated and plotted as a function of temperature as shown in Figure 3-6. A linear fit to the data yielded a resolution of ~9.03pm/^{0}C in case of FBG5 and ~9.23pm/^{0}C in case of FBG6.

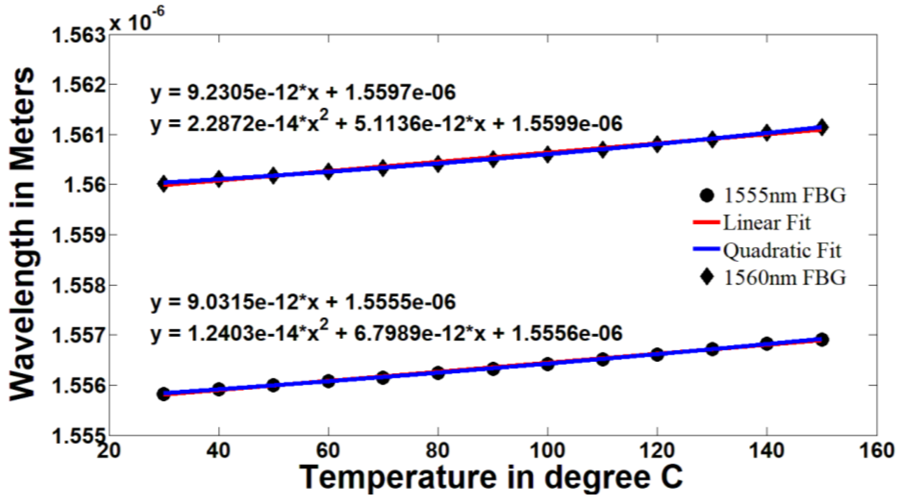

Figure 3-6: Temperature vs Wavelength plot of sensors

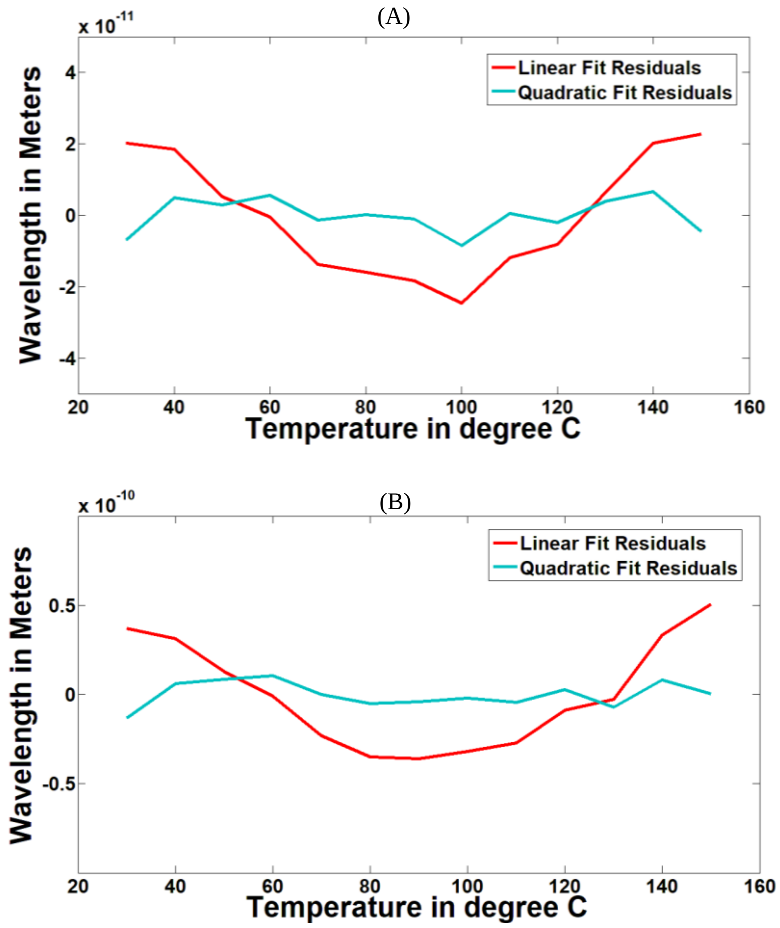

Figure 3-7: Plot of residuals of (A) FBG5 (1555nm) and (B) FBG6 (1560nm)

The deviation of the measurement points from both the linear and quadratic fits is shown in the plot of residuals in Figure 3-7. When compared to the linear fit residual values, the reduced quadratic fit residual values can be attributed to the quadratic nature exhibited by the FBGs [18]. The measurement accuracy is the range or extremity values of the fit residuals shown in Figure 3-7. To estimate the overall measurement accuracy, the difference between the maximum and minimum quadratic residuals was taken and resulted in ±8pm in case of FBG5 and ~±12pm in case of FBG6.

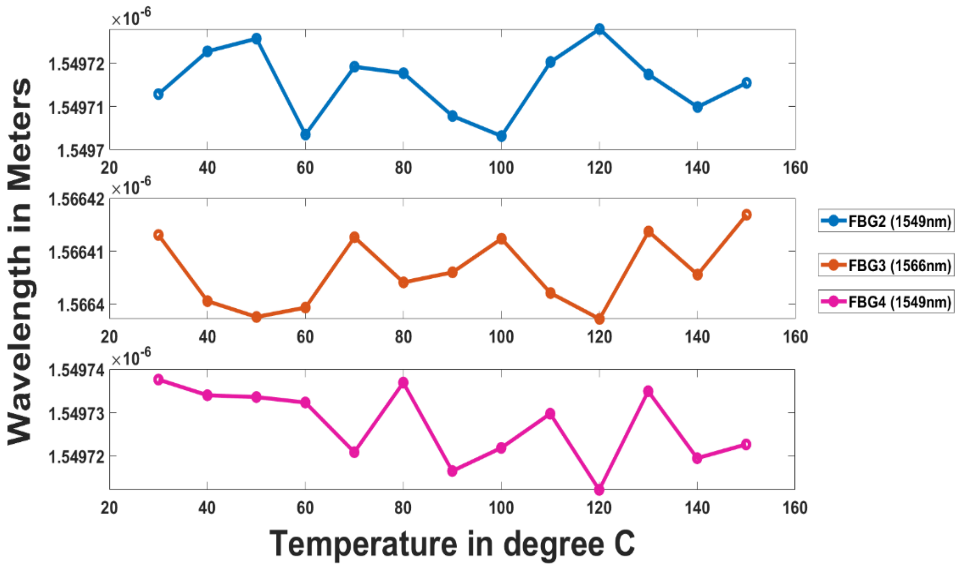

Figure 3-8: Plot of FBGs with similar wavelengths

A plot of the peak values of FBGs that were not subjected to the temperature change test is shown in Figure 3-8 demonstrating the capability of the system to simultaneously interrogate the FBGs with similar wavelengths (1549nm in this case). FBG Peak values in Figure 3-8 have been plotted against temperature for comparison with the FBGs that were subjected to the temperature test. Change in the sensors' wavelength over the course of the test is presented in Table 3-1.

Table 3-1: Change in wavelength of the sensors

Sensor	Range of change in wavelength (nm)
FBG2(~1549nm)	0.0247
FBG3(~1566nm)	0.0196
FBG4(~1549nm)	0.0254
FBG5(~1555nm)	1.086
FBG6(~1560nm)	1.121

From the plot (Figure 3-8) and Table 3-1, the range of change in peak values of the sensors that were not subjected to the temperature test can be seen to be negligible when compared against the sensors that were subjected to the temperature test. The range of FBG2, FBG3 and FBG4 was approximately 2% of the range of the sensors FBG5 and FBG6. This demonstrates negligible crosstalk between the sensors. The results presented above from this experimental chapter are discussed below.

3.5 Discussion

The experimental results reported are in concurrence with the FBG sensors' typically quadratic response to the temperature changes as previously demonstrated by Flockhart [18]. The quadratic temperature response is due to the FBG's dual dependency on the thermal expansion coefficient and the thermo-optic coefficient which in turn is influenced by the excitonic bandgap.

Standard deviation in the peak wavelengths of the FBG sensors that were not subjected to a temperature test were within ±7pm. Thus, the measurement resolution is ~7pm for the ~13mm OPD scan. The 7pm resolution is at least twice greater than the 15pm resolution previously reported using Fourier transform spectroscopy, for $1/23^{rd}$ of the OPD [12]. This demonstrates the efficacy of HTT to provide high resolution measurements for much shorter OPD. However, the 7pm resolution reported in this chapter is lower than the 5pm for 1.2mm OPD [13] and 3pm for 8mm OPD (windowed to 6.3mm) [19] previously reported. The reduced resolution can be attributed to the use of an FBG with a typical FWHM of 0.19nm for referencing. On the contrary, in the studies reporting high resolution [13], [19], a reference source with a linewidth in the range of few pico-meters were used. A narrow linewidth interferometric signal has increased number of fringes and thus more points for delay sampling yielding higher resolutions. The experimental setup used in this chapter does not permit the use of a second optical source for referencing. But the resolution can be further improved by using an FBG with a narrower spectral bandwidth.

3.6 Conclusion

The scheme of interrogation by interferometric illumination has shown to interrogate multiple arrays of wavelength division multiplexed FBG sensors simultaneously without forgoing optical throughput or sensor bandwidth.

Unlike the conventional interferometric interrogation system based on FTS, FBGs with similar wavelengths across the different sensor arrays were simultaneously interrogated by interferometric illumination of the sensors. As a result of this unique approach, the number of sensors that can be interrogated in a single interferometric scan can be increased multiple times the conventional approach without forgoing the measurement resolution. The demonstrated technique has shown to yield resolutions comparable with the ~8pm/^{0}C resolution previously reported [14]. From the quadratic fits to the measurement data and from the fit residuals, the quadratic nature of FBG previously demonstrated by Flockhart [18] was ascertained.

The number of arrays which can be addressed by the above system depends on several factors like source power, required resolution, signal to noise levels and the number of channels on the DAQ. The density of the multiplexed sensors which can be interrogated in an individual array is dependent on the scanning frequency of the stretcher. As the OPD drops off with increasing scan frequency, a low-frequency signal was used to modulate the stretcher for generating maximum OPD. By increasing the OPD, the system resolution can be improved, and the sensor density can be increased.

In the next chapter, the capability and efficacy of the interferometric illumination system to interrogate an altogether different class of fibre optic sensor called the interferometric sensor is investigated.

3.7 References

[1] A. D. Kersey and M. A. Davis, 'All-fibre Bragg grating strain-sensor demodulation technique using a wavelength division coupler', *Electronics Letters*, vol. 30, no. 1, pp. 75–77, Jan. 1994, doi: 10.1049/el:19940059.

[2] M. A. Davis and A. D. Kersey, 'Matched-filter interrogation technique for fibre Bragg grating arrays', *Electronics Letters*, vol. 31, no. 10, pp. 822–823, May 1995, doi: 10.1049/el:19950547.

[3] M. A. Davis, D. G. Bellemore, M. A. Putnam, and A. D. Kersey, 'Interrogation of 60 fibre Bragg grating sensors with microstrain resolution capability', *Electronics Letters*, vol. 32, no. 15, p. 1393, 1996, doi: 10.1049/el:19960908.

[4] M. S. Muller *et al.*, 'Fiber-Optic Sensor Interrogation Based on a Widely Tunable Monolithic Laser Diode', *IEEE Transactions on Instrumentation and Measurement*, vol. 59, no. 3, pp. 696–703, Mar. 2010, doi: 10.1109/TIM.2009.2025987.

[5] D. F. Murphy, D. A. Flavin, R. McBride, and J. D. C. Jones, 'Interferometric Interrogation of In-Fiber Bragg Grating Sensors Without Mechanical Path Length Scanning', *J. Lightwave Technol.*, vol. 19, no. 7, p. 1004, Jul. 2001.

[6] M. Perry, P. Orr, P. Niewczas, and M. Johnston, 'High-Speed Interferometric FBG Interrogator With Dynamic and Absolute Wavelength Measurement Capability', *Journal of Lightwave Technology*, vol. 31, no. 17, pp. 2897–2903, Sep. 2013, doi: 10.1109/JLT.2013.2276391.

[7] Y. Marin, T. Nannipieri, C. Oton, and F. Di Pasquale, 'Integrated FBG Sensors Interrogation using Active Phase Demodulation on a Silicon Photonic

Platform', *Journal of Lightwave Technology*, pp. 1–1, 2016, doi: 10.1109/JLT.2016.2598395.

[8] D. Pustakhod, E. Kleijn, K. Williams, and X. Leijtens, 'High-Resolution AWG-Based Fiber Bragg Grating Interrogator', *IEEE Photonics Technology Letters*, vol. 28, no. 20, pp. 2203–2206, Oct. 2016, doi: 10.1109/LPT.2016.2587812.

[9] T. Yamaguchi and Y. Shinoda, 'Multichannel High-Speed Fiber Bragg Grating Interrogation System Utilizing a Field Programmable Gate Array', *IEEE Sens. Lett.*, vol. 2, no. 1, pp. 1–4, Mar. 2018, doi: 10.1109/LSENS.2017.2782670.

[10] I. Drazic-Segrt, A. Krnjak, M. Sprem, M. Bosiljevac, and Z. Sipus, 'Portable FBG based optical sensor array', Apr. 2015, pp. 1–5, doi: 10.1109/SAS.2015.7133657.

[11] Y. J. Rao, D. J. Webb, D. A. Jackson, L. Zhang, and I. Bennion, 'High-resolution, wavelength-division-multiplexed in-fibre Bragg grating sensor system', *Electronics Letters*, vol. 32, no. 10, p. 924, 1996, doi: 10.1049/el:19960589.

[12] M. A. Davis and A. D. Kersey, 'Application of a fiber Fourier transform spectrometer to the detection of wavelength-encoded signals from Bragg grating sensors', *Journal of Lightwave Technology*, vol. 13, no. 7, pp. 1289–1295, Jul. 1995, doi: 10.1109/50.400685.

[13] D. A. Flavin, R. McBride, and J. D. C. Jones, 'Short-scan interferometric interrogation and multiplexing of fibre Bragg grating sensors', *Optics*

Communications, vol. 170, no. 4–6, pp. 347–353, Nov. 1999, doi: 10.1016/S0030-4018(99)00515-5.

[14] K. T. O'Mahoney, R. P. O'Byrne, S. V. Sergeyev, Lin Zhang, and I. Bennion, 'Short-Scan Fiber Interferometer for High-Resolution Bragg Grating Array Interrogation', *IEEE Sensors Journal*, vol. 9, no. 10, pp. 1277–1281, Oct. 2009, doi: 10.1109/JSEN.2009.2029818.

[15] A. D. Kersey *et al.*, 'Fiber grating sensors', *Journal of Lightwave Technology*, vol. 15, no. 8, pp. 1442–1463, Aug. 1997, doi: 10.1109/50.618377.

[16] E. P. Goodwin and J. C. Wyant, *Field Guide to Interferometric Optical Testing*. 1000 20th Street, Bellingham, WA 98227-0010 USA: SPIE, 2006.

[17] K. B. Rochford and S. D. Dyer, 'Demultiplexing of interferometrically interrogated fiber Bragg grating sensors using Hilbert transform processing', *Journal of Lightwave Technology*, vol. 17, no. 5, pp. 831–836, May 1999, doi: 10.1109/50.762900.

[18] G. M. H. Flockhart *et al.*, 'Quadratic behavior of fiber Bragg grating temperature coefficients', *Applied Optics*, vol. 43, no. 13, p. 2744, May 2004, doi: 10.1364/AO.43.002744.

[19] K. O'Mahoney, 'Fourier Transform Spectroscopic Demodulation of Fibre Bragg Grating Arrays', PhD Thesis, Waterford Institute of Technology, 2007.

Chapter 4

High-resolution Tapered Sensor Interrogation by Interferometric Illumination

4.1 Introduction

Chapter-3 demonstrated the capability of an all-fibre interferometer to interrogate multiple arrays of multiple fibre Bragg grating sensors by interferometric illumination. By adopting the unique method of interferometric illumination from Chapter-3, this chapter investigates the interrogation of tapered fibre optic sensors with resolutions higher than the ones typically obtained using an optical spectrum analyser.

A class of optical fibre in which the light guided interfere within the fibre and whose spectral fringes' properties are sensitive to varying physical forces like temperature, strain, etc. are called fibre optic interferometric sensors (FOIS) [1]. Under the class of FOIS, non-adiabatic tapered sensors (TS) are typically used for sensing refractive index changes [2]–[6]. Tapered sensors work on the principles of evanescent wave sensing. The theory behind evanescent wave sensing has already been dealt with in detail in Section 2.9.3 of Chapter-2 of this document. By studying the sensor's evanescent field interaction with the medium surrounding the sensor, changes to the medium's physical characteristics can be quantified.

In a commonly used TS based sensing arrangement, the sensor is illuminated with a broadband source and the interrogation unit (OSA or spectrometer or optical power meter) is placed at the end of sensor line for monitoring changes to a sensor's spectral fringes' phase or intensity [4]–[8]. Interrogation using OSA yields only the spectral information of the sensor. Additionally, in an OSA with a monochromator, the peak power reduces with increasing resolution, compounded by the increased attenuation in the fibre due to tapering and this tends to reduce the signal to noise ratio. As a result, non-adiabatic tapered sensors are interrogated with low resolution scans. The minimum detectable phase change to the sensor's spectrum is inversely dependent on the OSA's scanning resolution and as a result, with lower resolution scans, the minimum detectable phase change is high.

On the other hand, interferometric interrogation of sensors poses numerous advantages such as multiplexablity (Fellgett advantage) [9], high throughput (Jacquinot advantage) [10], high accuracy (Connes advantage) [11]. Interrogation of TS using an interferometer yields not only the temporal information of the sensor but also supports high-resolution measurements ensuing from the mechanical scans of the interferometer.

In this chapter, TS interrogation by interferometric illumination using an unbalanced all-fibre Michelson interferometer is presented in an attempt to, overcome the existing limitations of TS interrogation using an OSA. A low coherence interferogram is first generated by modulating the piezo fibre stretcher in the Michelson interferometer with a 1Hz waveform and the interferogram is then used to illuminate the tapered sensor. The low coherence interferogram modulated by the tapered sensor is then processed using Hilbert transform processing technique (HTT) for measuring the changes in sensor's phase as HTT has previously been used for obtaining high-resolution measurements for short scans of interferometer [12], [13].

Tapered sensors have previously been used for evanescent wave sensing of gases such as CO_2, hydrogen, methane, etc [14]–[19] and alcohol vapour [20], [21]. Hence, ethanol vapour is used as a stimulus to induce the shift in the sensor's spectral phase and to demonstrate the efficacy of the interferometric interrogation setup used. The results obtained have been found to be repeatable with three trials yielding similar phase change results. The label-free sensor was also found to retract automatically to its initial state briefly after removing the ethanol vapour source. Theory behind the refractive index sensing using a TS and the evaporation of ethanol is briefly discussed below.

4.2 Theory

Tapered fibre

An optical fibre with a section of reduced diameter is called a tapered optical fibre/tapered fibre. The tapered fibre has sections of gradually changing diameter called the transition region and a section of uniformly reduced diameter called the waist region. The waist region is such that the core of the fibre gets mixed with the cladding to form a medium whose refractive index is almost close to that of the cladding. For elaborate details on the tapering processes typically used, the reader is referred to Section 2.9.3 of Chapter-2 of this document.

Due to the inter-modal interference, the intensity of the light transmitted by the fiber is given by the following equation [22],

$$I_T = I_{CO} + I_{CL} + 2\sqrt{I_{CO} I_{CL} \cos\varphi} \tag{4-1}$$

where I_T is the transmitted light intensity, I_{CO} is the intensity of core mode and I_{CL} is the intensity of cladding mode and φ is the phase difference between two modes. Basically, it is a two beam interferometer of fixed optical path difference. So, the phase difference at the output will depend on the wavelength that is used. As a result, if we scan the wavelength or illuminate with a broadband source we will see sinusoidal fringes in the output spectrum. The spacing between the sinusoidal fringes in the spectrum is called the free spectral range (FSR) and is given by [23], [24],

$$FSR = \frac{\lambda^2}{(n_1 - n_2).l} \tag{4-2}$$

and the phase difference between two modes φ is given by, [4], [25],

$$\varphi = \frac{2\pi(n_1 - n_2)}{\lambda}.l \tag{4-3}$$

where n_1 is the refractive index of core, n_2 is the refractive index of cladding, l is the length of the taper and λ is the central wavelength of the source. Using Equations (4-2) and (4-3), the φ can be expressed in terms of FSR as,

$$\varphi = \frac{2\pi\lambda}{FSR} \tag{4-4}$$

Changes in the environment will result in a changing n_2 and therefore changes the output phase difference and the FSR of tapered fibre's spectral response [4], the latter of which can be measured.

The sensor's spectrum is obtained by the application of Fourier transform to the sensor interferogram (*Wiener-Khinchin theorem*). The period of the spectral fringes are then obtained using Hilbert transform processing method outlined in Section 2.10.6.

The work reported in this chapter uses ethanol for characterising the sensor and to demonstrate the capability of the interrogation system. Hence, the theory and nature of ethanol evaporation is discussed below.

Ethanol Evaporation

From the "Yellow Book" [26], the expression for the rate of ethanol evaporation is given by,

$$E = \frac{k_m . P_v . M_i}{R . T} \tag{4-5}$$

where, k_m denotes the mass transfer coefficient, P_v denotes its vapour pressure at temperature T, M_i denotes the molecular weight and R denotes the gas constant. Substituting the values of molecular weight and gas constant of ethanol in Equation (4-5) we get,

$$E = (2.548x10^{-4}) . \frac{k_m . P_v}{T} \tag{4-6}$$

The vapour pressure of liquids is dependent on the temperature. The inter-relationship is given by the Antoine equation [29],

$$P_v = exp\left(A - \frac{B}{C + T}\right) \tag{4-7}$$

Substituting Equation (4-7) in (4-6) we get,

$$E = (2.548x10^{-4})\left(\frac{k_m}{T}\right) exp\left(A - \frac{B}{C + T}\right) \tag{4-8}$$

where A, B, C are constants and T is the temperature in Kelvin. The values of constants A, B, and C vary depending upon the concentration of ethanol solution [28]. From the above Equation (4-8), the rate of evaporation of ethanol can be seen to vary exponentially with (1/temperature). However, at a constant temperature, as ethanol starts evaporating, the concentration of the ethanol molecules surrounding the sensor will increase at the onset of evaporation and subsequently decrease as the ethanol molecule concentration in the solution decreases and the ethanol in the air diffuses away.

4.3 Experimental setup

Interferometer constructed for interrogating a tapered sensor with high measurement resolution is shown in Figure 4-1. The scanning all-fibre Michelson interferometer is illuminated using a broadband superluminescent diode (Opto Speed SA, SLED1550SA) with a central wavelength at 1550nm. The optical path delay in the Michelson interferometer (MI) is generated by a piezo fibre stretcher (PFS) (Evanescent Optics, Fibre Stretcher, Model 916B). The optical path delay (OPD) generated by the fibre stretcher is dependent on the frequency of the signal used to modulate it (a graphical representation of the dependency is attached in the Appendix-B). A sinusoidal signal with 1Hz frequency is used to generate an OPD ~13mm. Faraday rotor mirrors FRM1 and FRM2 reduce the polarization induced fading in the fibre [29]. The circulator (C) directs the light from the source into the MI and the interferograms from the MI into the sensing arms. Isolators I1 and I2 are placed ahead of the directional couplers DC3 and DC2 respectively to prevent back reflections.

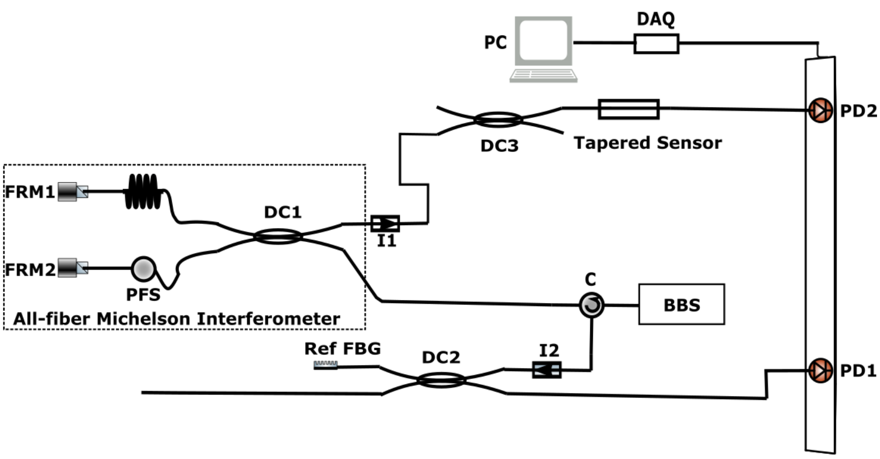

Figure 4-1: Interferometer setup for tapered sensor interrogation

Photodiodes PD1, PD2 (Newfocus 2053) are used to convert the light reflected by reference fibre Bragg grating (FBG) (peak wavelength ~1550nm, full width at half maximum < 0.25nm) and light transmitted via the tapered sensor into electrical signals. A high-speed data acquisition card (DAQ) (NI-USB-6341) is used to record the analogue signals from the photodiode on to a computer. The frequency response on both the photodiodes was set to 10k-100k Hz. For the tests, interferometric signals were recorded at 100kHz with a sampling density of 4 samples per fringe, much greater than the Nyquist sampling criterion [30].

A petri dish was placed in an acrylic enclosure measuring 20x8x12cms (Length x Height x Width, approx.) in dimension and the tapered sensor was fixated about 4cms above the petri dish. Two holes measuring 5mm in diameter were drilled on the lid for ventilation. After adding 2ml of 98% ethyl alcohol into the petri dish, capturing of interferometric signals at 5-minute intervals occurred. This involved 10 stretch and relax cycles every 5 minutes. Throughout the test duration of 120 minutes, the reference FBG remained stabilised on a Peltier module.

4.4 Results

To monitor the changing ethanol concentration, interferometric data is logged in 5 minute intervals for 120 minutes (25 data sets). Each of the interferometric data is 10 second long containing 20 interferograms i.e., 10 each from the stretching and relaxation of the stretcher. Overall, 500 interferograms each for the tapered sensor and the reference FBG sensor are processed for sensor response estimation. Samples of the broadband interferograms transmitted through the TS and the narrowband interferograms reflected by the reference FBG are shown in Figure 4-2.

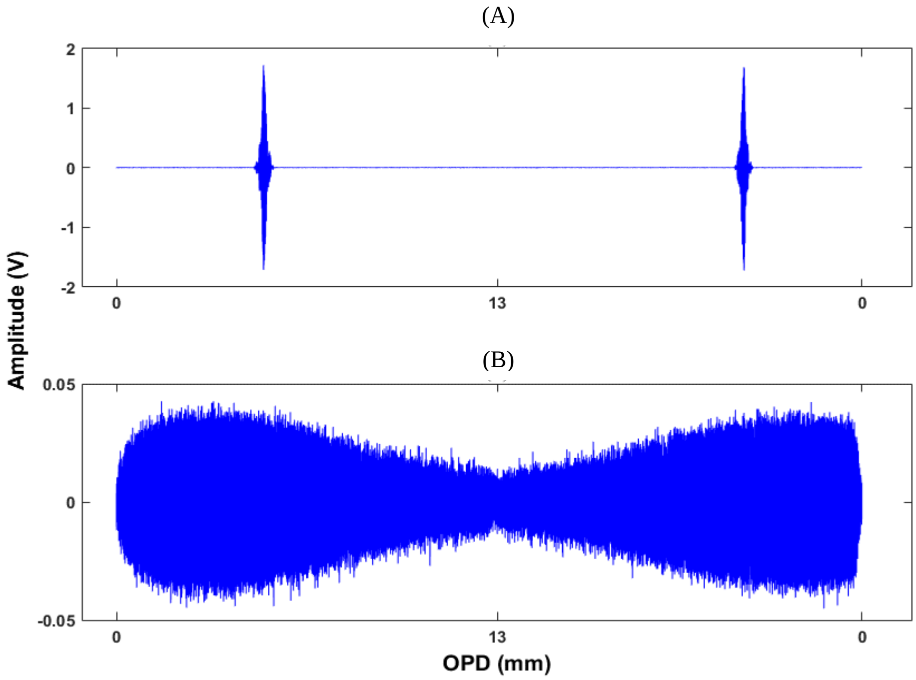

Figure 4-2: (A) - Interferograms transmitted through TS, (B) - Interferograms reflected by Ref FBG

Due to the non-linear motion of the fibre stretcher and uneven delay sampling, Fast Fourier Transform (FFT) of the interferograms yields additional spectral content as seen in Figure 4-3.

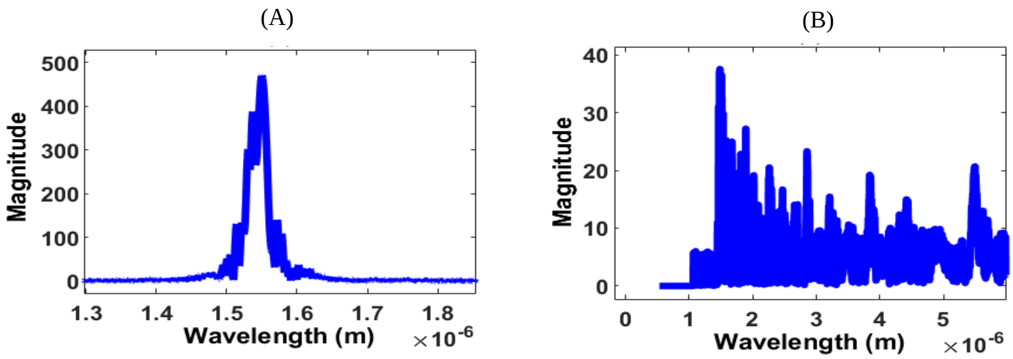

Figure 4-3: Uncalibrated spectra of (A) Tapered sensor and (B) Reference FBG

For delay calibration, the analytic signal of the reference interferogram is first obtained. Upon delay calibration by simulation of uniform OPD sampling using the reference analytic signal, the fringes of the broadband tapered sensor and the narrower band reference sensor peak become clearly resolvable. The recalibrated spectra can be seen in Figure 4-4. The tapered sensor spectrum in Figure 4-4 corresponds to the sensor spectrum when surrounded by air without ethanol. A sample plot of the sensor spectrum when surrounded by ethanol is presented in Figure 4-5. The magnitude of the spectra in Figure 4-3, Figure 4-4 and Figure 4-5 are represented by arbitrary units.

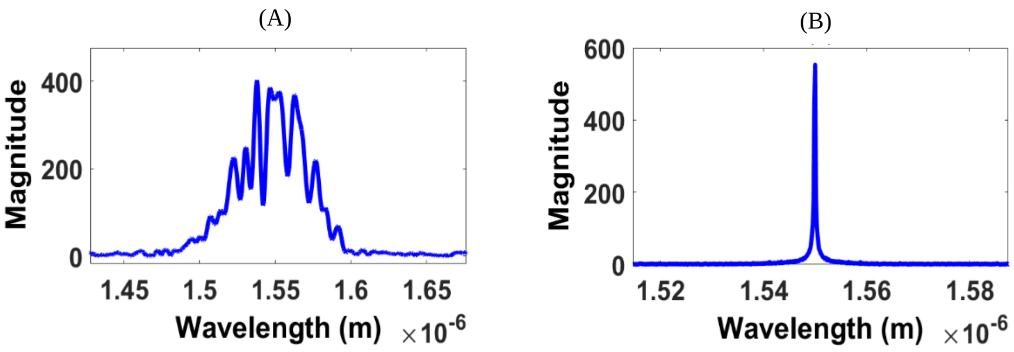

Figure 4-4: Recalibrated spectra of (A) Tapered sensor surrounded by air and (B) Reference FBG

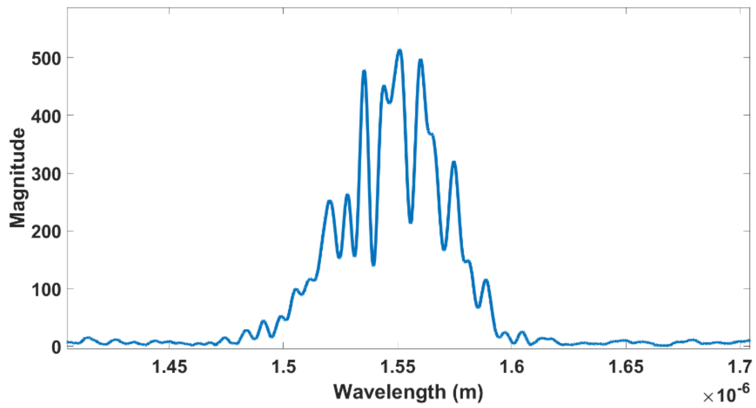

Figure 4-5: Sample of tapered sensor spectrum when surrounded by ethanol

To demonstrate the high-resolution measurement capability of interferometric interrogation of the sensor when compared to OSA, the results are first processed as is typically done when using an OSA, and thereafter compared with the results obtained from processing the recalibrated interferometric signals. Results obtained using the different approaches adopted for computing the sensor's phase change with the passage of time and rising ethanol vapour concentration are presented below.

Sensor phase estimation using spectral fringes

The recalibrated sensor spectrum is shown in Figure 4-4 (A). For computing phase changes using the recalibrated sensor spectra, first the offset is removed using a zero-phase filter. The zero-phase filter centres the sensor spectrum along the x-axis while preserving the spectral fringes' phase. Figure below shows the sensor spectrum after filtering. The x-axis has been set to wavelength for an idea of the operation.

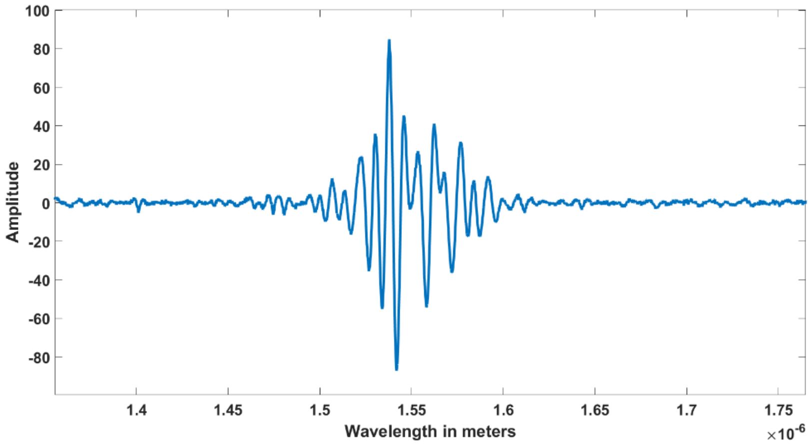

Figure 4-6: Sensor spectrum after filtering

The filtered spectrum contains datapoints for the entire scan length. For analysis using only the spectral fringes, following the filtering operation, the spectral fringes are segmented from the filtered spectrum. A sample plot of a sensor spectrum after segmentation is shown in Figure 4-7. It is to be noted that the spectrum in Figure 4-7 is a mirror image of the unsegmented spectrum in Figure 4-6 as the x-axis in Figure 4-6 is wavelength and the x-axis in Figure 4-7 is sample number.

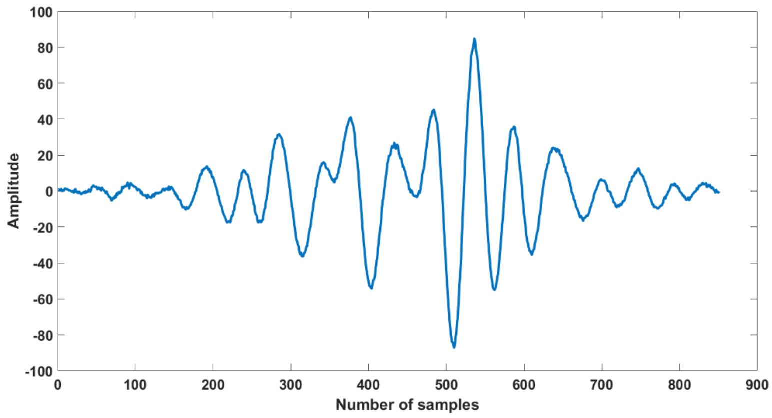

Figure 4-7: Sensor spectrum after segmentation

Using the Hilbert transform processing technique (HTT) previously discussed, the instantaneous phase vector of the segmented spectral fringes is obtained. Figure 4-8 shows the plot of the phase vector obtained from the segmented spectrum using HTT.

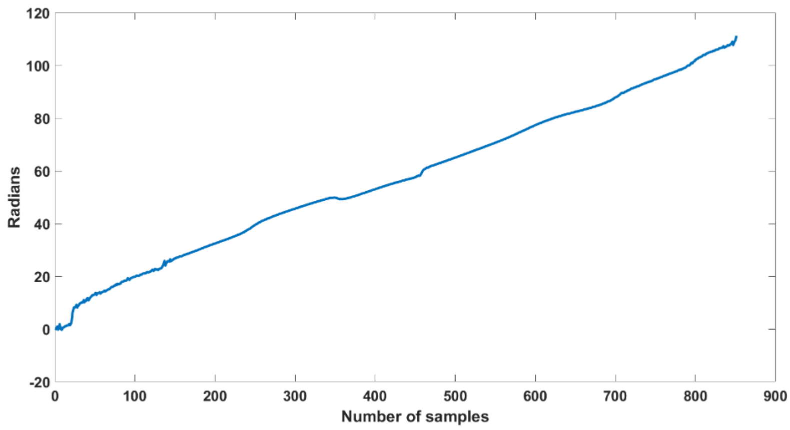

Figure 4-8: Phase vector of the filtered spectrum

To measure the sensor response to ethanol, first, spectral fringe phase vectors for each of the 500 interferogram samples are obtained using the method discussed above and the slopes of the individual phase vectors are then calculated and plotted on Figure 4-9. As the 0th minute data is treated as the reference for subsequent scans in the stretching and relaxation cycle, its value is always 1. 20 stretching/relaxation cycles are measured with 25 points per stretching and 25 per relaxation.

Next, for each time step, the median value for the 20 runs is calculated and displayed on Figure 4-10 together with error bars to reflect the spread of the data for each time step. The median is used instead of the average as it reduces the effect of outliers on the result. Various studies relating to ethanol sensing have shown exponential-like behavior in ethanol dynamics [20], [31]–[33] and so an exponential fit is applied to the ethanol dynamics (median data) to estimate the sensor response. The rate of the sensor's phase change or the measurement resolution as obtained from the exponential fit is ~(67±35)e-3/min. As the variable "b" seen in the fit window of Figure 4-10 is a time constant, the sensor response has a unit "per min (/min)". Results from two other trials have been shown in Figure 4-11 and Figure 4-12.

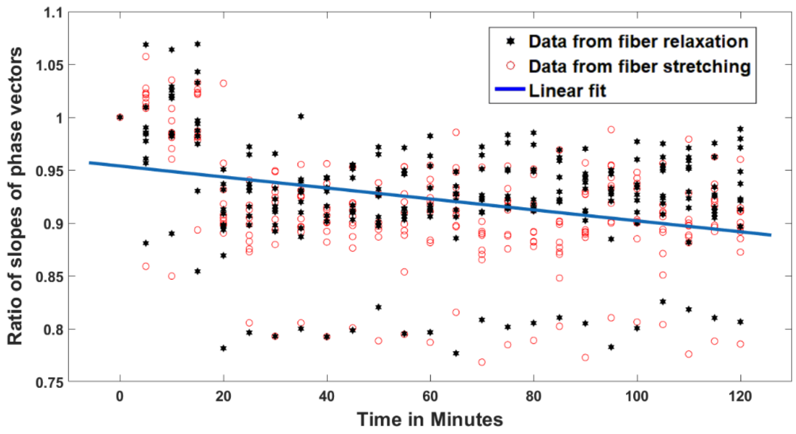

Figure 4-9: Sensor's phase change obtained using the spectral fringes

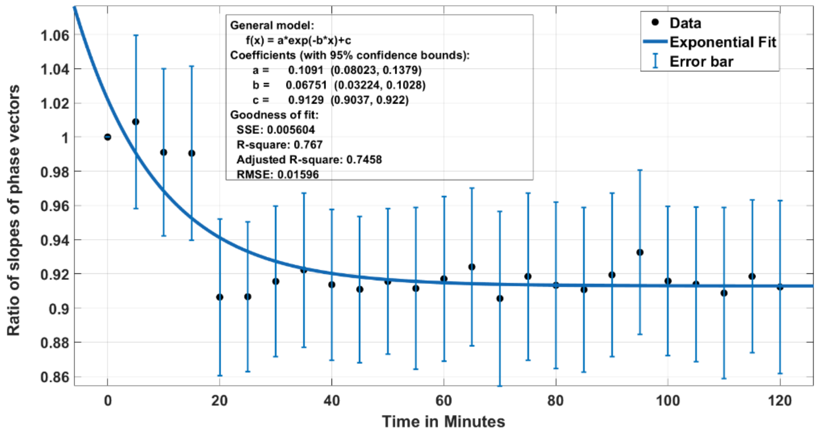

Figure 4-10: Median of sensor's phase change values plotted in Figure 4-9

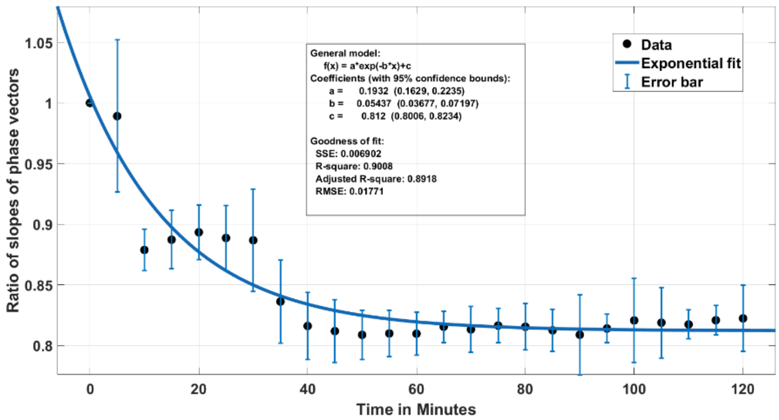

Figure 4-11: Sensor response calculated using the spectral fringes from the second trial

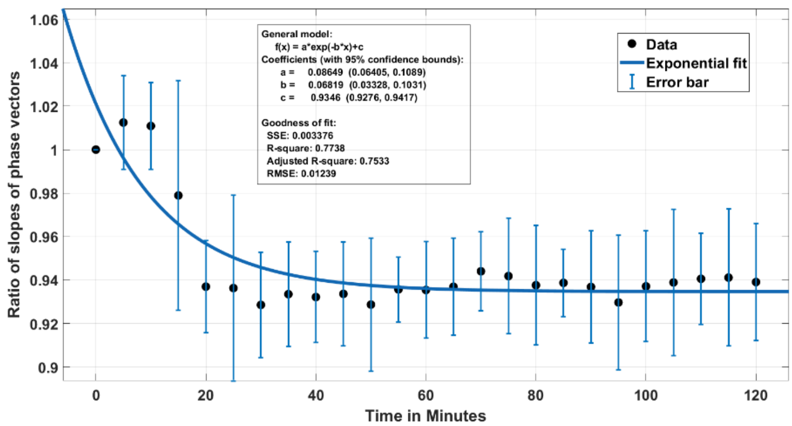

Figure 4-12: Sensor response calculated using the spectral fringes from the third trial

Sensor phase estimation using temporal fringes

In the second approach, the sensor's phase changes are directly calculated from their delay calibrated interferometric signals and an average frequency for the sensor's spectrum is obtained. Temporal phase vectors of the tapered sensor and the reference FBG are obtained from their respective recalibrated interferograms using Equation (2-87). Figure 4-13 shows a sample plot of the phase vectors.

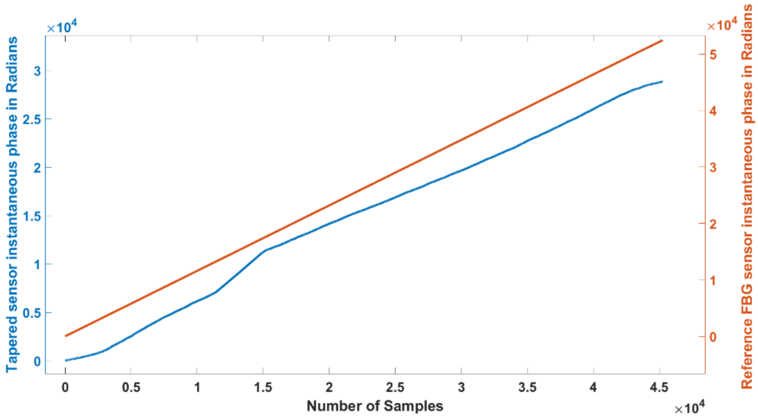

Figure 4-13: Plot of phase vector samples

For sensor response estimation using the temporal fringes, the phase vectors of all the 500 recalibrated reference FBG interferograms and the 500 recalibrated tapered sensor interferograms are obtained. Changes in the sensor's phase are computed by calculating the ratio of; the slopes of the reference FBG phase vectors and the slopes of the corresponding tapered sensor phase vectors. Figure 4-14 shows the sensor's response calculated as discussed above. It should be noted that the ratio between slopes (~1.7) is somewhat higher than expected (~1) based on the average wavelengths of taper and FBG. This discrepancy may be due to detection nonlinearities or spurious signals but should not affect the overall trends. A linear fit to the data shows an increasing trend in sensor's phase due to rising ethanol vapour concentration with the passage of time. This trend is the opposite direction to that observed in the previous section, possibly because in the previous case, the measurements were based on the TS's FSR (in terms of frequency), while in this case, tapered sensor’s average wavelength is being measured.

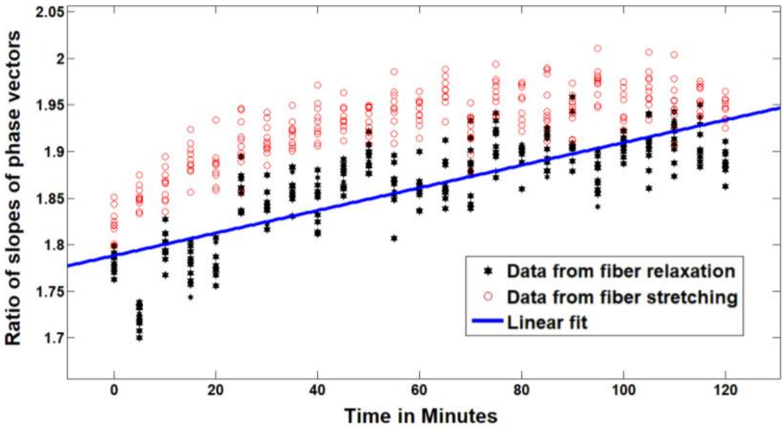

Figure 4-14: Plot of Sensor's phase change obtained using the temporal fringes
NB: Unlike in Figure 4-10, where all the sensor data points were divided by the first sensor data (as ref), in the above figure, slopes of the Ref FBG phase vectors were divided by the slopes of tapered sensor phase vectors. Hence the higher values when compared to Figure 4-10

Unfortunately, as is visible from Figure 4-14, this data processing technique results in a significant deviation between the results for stretching and relaxation of the stretcher, possibly due to less tolerance of the method to non-uniform OPD. Hence, only the data corresponding to the stretching of the fibre is considered. Median values of the stretching data sets seen in Figure 4-14 are plotted as a function of time. An exponential fit to the sensor data demonstrates the exponential change in sensor phase with changing ethanol concentration. The plot of the sensor data with the fitted exponential function and error bars is shown in Figure 4-15. From the exponential fit, the rate of sensor phase change is seen to be ~(36±10)e-3/min. Sensor responses from two other such trials have been shown in Figure 4-16 and Figure 4-17. The larger uncertainty value in the third trial is perhaps due to the abnormal data at the 25th

minute that can be seen in Figure 4-17. This abnormal data could possibly be attributed to the abnormal working of the stretcher.

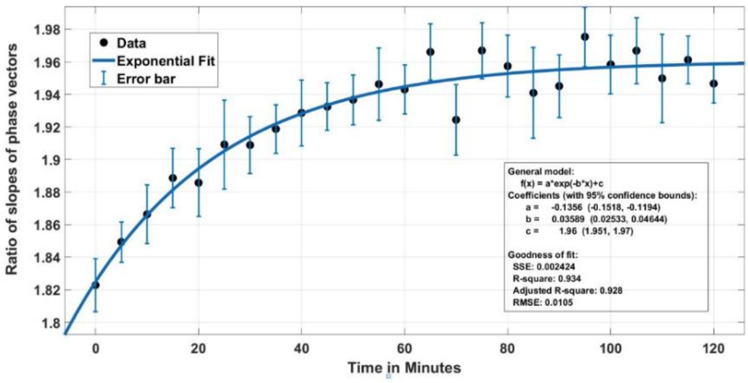

Figure 4-15: Plot of tapered sensor phase change data vs. Time

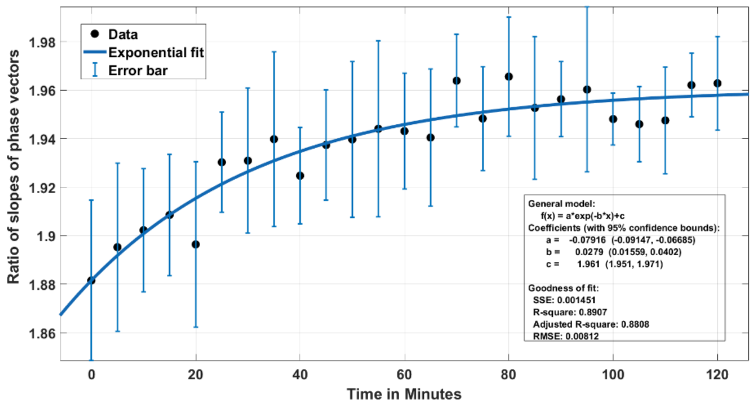

Figure 4-16: Sensor response calculated using the temporal fringes from the second trial

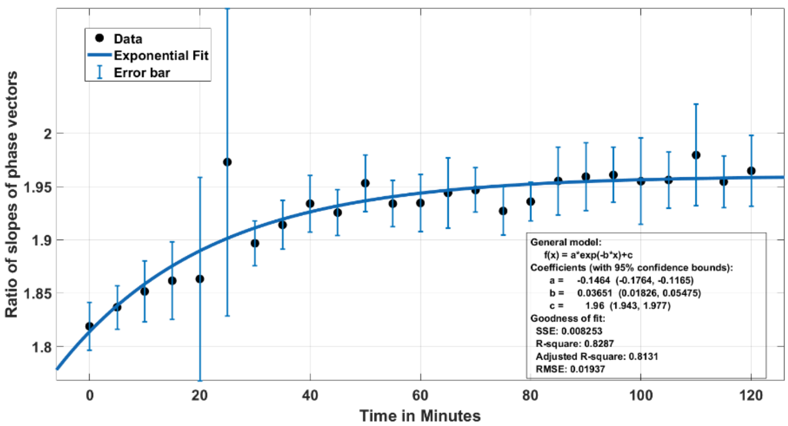

Figure 4-17: Sensor response calculated using the temporal fringes from the third trial

Measurement results obtained using the spectral fringes and the temporal fringes from multiple trials have been tabulated in Table 4-1.

Table 4-1: Tapered sensor data results

Trial Number	**Rate of the exponential phase change (/min)**	
	Spectral fringes	**Temporal fringes**
1	67±35e-3	36±10e-3
2	54±18e-3	28±12e-3
3	68±35e-3	36±18e-3

Sensor recovery after ethanol sensing

To demonstrate the reusability of the tapered sensors for ethanol sensing, a prolonged test was conducted beyond the 120 minutes previously discussed. In this case, the tapered sensors were used for sensing ethanol for 145 minutes after which the ethanol source was removed. In addition to the ethanol sensing experimental data, a set of interferometric data was recorded prior to the start of the ethanol sensing experiment and another set was recorded after a brief period of 30 minutes post the sensing experiment.

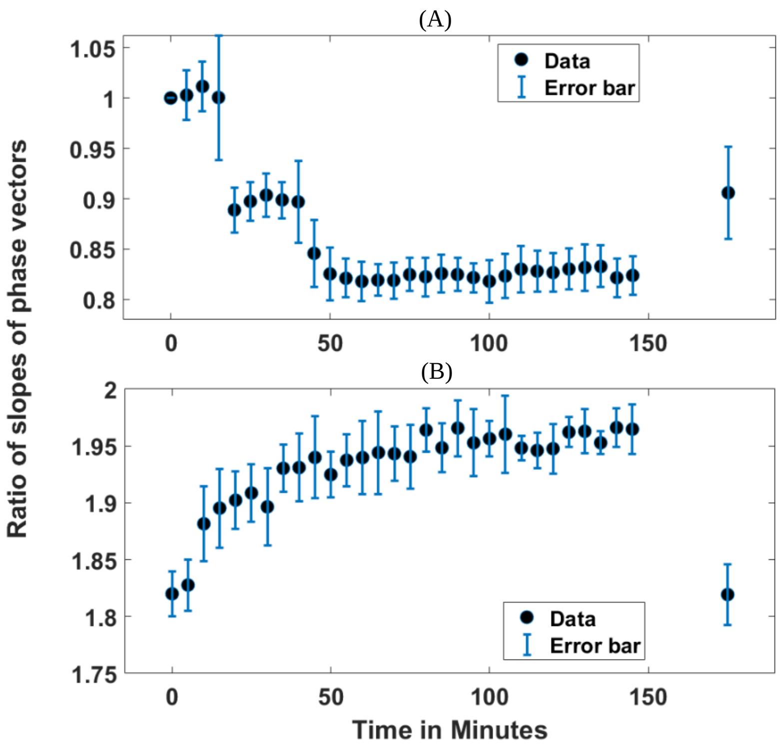

Figure 4-18: Plots of the sensor's phase change demonstrating the sensor's recovery

Figure 4-18, (A) and (B) show the plots of the tapered sensor's phase changes with error bars at various stages of the ethanol sensing experiment calculated using the spectral fringes and temporal fringes, respectively. The gap between the 145th minute data and the 175th minute data corresponds to the 30 minute break /cool-off period. Data at the 0th minute and 175th minute correspond to tapered sensor's phase value before and after the ethanol sensing experiment, respectively. From the above figure, the sensor response calculated using the temporal fringes is evidently more accurate as the sensor is seen to recover to its initial state after the conclusion of the ethanol sensing experiment. On the other hand, the data from the processing of the spectral fringes is seen to be less accurate with the 175th minute data not reverting to its initial state. The reason for this anomaly and the other results are discussed in the following section.

4.5 Discussion

In the previous experimental chapter, the interferometric data was sampled at 60kHz due to the 200kHz aggregate sampling frequency limitation of the DAQ unit. In this experimental chapter and the subsequent chapters, a faster DAQ has been employed, permitting the 100kHz sampling rate used.

As the spectral fringes were segmented for the phase change estimation thereby using only a section of the interferometric scan, the data from fibre stretching and relaxing interferograms had a negligible difference. The temporal fringe based sensor response estimation utilises the full length of the interferometric scan, and as a result, the effect of lash back of the stretched fibre during the relaxation is more profound. This results in large deviations from the values obtained using the stretching phase of the fibre stretcher.

The average % of the uncertainty values from the measurements obtained using the spectral fringes was calculated to be ~47% and the average % of the uncertainty values from the measurements obtained using the temporal fringes was calculated to be ~40%. Thus, the temporal fringe based measurement method was found to yield ~15% accuracy measurements when compared to the spectral fringe based measurements.

Unlike the temporal fringe based method where the referencing is done using the FBG data from the same time domain, in the spectral fringe based sensor response estimation method, scans from different time domains are compared. The fibre stretcher is an open loop system with no feedback mechanism. As a result, there is a scope for minor variations in the OPD between the scans from different times. Hence, comparison of data from different time domains implies comparison of data from different or dissimilar OPDs. Thus, the reduced accuracy with the spectral fringe based sensor response estimation can be attributed to the technique of comparing scans from different time domains.

To ascertain the above reasoning, ratio of; the slopes of the temporal phase vectors of reference FBG and the slopes of spectral fringe phase vectors from the same time domain were calculated and plotted as seen in Figure 4-19. In the figure, the 175th minute sensor value can be seen to revert to its initial value post the ethanol sensing experiment. Thus, the sensor response estimation using the spectral fringes is seen to work with lesser accuracy than the temporal fringe based sensor response estimation.

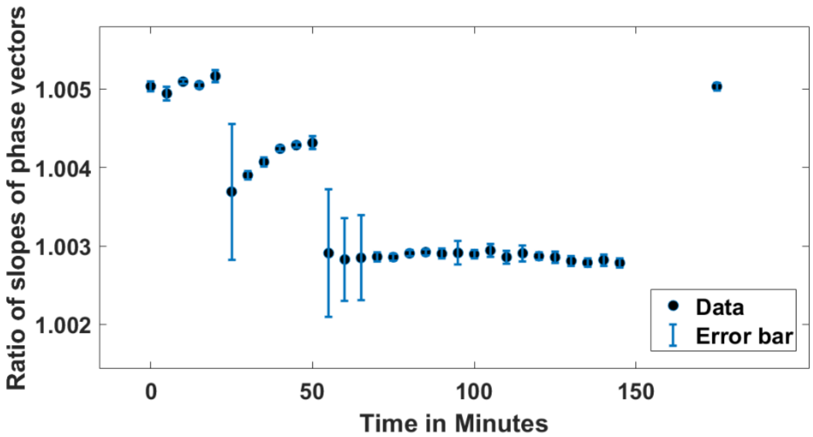

Figure 4-19: Slope of reference FBG temporal phase vector vs slope of spectral fringe phase vector

4.6 Conclusion

In this work, interferometric illumination of a tapered sensor and short-scan interferometry have demonstrated detection of ethanol vapour/gas. The results obtained by processing the sensor's temporal fringes have been found to be repeatable with three trials yielding similar detection rates of ~(36±10)e-3/min, ~(28±12)e-3/min and ~(36±18)e-3/min. The measurement accuracy obtained using the temporal fringes were found to be ~15% better than the ones obtained by processing the sensor's spectral fringes (typical measurement method using an OSA) ~(67±35)e-3/min, ~(54±18)e-3/min and ~(68±35)e-3/min.

Unlike certain dye based sensors [34] and sensors with special coatings [35], [36] used for gas sensing and ethanol sensing [37], that require heating or other treatments for sensor desorption and re-use, the label-free tapered sensor used in this study was shown to recover automatically to its initial state upon the removal of the stimulus. However, to accurately determine the exact response and recovery time, further dynamic studies have to be conducted as performed by Rosli *et al.* [38] and Shabaneh *et al.* [39].

The free spectral range of the sensor used in this work was ~8nm. The effect of sensor's FSR and the measurement sensitivity has been previously reported [23]. It is well known that in FTS, the system resolution is dependent on the scan length. Thus, the system resolution can be further improved by increasing the scan length and the sensitivity of the sensor can be improved by using a sensor with reduced FSR.

In the next chapter, by expanding on the interrogation system used in this experiment, the simultaneous interrogation of multiple tapered sensors is presented. This demonstrates the capability and efficacy of the interferometric illumination system to interrogate multiple tapered sensors in a single scan, thereby overcoming the limitations of the conventional schemes.

4.7 References

[1] B. H. Lee *et al.*, 'Interferometric Fiber Optic Sensors', *Sensors*, vol. 12, no. 12, pp. 2467–2486, Feb. 2012, doi: 10.3390/s120302467.

[2] P. Lu, L. Men, K. Sooley, and Q. Chen, 'Tapered fiber Mach–Zehnder interferometer for simultaneous measurement of refractive index and temperature', *Applied Physics Letters*, vol. 94, no. 13, p. 131110, Mar. 2009, doi: 10.1063/1.3115029.

[3] P. Wang, H. Zhao, X. Wang, G. Farrell, and G. Brambilla, 'A Review of Multimode Interference in Tapered Optical Fibers and Related Applications', *Sensors*, vol. 18, no. 3, p. 858, Mar. 2018, doi: 10.3390/s18030858.

[4] K. Q. Kieu and M. Mansuripur, 'Biconical Fiber Taper Sensors', *IEEE Photonics Technology Letters*, vol. 18, no. 21, pp. 2239–2241, Nov. 2006, doi: 10.1109/LPT.2006.884742.

[5] Y. Tian, W. Wang, N. Wu, X. Zou, and X. Wang, 'Tapered Optical Fiber Sensor for Label-Free Detection of Biomolecules', *Sensors*, vol. 11, no. 12, pp. 3780–3790, Mar. 2011, doi: 10.3390/s110403780.

[6] S. W. Harun, K. S. Lim, C. K. Tio, K. Dimyati, and H. Ahmad, 'Theoretical analysis and fabrication of tapered fiber', *Optik - International Journal for Light and Electron Optics*, vol. 124, no. 6, pp. 538–543, Mar. 2013, doi: 10.1016/j.ijleo.2011.12.054.

[7] J. Miller *et al.*, 'Biconically Tapered Fiber Optic Probes for Rapid Label-Free Immunoassays', *Biosensors*, vol. 5, no. 2, pp. 158–171, Apr. 2015, doi: 10.3390/bios5020158.

[8] S. H. Girei, A. A. Shabaneh, P. T. Arasu, S. Painam, and M. H. Yaacob, ‘Tapered multimode fiber sensor for ethanol sensing application’, in *2013 IEEE 4th International Conference on Photonics (ICP)*, Melaka, Malaysia, Oct. 2013, pp. 275–277, doi: 10.1109/ICP.2013.6687137.

[9] P. Fellgett, ‘Spectromètre interférentiel multiplex pour mesures infra-rouges sur les étoiles’, *Journal de Physique et le Radium*, vol. 19, no. 3, pp. 237–240, 1958, doi: 10.1051/jphysrad:01958001903023700.

[10] P. Jacquinot, ‘New developments in interference spectroscopy’, *Reports on Progress in Physics*, vol. 23, no. 1, p. 267, 1960.

[11] J. Connes and P. Connes, ‘Near-Infrared Planetary Spectra by Fourier Spectroscopy. I. Instruments and Results’, *J. Opt. Soc. Am.*, vol. 56, no. 7, pp. 896–910, Jul. 1966, doi: 10.1364/JOSA.56.000896.

[12] D. A. Flavin, R. McBride, and J. D. C. Jones, ‘Short-scan interferometric interrogation and multiplexing of fibre Bragg grating sensors’, *Optics Communications*, vol. 170, no. 4–6, pp. 347–353, Nov. 1999, doi: 10.1016/S0030-4018(99)00515-5.

[13] K. T. O’Mahoney, R. P. O’Byrne, S. V. Sergeyev, Lin Zhang, and I. Bennion, ‘Short-Scan Fiber Interferometer for High-Resolution Bragg Grating Array Interrogation’, *IEEE Sensors Journal*, vol. 9, no. 10, pp. 1277–1281, Oct. 2009, doi: 10.1109/JSEN.2009.2029818.

[14] Y. L. Hoo, W. Jin, H. L. Ho, D. N. Wang, and R. S. Windele, ‘Evanescent wave gas sensing using microstructure fibre’, 2001, pp. 8–9, doi: 10.1109/CLEOPR.2001.968008.

[15] C. Consani, C. Ranacher, A. Tortschanoff, T. Grille, P. Irsigler, and B. Jakoby, 'Evanescent-Wave Gas Sensing Using an Integrated Thermal Light Source', *Proceedings*, vol. 1, no. 4, p. 550, Aug. 2017, doi: 10.3390/proceedings1040550.

[16] H. Tai, T. Yoshino, and H. Tanaka, 'Fiber-optic evanescent-wave methane-gas sensor using optical absorption for the 3392-μm line of a He–Ne laser', *Optics Letters*, vol. 12, no. 6, p. 437, Jun. 1987, doi: 10.1364/OL.12.000437.

[17] R. Siebert and J. Müller, 'Infrared integrated optical evanescent field sensor for gas analysis', *Sensors and Actuators A: Physical*, vol. 119, no. 1, pp. 138–149, Mar. 2005, doi: 10.1016/j.sna.2004.11.001.

[18] G. Stewart, F. A. Muhammad, and B. Culshaw, 'Sensitivity improvement for evanescent-wave gas sensors', *Sensors and Actuators B: Chemical*, vol. 11, no. 1–3, pp. 521–524, Mar. 1993, doi: 10.1016/0925-4005(93)85297-N.

[19] S. Sekimoto *et al.*, 'A fiber-optic evanescent-wave hydrogen gas sensor using palladium-supported tungsten oxide', *Sensors and Actuators B: Chemical*, vol. 66, no. 1–3, pp. 142–145, Jul. 2000, doi: 10.1016/S0925-4005(00)00330-0.

[20] M. Morisawa, Y. Amemiya, H. Kohzu, C. X. Liang, and S. Muto, 'Plastic optical fibre sensor for detecting vapour phase alcohol', *Measurement Science and Technology*, vol. 12, no. 7, pp. 877–881, Jun. 2001, doi: 10.1088/0957-0233/12/7/322.

[21] D. Liu *et al.*, ‘High sensitivity optical fiber sensors for simultaneous measurement of methanol and ethanol’, *Sensors and Actuators B: Chemical*, vol. 271, pp. 1–8, Oct. 2018, doi: 10.1016/j.snb.2018.05.106.

[22] A. Grazia, M. Riccardo, and F. L. Ciaccheri, ‘Evanescent Wave Absorption Spectroscopy by Means of Bi-tapered Multimode Optical Fibers’, *Appl. Spectrosc.*, vol. 52, no. 4, pp. 546–551, Apr. 1998.

[23] M. Z. Muhammad, A. A. Jasim, H. Ahmad, H. Arof, and S. W. Harun, ‘Non-adiabatic silica microfiber for strain and temperature sensors’, *Sensors and Actuators A: Physical*, vol. 192, pp. 130–132, Apr. 2013, doi: 10.1016/j.sna.2012.12.036.

[24] S. Ravets, J. E. Hoffman, P. R. Kordell, J. D. Wong-Campos, S. L. Rolston, and L. A. Orozco, ‘Intermodal energy transfer in a tapered optical fiber: optimizing transmission’, *Journal of the Optical Society of America A*, vol. 30, no. 11, p. 2361, Nov. 2013, doi: 10.1364/JOSAA.30.002361.

[25] L. V. Nguyen, D. Hwang, S. Moon, D. S. Moon, and Y. Chung, ‘High temperature fiber sensor with high sensitivity based on core diameter mismatch’, *Optics Express*, vol. 16, no. 15, p. 11369, Jul. 2008, doi: 10.1364/OE.16.011369.

[26] Niederlande, Ed., *Methods for the calculation of physical effects: due to releases of hazardous materials (liquids and gases) ; ‘yellow book’*, 3rd ed. Den Haag: Sdu Uitgevers, 1997.

[27] G. Wm. Thomson, ‘The Antoine Equation for Vapor-pressure Data.’, *Chemical Reviews*, vol. 38, no. 1, pp. 1–39, Feb. 1946, doi: 10.1021/cr60119a001.

[28] M. Talibov and J. Safarov, ‘Vapour Pressure of Ethanol and 1-Propanol Binary Mixtures’, *Hungarian Journal of Industry and Chemistry*, vol. 44, no. 1, pp. 33–38, Oct. 2016, doi: 10.1515/hjic-2016-0004.

[29] A. D. Kersey, M. J. Marrone, and M. A. Davis, ‘Polarisation-insensitive fibre optic Michelson interferometer’, *Electronics Letters*, vol. 27, no. 6, p. 518, 1991, doi: 10.1049/el:19910325.

[30] H. Nyquist, ‘Certain Topics in Telegraph Transmission Theory’, *Trans. Am. Inst. Electr. Eng.*, vol. 47, no. 2, pp. 617–644, Apr. 1928, doi: 10.1109/T-AIEE.1928.5055024.

[31] M. Konstantaki, A. Klini, D. Anglos, and S. Pissadakis, ‘An ethanol vapor detection probe based on a ZnO nanorod coated optical fiber long period grating’, *Optics Express*, vol. 20, no. 8, p. 8472, Apr. 2012, doi: 10.1364/OE.20.008472.

[32] H. Saad, M. T. Ali, and M. K. Abd Rahman, ‘High Sensitivity Optical POF Sensor for Detecting Low Ethanol Concentration in Water’, *Advanced Materials Research*, vol. 1107, pp. 693–698, Jun. 2015, doi: 10.4028/www.scientific.net/AMR.1107.693.

[33] J. Linesh, ‘Design and Development of Fiber Optic Sensors for Quality Evaluation of various Liquid and Gaseous Media’, 2013.

[34] C.-S. Chu and M.-W. Hsieh, ‘Optical carbon dioxide sensor based on the colorimetric change of α-naphtholphthalein and internal reference fluorescent CIS/ZnS QDs’, Apr. 2017, doi: 10.1117/12.2255810.

[35] J.-W. Wu and C.-C. Chiang, ‘Notched Long-Period Fiber Grating with an Amine-Modified Surface Nanostructure for Carbon Dioxide Gas Sensing’, *Materials*, vol. 8, no. 7, pp. 4535–4543, Jul. 2015, doi: 10.3390/ma8074535.

[36] C. Gouveia, A. Markovics, J. M. Baptista, B. Kovacs, and P. A. S. Jorge, ‘Measurement of CO2 Using Refractometric Fiber Optic Sensors’, in *Proceedings of the 3rd WSEAS International Conference on Advances in Sensors, Signals and Materials*, Stevens Point, Wisconsin, USA, 2010, pp. 169–173, [Online]. Available: http://dl.acm.org/citation.cfm?id=1950175.1950209.

[37] L. R. Shobin, B. Renganathan, D. Sastikumar, K. C. Park, and S. Manivannan, ‘Pure and Iso-Butyl Methyl Ketone Treated Multi-Walled Carbon Nanotubes for Ethanol and Methanol Vapor Sensing’, *IEEE Sensors J.*, vol. 14, no. 4, pp. 1238–1243, Apr. 2014, doi: 10.1109/JSEN.2013.2294361.

[38] M. A. A. Rosli, P. T. Arasu, H. N. Lim, and A. S. M. Noor, ‘Dynamic response of tapered optical fiber coated with graphene oxide for detecting aqueous ethanol’, in *2016 IEEE 6th International Conference on Photonics (ICP)*, Kuching, Sarawak, Malaysia, Mar. 2016, pp. 1–3, doi: 10.1109/ICP.2016.7510029.

[39] A. A. Shabaneh *et al.*, ‘Reflectance Response of Optical Fiber Coated With Carbon Nanotubes for Aqueous Ethanol Sensing’, *IEEE Photonics J.*, vol. 6, no. 6, pp. 1–10, Dec. 2014, doi: 10.1109/JPHOT.2014.2363429.

Chapter 5

Simultaneous Interrogation of Multiple Tapered Fibre Optic Sensors by Interferometric Illumination

5.1 Introduction

A conventional approach to simultaneous interrogation of multiple tapered fiber optic sensors would involve a tunable laser, beam splitter and multiple detectors each one monitoring a different sensor. This chapter investigates the capability and efficacy of a novel and potentially a low cost approach to interrogate multiple tapered sensors simultaneously using a single interferometer. Interrogation by this unique approach of first illuminating the sensors with the source's broadband interferogram will facilitate the sensors' interrogation with equal and high resolution of the interferometer.

The optical fibres in which the light guided within is modulated in response to an external physical, chemical, biological or any other such stimulus are called fibre optic sensors. The tapered sensor is a type of fibre optic interferometric sensor (FOIS) with a section of reduced diameter [1]. Based on evanescent wave sensing, tapered sensors have been primarily used for refractive index based sensing applications such as bio-sensing [2]–[4], gas sensing [5]–[7], etc., whilst being interrogated using optical spectrum analysers (OSA), spectrometers and optical power meters [2], [3], [8]–[10].

The tapered sensors take up the entire bandwidth of the illuminating source spectrum and as a result, sensor multiplexing would result in a spectral overlap. An OSA and even existing interferometer [11]–[14] based interrogation schemes do not permit simultaneous interrogation of multiple tapered sensors due to this characteristic of the sensor.

Using a novel approach to interferometrically interrogate tapered sensors, this work investigates the capability and efficacy of an all-fibre interrogation system to interrogate multiple tapered fibre optic sensors (TFOS) in a single interferometric scan. An all-fibre Michelson interferometer scanning through an optical path difference (OPD) of ~13mm generated a broadband interferogram and the generated broadband interferogram was then used to illuminate the reference fibre Bragg grating (FBG) and the measurement tapered sensors. Dedicated photodiodes for the sensors prevented the spectral overlap of sensors.

Even with the conventional methods using a broadband source, by using couplers, multiple sensors can be independently illuminated, but sensors' demodulation requires as many OSAs/spectrometers as the sensors due to the nature of the sensor itself. In the experiment demonstrated in this chapter, only one interrogation unit is used with multiple photodiodes which is a more cost effective solution than using multiple OSAs/spectrometers. The key characteristic of this interrogation system is its ease of scalability. This experiment demonstrates the simultaneous interrogation of two sensors; however, the sensor capacity can be increased several times.

To ascertain the interrogation capabilities of the system, the tapered sensors were used to sense refractive index changes caused by the addition of various concentrations of glucose solutions to a bath and the changes to the refractive index of air surrounding the tapered sensors caused by ethanol evaporating at room temperature. The rate of change in the phase of sensors caused by the addition of glucose solutions was found to be ~(3.0±1.4)e-7/ppm for the first tapered sensor and

and ~(5.2±2.3)e-7/ppm for the other tapered sensor. Ethanol evaporating at room temperature was found to change the sensors' phase exponentially by ~(26±12)e-3/min and ~(29±10)e-3/min for sensor 1 and sensor 2, respectively.

5.2 Theory

Tapered fibre

The theory behind the working of the tapered sensors based on modal interference for sensing applications has been dealt with at great length in the previous experimental chapter. However, when a non-adiabatic tapered sensor is immersed in a liquid medium whose refractive index is close to that of the air-cladding interface, the higher order modes tend to escape into the external medium resulting in very little or no interference with the fundamental mode at the transition region, resulting in reduced spectral fringe visibility. Under such circumstances, evanescent wave power is monitored in addition to the phase difference between the modes.

In accordance with Maxwell's equations and the boundary conditions, though all the light is contained within the core of the fibre due to total internal reflection, still there will be a disturbance or a wave extending beyond the core of the fibre. This wave in the second medium is called the evanescent wave. Evanescent wave's intensity decays exponentially with increasing distance from the core-cladding interface as given by the following equation [15].

$$E_x = E_0 e^{-\frac{x}{d_p}} \tag{5-1}$$

In Equation (5-1), E_0 is the intensity of the incident light, x is the distance from the core-cladding interface and d_p is the penetration depth. For the derivation of the evanescent wave decay, the reader is referred to Section 2.9.3 of Chapter-2 of this document. Due to effects like scattering and absorption, the evanescent field power will vary based on its interaction with the external environment. By measuring the evanescent field power loss across the tapered region, information about the external environment can be inferred.

A fibre's sensitivity to the environment depends on the penetration depth which is given by [16],

$$d_p = \frac{\lambda}{2\pi\sqrt{n_1^2 \, sin^2\,\theta - n_2^2}} \tag{5-2}$$

where n_1, n_2 are refractive indices of core and cladding respectively, λ is the central wavelength of source and θ is the angle of the ray with the normal to the core-cladding interface. When the sensor is surrounded by a liquid medium, the exposed evanescent waves interact freely with the medium surrounding the sensor. This property of the tapered sensor and evanescent wave based sensing is exploited in this experimental chapter to compute the TSs' response. On the other hand, in a gaseous environment like the ethanol sensing experiment discussed in the previous chapter, the reduced penetration depth of the evanescent waves results in its sparse interaction with the medium surrounding the sensor. And under such conditions, the modulation of the light by the sensor is primarily based on the interaction of the cladding modes with the medium around the sensor.

The interferogram processing techniques for sensor response estimation has also been discussed previously in Chapters 3 and 4. This chapter employs ethanol vapours and glucose solutions for demonstrating the efficacy of the interrogation system to simultaneously interrogate multiple tapered sensors in a single interferometric scan. As the theory behind the ethanol vapour sensing has already been covered in Chapter-4, only the theory pertaining to glucose sensing is presented below.

Glucose Sensing

The refractive index of the glucose solution is directly proportional to its concentration. The relation between the glucose solution's refractive index and concentration is given by [17],

$$n = n_w + 0.00143 * C \tag{5-3}$$

In Equation (5-3), n is the refractive index of the glucose solution, n_w is the refractive index of deionised water, which is ~1.3179 and C is the concentration of glucose in gm/100ml unit. The Equation (5-3) is of the form $y = mx + c$ and as a result, if the refractive index values are plotted against the glucose concentration values, the resultant plot will be a straight line with a slope of ~1.43e-3.

With changing glucose concentrations, the refractive index also changes proportionally. The refractive index changes of the glucose solution induce changes to the tapered sensor's spectrum. Hence, in this chapter, to demonstrate the efficacy of the interferometric illumination method to simultaneously interrogate multiple tapered sensors in a liquid medium, glucose solutions with varying concentrations are used as the sensor stimulants.

5.3 Experimental setup

The experimental setup used in this work is shown in Figure 5-1. The interferometer is an unbalanced all-fibre Michelson interferometer in which an OPD of ~13mm is generated by the piezo fibre stretcher (PFS) (Evanescent Optics, Fibre Stretcher, Model 916B), when modulated with 1Hz sine wave with a 5V DC offset.

The fibre interferometer implemented using a single mode fibre is prone to variations in fringe visibility and fading of the interferometric signal due to random changes to the state of polarization (SOP) of the interfering optical beams. Faraday rotator components have been previously shown to reduce the fading of the interferometric signal due to changes in the SOP [18], [19]. Hence, in the experimental setup, Faraday rotator mirrors FRM1 and FRM2 are used to reduce polarization induced fading in the fibre. The circulator (C) directs the light from a broadband source (BBS) with a centre wavelength of 1550nm into the interferometer, and the interferogram generated by the interferometer towards the sensors. The directional coupler DC1 is used to illuminate the arms of the interferometer. Isolators I1, I2, and I3 prevent back reflections from coupling into other sensor arrays.

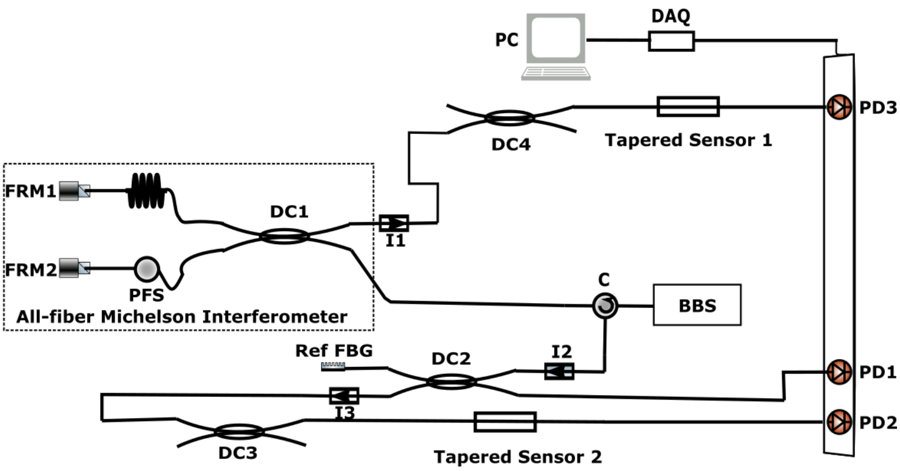

Figure 5-1: Experimental setup

The photodiodes PD1, PD2 and PD3 (Newfocus 2053) are used to convert the light reflected by reference fibre Bragg grating (FBG) and the light transmitted through TFOS into electrical signals. A high-speed data acquisition card (DAQ) (NI-USB-6341) was used to record the analogue signals from the photodiode on to a computer. Ref FBG with a full width at half maximum of ~ 0.19nm and a centre wavelength of ~1559nm has a coherence length of ~12.8mm. For the tests, 1M samples of interferometric signals were recorded at 100kHz such that, each fringe was sampled 4 times. The sensing capability of the system is evaluated by interrogating the tapered sensors whilst monitoring ethanol evaporation at room temperature and glucose solution's concentration changes.

Both the ethanol vapours and the glucose solutions induce varying levels of phase changes on the tapered sensors. In addition, they are in different media, i.e., the glucose solution is a liquid while ethanol vapour is a gas and as a result, the sensors' fringe visibility varies between the two stimuli. Thus, by using these stimuli and interrogating the tapered sensors, the dexterity of the sensing system is demonstrated. Due to the fragility of the sensors, different sets of sensors were used for glucose and ethanol sensing.

Ethanol sensing

The methodology used for sensing ethanol evaporation at room temperature has already been delineated in the Chapter-4. The previously demonstrated method of sensing ethanol using a single tapered fibre was extrapolated to the two sensors used in this experiment.

Glucose sensing

A fixed concentration of glucose solution induces a discrete change in the tapered sensors' phase. Hence for obtaining multiple data points/samples, glucose solutions with varying concentrations were used. D-Glucose-1 hydrate was dissolved in de-ionised water and equal volumes of 64%, 32%, 16%, 8%, 4% and 2% glucose solutions were prepared by serial dilution. Starting with the highest concentration, the solutions were sequentially added into a bath containing the sensors and data was logged after the addition of each solution.

5.4 Results

A single scan of the all-fibre interferometer generates a broadband interferogram of the source and the reference FBG when illuminated with the generated broadband interferogram, reflects a narrowband interferogram characteristic to it. The broadband interferogram generated is shown in Figure 5-2 (A) and interferogram reflected by the reference FBG can be seen in Figure 5-2 (B).

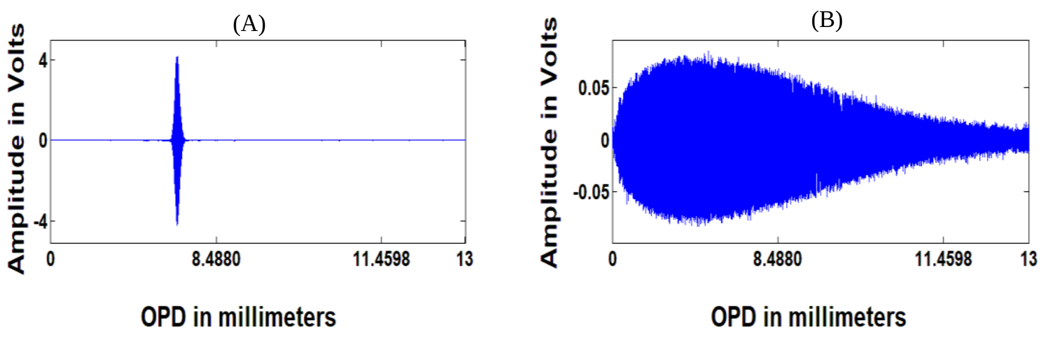

Figure 5-2: (A) - Source interferogram, (B) - Interferogram reflected by Ref FBG

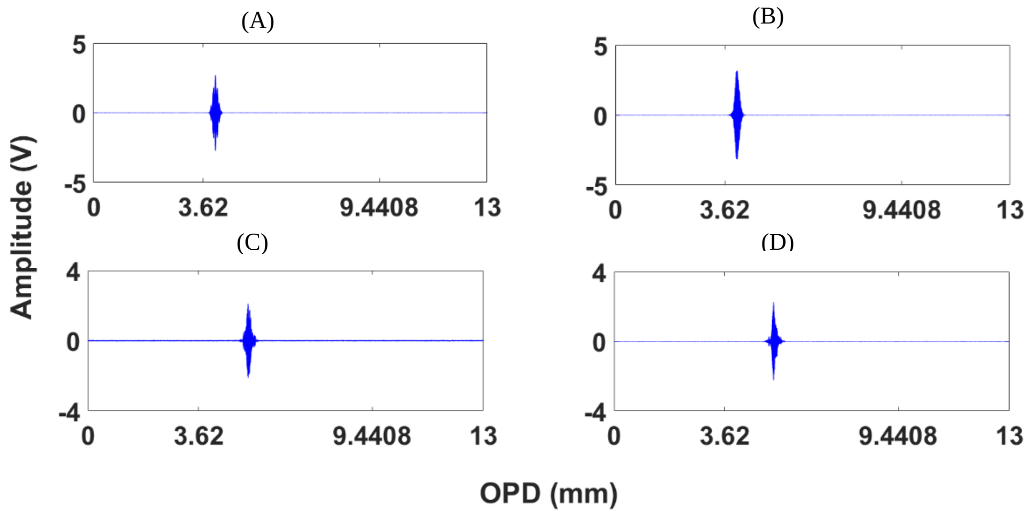

Figure 5-3: (A) - (B) - TS1 and TS2 used for glucose sensing, (C) - (D) - TS1 and TS2 used for ethanol sensing

Interferograms transmitted by the different tapered sensors used in the experiment are shown in Figure 5-3. In Figure 5-3, while (A) and (B) correspond to the interferograms transmitted through tapered sensors used to study the concentration changes of glucose solutions, (C) and (D) correspond to the interferograms transmitted through tapered sensors used to monitor the ethanol evaporation.

Due to the non-linear motion of the fibre stretcher and non-uniform OPD sampling, the Fourier transform of the reference and measurement interferograms results in additional spectral content as shown in Figure 5-4. For delay calibration, the analytic signal of the reference interferogram is first obtained by Hilbert transform processing. Subsequently, using the phase vector obtained from the analytic signal, the sensors are calibrated by simulation of uniform OPD sampling.

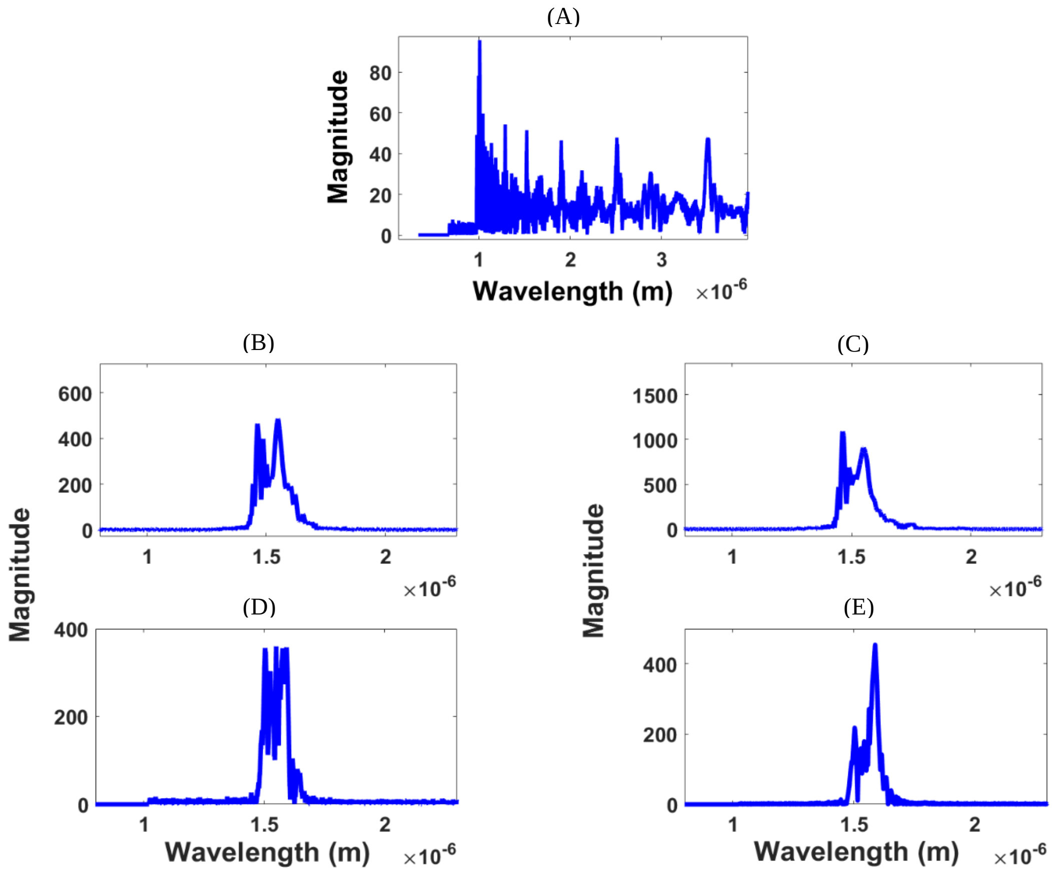

Figure 5-4: Uncalibrated spectra of (A) - Reference FBG (B) - (C) - TS1 and TS2 used for glucose sensing, (D) - (E) - TS1 and TS2 used for ethanol sensing

Upon calibration of the sensors using HTT [20], the reference FBG peak and the fringes of the tapered sensors become clearly visible. Fourier transform of the delay calibrated signals are shown in Figure 5-5.

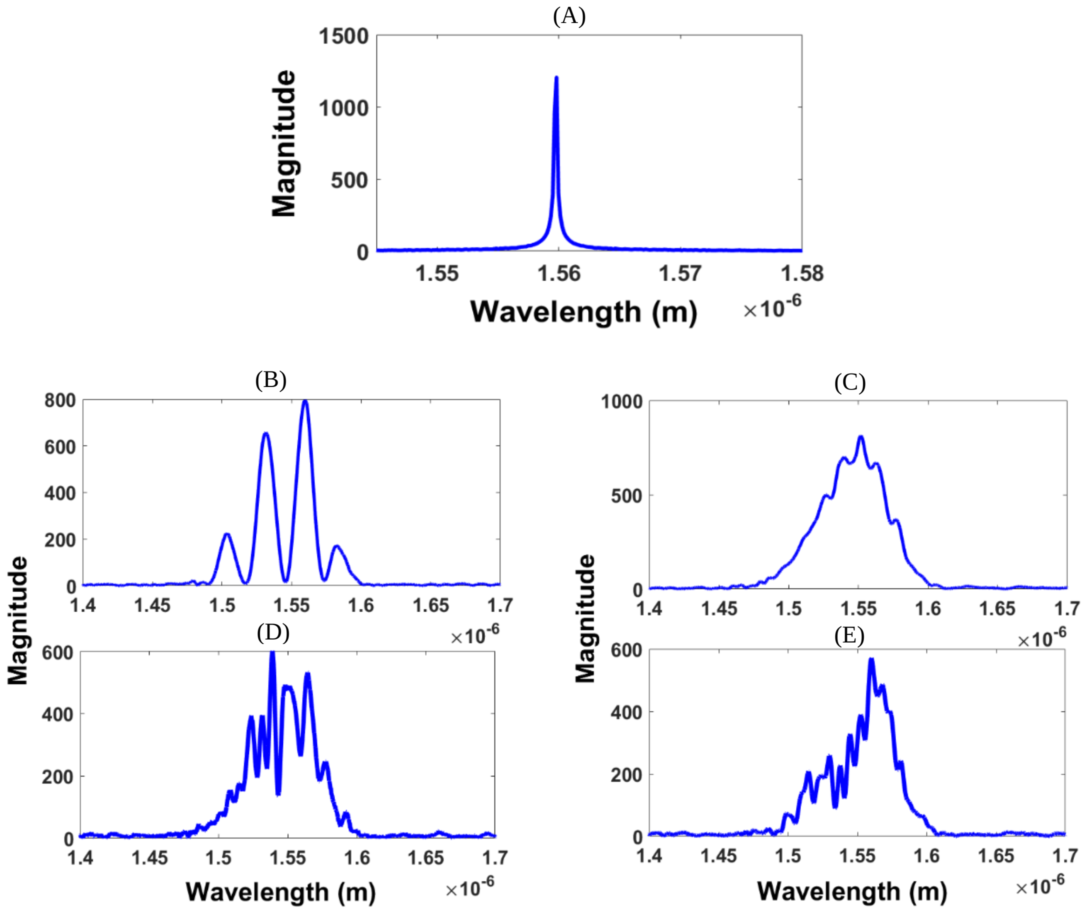

Figure 5-5: Recalibrated spectra of: (A) - Reference FBG interferogram, (B) - (C) – Bare TS1 and TS2 used for glucose sensing, (D) - (E) – Bare TS1 and TS2 used for ethanol sensing

The sensor spectra shown in Figure 5-4 and Figure 5-5 are spectra obtained prior to the experimentation process i.e., bare sensor spectra without the influence of ethanol or glucose. Ethanol vapour testing is done under a gaseous environment without any impact on the spectral fringe visibility. However, when the tapered sensor is immersed into a bath of liquid, the spectral visibility reduces as shown in the Figure 5-6. Hence, when the tapered sensor is immersed in a bath of glucose solution, the fringe visibility reduces. Figure 5-7 is a plot from the pilot study conducted on glucose sensing, in which the tapered sensor's spectral fringes are barely/minimally visible. It also shows the reduction in sensor's spectral intensity with increasing glucose concentration. The y-axis term "Magnitude" in Figure 5-4, Figure 5-5 and Figure 5-6 is in arbitrary units.

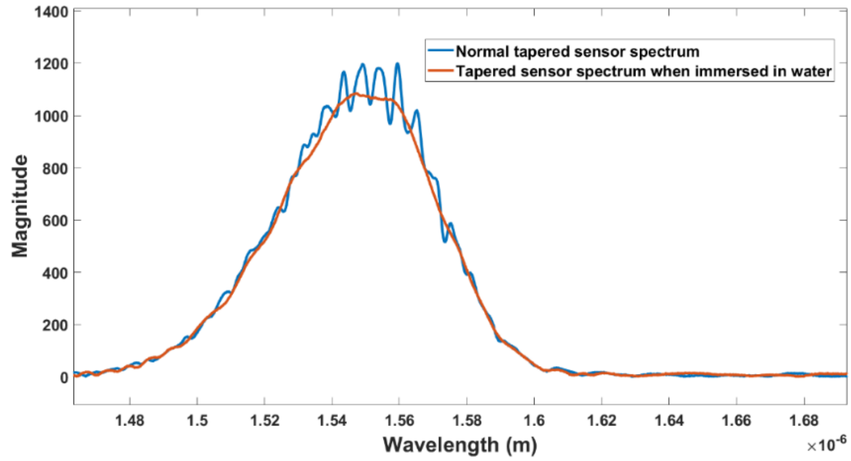

Figure 5-6: Plot of sensor spectrum surround by air and water

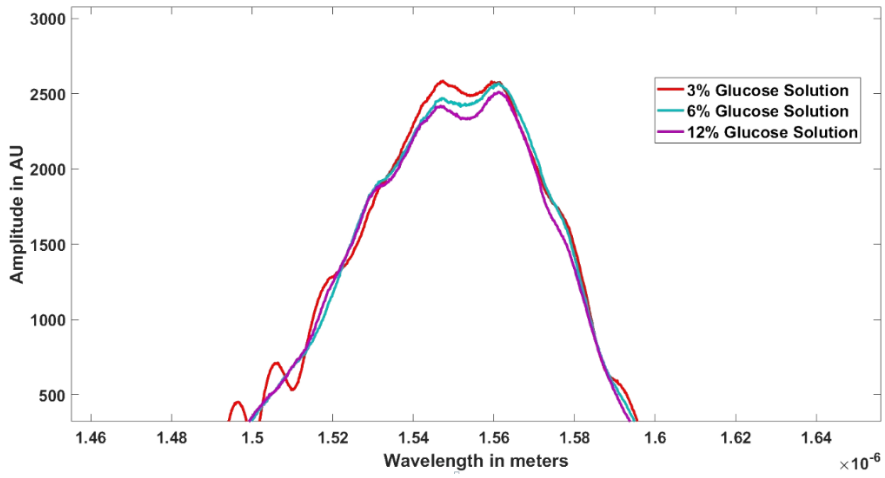

Figure 5-7: Reduction in tapered sensor fringe visibility when immersed in glucose solution

Use of the HTT directly on the recalibrated tapered sensor interferograms gives the average wavelength of the tapered sensor. If we measure the change in this quantity then, it should give us a quantity that is proportional to the refractive index change in the surrounding medium.

Ethanol Sensing

For the ethanol sensing experiment, the same test setup described in the last experimental chapter, Chapter-4 was extended to work with the second tapered sensor. 2ml of 98% ethyl alcohol was added to the petri dish and recording of interferometric signals was started. Interferometric signals were logged in 5-minute intervals for 120 minutes.

Change in the phase of the sensors is calculated by comparing the slopes of the reference FBG against their respective sensors' temporal phase vector slopes. Due to lash back effect of the fibre stretcher during the relaxation of the stretched fibre, only the interferograms resulting from the stretching of the fibre is used for phase calculations. Phase data of the sensors plotted as a function of time as shown in Figure 5-8.

An exponential fit to the sensors' phase data demonstrated the exponential phase change induced by increasing ethanol concentrations discussed in the previous chapter of this document. From the exponential fit equations, the rate of phase change with rising ethanol vapour concentration was calculated to be ~(26±12)e-3/min and ~(29±10)e-3/min for tapered sensors 1 and 2, respectively.

(A)

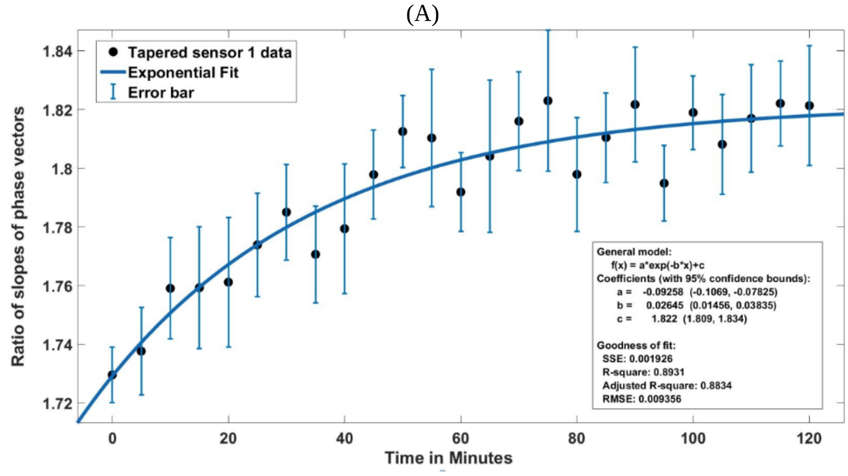

(B)

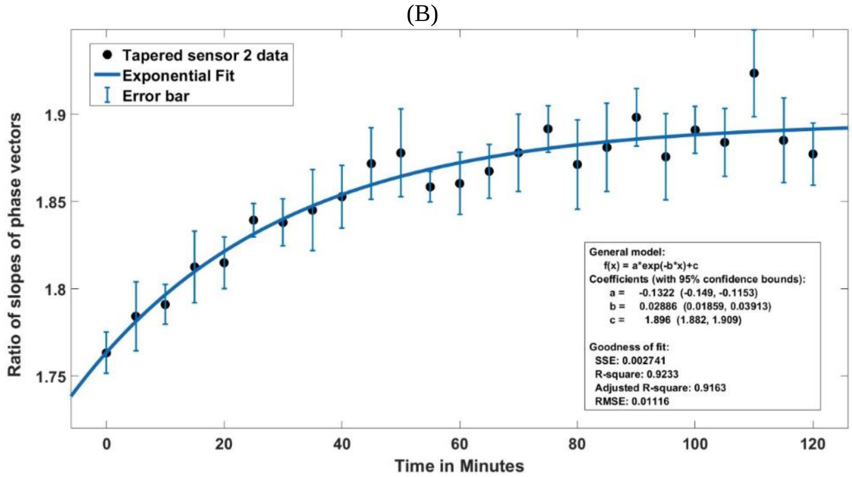

Figure 5-8: Plot of (A) - Tapered sensor 1 data, (B) - Tapered sensor 2 data for ethanol sensing experiment

Glucose Sensing

Equal volumes of 64%, 32%, 16%, 8%, 4% and 2% glucose solutions were prepared by serial dilution of D-Glucose-1 hydrate in de-ionised water. Net concentration of the solution in the bath changes upon the addition of each glucose solution sample. The order in which the glucose solutions were added to the bath (sample number) and the theoretical values of the nett concentration of the solution in the bath after the addition of each of the samples is given in Table 5-1. The addition of solutions by serial dilution to one another results in an overall change of concentration that varies cubically as shown in Figure 5-9 and Table 5-1. In Figure 5-9, the cubic fit demonstrates the cubic variation and the linear fit demonstrates a positive increase in concentration.

Table 5-1: Glucose solution samples and theoretical concentration

Sample Number	Glucose Solution Concentration	Theoretical Concentration of the solution in the Bath
1	2%	2%
2	4%	3%
3	8%	4.667%
4	16%	7.5%
5	32%	12.4%
6	64%	21%

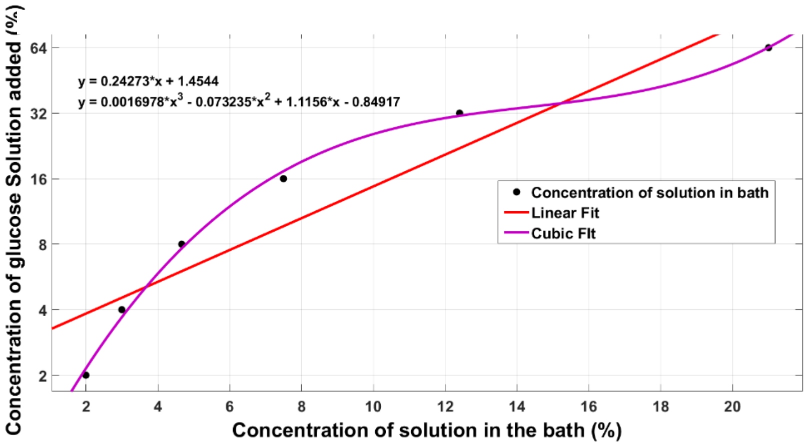

Figure 5-9: Plot of theoretical concentration of the solution in the bath after the addition of each of the samples.

Samples of interferometric signals continuously recorded for 10 seconds at a sampling frequency of 100kHz yields 20 interferograms (10 due to stretching of fibre stretcher and 10 dues to the relaxation of it). Due to the lash back of fibre during the relaxation of the fibre stretcher, fibre stretcher relaxation results in nonuniform OPD and hence only the interferograms generated by the stretching of fibre stretcher are considered for examination. The stretching interferogram samples for the different concentrations of glucose solutions are then processed and the change in phase values computed. Figure 5-10 shows the plot of sensors' phase data. A linear fit to the data shows a positive change in phase for increasing glucose solution concentration. For each sensor, the data plotted in Figure 5-10 comprises of 6 sets of data (1 set each for the 6 glucose solution samples) and each data set contains results from the processing of 10 stretching interferograms.

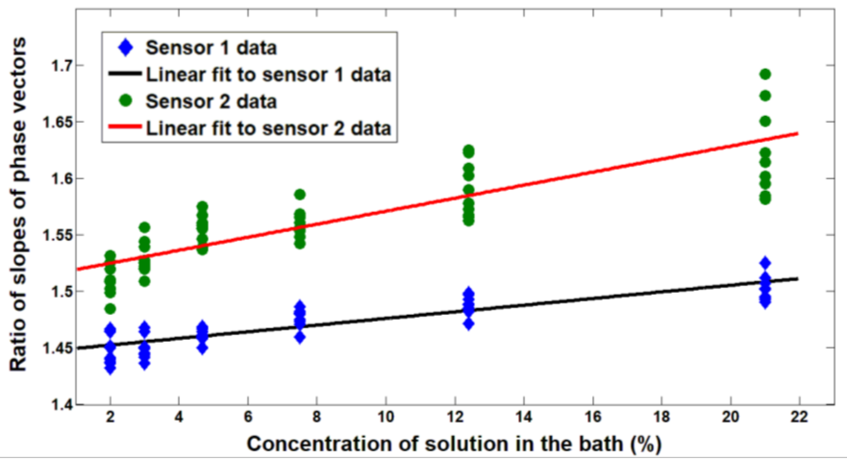

Figure 5-10: Plot of tapered sensor data

The median of the sensors' phase data sets shown in Figure 5-10 is calculated and plotted against the theoretical glucose solution concentration with error bars, as shown in Figure 5-11. The refractive index of a glucose solution changes linearly with its concentration and hence the sensitivity of the sensors is estimated from the slope of linear fits applied to the sensors' data. Linear fits yielded a sensitivity of ~(3.0±1.4)e-7/ppm for TS1 and ~(5.2±2.3)e-7/ppm for TS2. A discussion on the results from the ethanol and glucose sensing experiments is presented in the following section.

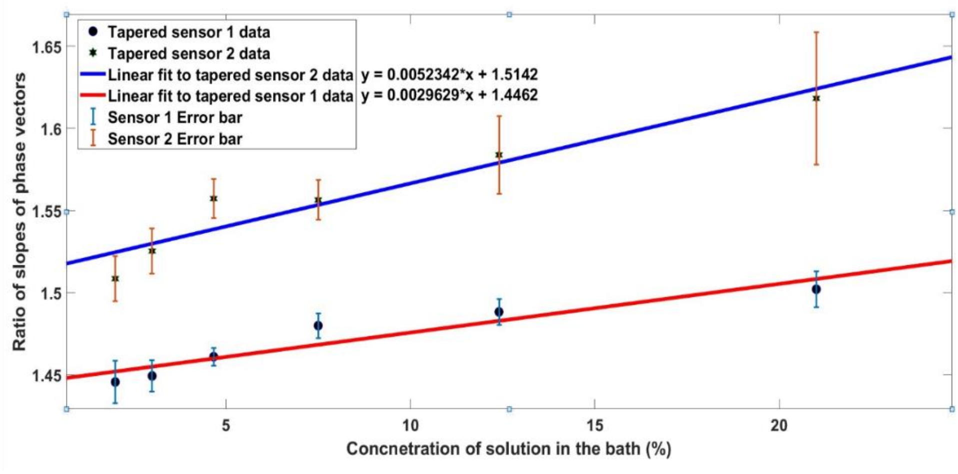

Figure 5-11: Plot of sensor data for glucose sensing experiment

5.5 Discussion

From the theory sections of Chapters 4 and 5, it can be seen that, the tapered sensors are used for sensing applications based on; the interaction of the cladding modes with the external environment and as well as the evanescent field power loss due to effects like absorption and scattering. In the two experiments presented in this chapter, the two different sensing methodologies are demonstrated. While in the case of ethanol sensing, the interaction of the ethanol vapours with the cladding modes induce a change in phase of the sensor's spectral fringes, in the case of glucose sensing, evanescent wave absorption results in the reduction of sensor's spectral intensity in addition to the interaction of cladding modes with the glucose solution.

In reference to the ethanol sensing experiment, one can find the data points beyond the 60th minute to deviate largely from the ideal exponential behaviour. This behaviour can be observed in the tapered sensor's phase change plots in this chapter as well as the previous one. As the ethanol molecules evaporate from the 98% ethanol solution, the concentration of the residual water increases changing the overall ethanol solution concentration. This decelerates or causes variations in the ethanol evaporation as observed beyond the 60th minute.

The data points in Figure 5-8 (A) appear scattered more than the data points in Figure 5-8 (B). However, on a closer inspection of the figures, one may find that the range of the sensor in Figure 5-8 (A) is ~0.09, which is lower than the ~0.16 range of sensor in Figure 5-8 (B). Thus, the datapoints in Figure 5-8 (A) appear more scattered because of the reduced range.

The reduction in fringe visibility of sensors when immersed in the glucose solution necessarily need not mean the total lack of cladding modes' interference with the fundamental mode. In Figure 5-7, spectral fringes are visible in a section of the tapered sensor spectrum corresponding to the 3% glucose solution. Due to effects like scattering and absorption, the number of cladding modes interfering with the fundamental mode reduces, resulting in the reduced spectral fringe visibility.

In the case of glucose sensing experiment, the sensors can be seen to effectively detect the 1% change in concentration i.e., the concentration change from 2% to 3%. From Equation (4-2), the FSR is inversely proportional to the refractive index difference and the taper length. Sensitivity has been shown to increase with refractive index difference [21] and should also increase with the taper length. Thus, overall sensitivity should increase with decreasing FSR, a trend previously noted in [22]. From Figure 5-5 (B) and (C), the TS1 has an FSR of 28nm which is greater than the 15nm FSR of the TS2. The marginally higher sensitivity and the reduced deviation to range % of the TS2 can thus be attributed to its lower FSR.

5.6 Conclusion

Multiple tapered sensors were simultaneously interrogated by interferometric illumination using short-scan interferometry. Efficacy of the system was demonstrated by sensing changes in both liquid and gaseous medium. While glucose solution was used as a stimulant for aqueous medium, ethanol vapour was used as a gaseous stimulant.

Unlike interrogation using OSA and the previously demonstrated heterodyning techniques [11]–[14] that do not permit the interrogation of more than one interferometric sensor, the interrogation system shown in Figure 5-1 demonstrated its ability to simultaneously interrogate two tapered sensors in a single scan of the interferometer. The rate of change of phase of the two tapered sensors subjected to investigation in an environment of rising ethanol vapour concentration was measured to be ~(26±12)e-3/min and ~(29±10)e-3/min.

When the tapered sensors were immersed in the liquid medium, their fringe visibility reduced considerably. Reduction in fringe visibility hampers interrogation using optical spectrum analysers, spectrometers, etc which rely on spectral fringes for information on the measurement medium. By interferometric illumination of the sensors, the change in phase induced by the changing glucose concentration measured was found to be ~(3.0±1.4)e-7/ppm and ~(5.2±2.3)e-7/ppm for sensor 1 and sensor 2 respectively. Tapered sensor 2 with an FSR lower than that of the sensor 1 was found to have better sensitivity.

Simultaneous interrogation of multiple tapered sensors without spectral overlap was thus demonstrated. Each of the tapered sensors can be used to simultaneously sense varied parameters. Interrogation system used in this work can be further expanded to accommodate a number of sensors and the number of sensors that can be interrogated in a single scan is limited only by factors like the optical power of the source, the number of photodiodes and data acquisition card channels, coupler losses, etc.

Through Chapters 3-5, the capability and efficacy to interrogate one or multiple sensors of a given sensor class by interferometric illumination has been demonstrated successfully. By combining the techniques from the previous experimental chapters, simultaneous interrogation of multiple sensors from multiple sensor classes is investigated in the next chapter.

5.7 References

[1] B. H. Lee *et al.*, 'Interferometric Fiber Optic Sensors', *Sensors*, vol. 12, no. 12, pp. 2467–2486, Feb. 2012, doi: 10.3390/s120302467.

[2] Y. Tian, W. Wang, N. Wu, X. Zou, and X. Wang, 'Tapered Optical Fiber Sensor for Label-Free Detection of Biomolecules', *Sensors*, vol. 11, no. 12, pp. 3780–3790, Mar. 2011, doi: 10.3390/s110403780.

[3] J. Miller *et al.*, 'Biconically Tapered Fiber Optic Probes for Rapid Label-Free Immunoassays', *Biosensors*, vol. 5, no. 2, pp. 158–171, Apr. 2015, doi: 10.3390/bios5020158.

[4] R. Sivacoumar, M. Vinoth, and Z. C. Alex, 'P1.1.3 Tapered Optical Fiber BioSensor for Testosterone Detection', *AMA Service GmbH, P.O. Box 2352, 31506 Wunstorf, Germany*, 2012, doi: 10.5162/imcs2012/p1.1.3.

[5] D. Tiwari, K. Mullaney, S. Korposh, S. W. James, S.-W. Lee, and R. P. Tatam, 'An ammonia sensor based on Lossy Mode Resonances on a tapered optical fibre coated with porphyrin-incorporated titanium dioxide', *Sensors and Actuators B: Chemical*, vol. 242, pp. 645–652, Apr. 2017, doi: 10.1016/j.snb.2016.11.092.

[6] Y. L. Hoo, W. Jin, H. L. Ho, D. N. Wang, and R. S. Windele, 'Evanescent wave gas sensing using microstructure fibre', 2001, pp. 8–9, doi: 10.1109/CLEOPR.2001.968008.

[7] R. Orghici, U. Willer, M. Gierszewska, S. R. Waldvogel, and W. Schade, 'Fiber optic evanescent field sensor for detection of explosives and CO2 dissolved in water', *Applied Physics B*, vol. 90, no. 2, pp. 355–360, Feb. 2008, doi: 10.1007/s00340-008-2932-7.

[8] K. Q. Kieu and M. Mansuripur, 'Biconical Fiber Taper Sensors', *IEEE Photonics Technology Letters*, vol. 18, no. 21, pp. 2239–2241, Nov. 2006, doi: 10.1109/LPT.2006.884742.

[9] S. H. Girei, A. A. Shabaneh, P. T. Arasu, S. Painam, and M. H. Yaacob, 'Tapered multimode fiber sensor for ethanol sensing application', in *2013 IEEE 4th International Conference on Photonics (ICP)*, Melaka, Malaysia, Oct. 2013, pp. 275–277, doi: 10.1109/ICP.2013.6687137.

[10] S. W. Harun, K. S. Lim, C. K. Tio, K. Dimyati, and H. Ahmad, 'Theoretical analysis and fabrication of tapered fiber', *Optik - International Journal for Light and Electron Optics*, vol. 124, no. 6, pp. 538–543, Mar. 2013, doi: 10.1016/j.ijleo.2011.12.054.

[11] D. A. Jackson, A. D. Kersey, M. Corke, and J. D. C. Jones, 'Pseudoheterodyne detection scheme for optical interferometers', *Electronics Letters*, vol. 18, no. 25–26, p. 1081, 1982, doi: 10.1049/el:19820740.

[12] P. A. S. Jorge, 'Fiber modal Michelson interferometers with coherence addressing and heterodyne interrogation', *Opt. Eng*, vol. 47, no. 4, p. 044401, Apr. 2008, doi: 10.1117/1.2903089.

[13] Yu-Lung Lo and Chin-Ho Chuang, 'New synthetic-heterodyne demodulator for an optical fiber interferometer', *IEEE J. Quantum Electron.*, vol. 37, no. 5, pp. 658–663, May 2001, doi: 10.1109/3.918578.

[14] E. Velosa, C. Gouveia, O. Frazao, P. A. S. Jorge, and J. M. Baptista, 'Digital Control of a White Light Interrogation System for Optical Fiber Interferometers', *IEEE Sensors J.*, vol. 12, no. 1, pp. 201–206, Jan. 2012, doi: 10.1109/JSEN.2011.2144579.

[15] S. Yin, P. B. Ruffin, and F. T. S. Yu, Eds., *Fiber optic sensors*, 2nd ed. Boca Raton, FL: CRC Press, 2008.

[16] B. D. Gupta, H. Dodeja, and A. K. Tomar, 'Fibre-optic evanescent field absorption sensor based on a U-shaped probe', *Optical and Quantum Electronics*, vol. 28, no. 11, pp. 1629–1639, Nov. 1996, doi: 10.1007/BF00331053.

[17] A. V. Malinin, A. A. Zanishevskaja, V. V. Tuchin, Yu. S. Skibina, and I. Y. Silokhin, 'Photonic crystal fibers for food quality analysis', Brussels, Belgium, Jun. 2012, p. 842746, doi: 10.1117/12.924096.

[18] X. Zhou, W. Zhou, W. Tang, and X. Ye, 'Eliminating polarization-induced fading in interferometric fiber optic arrays by modulation', Beijing, China, Aug. 1998, pp. 174–179, doi: 10.1117/12.318155.

[19] A. D. Kersey, M. J. Marrone, and M. A. Davis, 'Polarisation-insensitive fibre optic Michelson interferometer', *Electronics Letters*, vol. 27, no. 6, p. 518, 1991, doi: 10.1049/el:19910325.

[20] K. B. Rochford and S. D. Dyer, 'Demultiplexing of interferometrically interrogated fiber Bragg grating sensors using Hilbert transform processing', *Journal of Lightwave Technology*, vol. 17, no. 5, pp. 831–836, May 1999, doi: 10.1109/50.762900.

[21] A. Ben Khalifa, 'Ultrahigh sensitivity with different taper geometries of thin-core fiber modal interferometer for refractive index sensing', *Opt. Eng.*, vol. 58, no. 02, p. 1, Feb. 2019, doi: 10.1117/1.OE.58.2.026109.

[22] W. B. Ji, Y. C. Tan, B. Lin, S. C. Tjin, and K. K. Chow, 'Nonadiabatically Tapered Microfiber Sensor With Ultrashort Waist', *IEEE Photon. Technol. Lett.*, vol. 26, no. 22, pp. 2303–2306, Nov. 2014, doi: 10.1109/LPT.2014.2353931.

Chapter 6

Simultaneous Interrogation of Multiple Sensor Classes by Interferometric Illumination

6.1 Introduction

Existing interrogation schemes capable of simultaneously interrogating multiple sensor classes costs tens of thousands of euros. Expanding on the earlier experiments detailed in Chapters-3-5, this chapter investigates the capability and the efficacy of a low cost interferometric interrogation scheme for interrogating multiple sensor classes. Apart from the low cost, the atypical interrogation scheme under study also offers the advantage of an increased sensor density when compared against its counterparts.

Fibre optic sensor (FOS) is an optical fibre in which the light guided within is modulated in response to an external stimulus. FOS types include grating based sensors, distributed sensors, interferometric sensors, etc. The grating based sensors and distributed sensors are primarily sensitive to strain and temperature and interferometric sensors are sensitive to refractive index changes, temperature, strain, etc.

Owing to high sensitivity of grating based sensors to temperature and interferometric sensors to refractive index changes, for simultaneous sensing of refractive index and temperature changes, a combination of grating based and interferometric sensors have been used in the past [1]–[11]. In the previous studies involving multi-class sensor interrogation ([1]–[11]), an optical spectrum analyser (OSA) was used to interrogate the combination of sensors. In an OSA with a monochromator, the peak power reduces with increasing resolution which tends to reduce the signal to noise ratio. Due to the overlapping spectrum of the sensors when using an OSA, the effect of refractive index and temperature changes on the sensor had to be individually first studied and a complex matrix of sensitivities then developed to estimate the effect of the combination of physical forces acting on the sensor. Another limitation of interrogation using OSA is that, the density of FBGs that can be multiplexed with a tapered sensor is limited due to the overlapping spectra of the sensors.

In previous works [1]–[10], at the most one FBG sensor was interrogated in conjunction with an interferometric sensor for reasons already stated above. Work described in this chapter investigates the feasibility of simultaneous interrogation of an array of FBG sensors and an interferometric tapered sensor without spectral overlap. Also, when compared to interrogation using OSA, interferometry offers advantages such as multiplexablity (Fellgett advantage) [11], high throughput (Jacquinot advantage) [12], Connes advantage [13].

In a typical interferometric interrogation scheme, the sensors are first illuminated and the light from the sensors are then interrogated using an interferometer, as a result cascading of a tapered sensor and an FBG sensor gives rise to spectral overlap. Unlike the typical interferometric interrogation schemes, in the experiment described in this chapter, a broadband interferogram is first generated using an all-fibre Michelson interferometer scanning through an optical path difference (OPD) of ~13mm and the generated broadband interferogram is then used to illuminate sensors. As a result of this arrangement without spectral overlap, the broadband interferogram modulated by the tapered sensor and the superposed interferograms reflected by the FBGs can be independently processed to obtain the measurement sensor values.

6.2 Theory

The two types of sensors used in the experimental work are an FBG sensor and a tapered sensor. The theory pertaining to the FBG sensor has been covered in Chapter-3 and the theory pertaining to the tapered sensor based sensing has been covered in Chapter-4. The reader is requested to follow and consider the theories for the sensors discussed in this study from the above mentioned chapters.

6.3 Experimental Setup

The experimental setup for multiparameter sensing is shown in Figure 6-1. The all-fibre interferometer is constructed in Michelson interferometer configuration and in the interferometer, a piezo fibre stretcher (PFS) (Evanescent Optics, Fiber Stretcher, Model 916B) is used for generating an optical path delay (OPD) of ~13mm. OPD generated by the stretcher varies logarithmically with the frequency of the signal used to modulate the stretcher. Hence for generating a maximum OPD, a low-frequency signal of ~1Hz with a 5V DC offset is used for modulating the stretcher.

Single mode fibre based interferometer is susceptible to random changes to the state of polarization (SOP) of the interfering optical beams. Randomly changing SOP results in fringe visibility variations and fading of the interferometric signal. In the experimental setup, Faraday rotor mirrors FRM1 and FRM2 are used to reduce polarization induced fading in the fibre, as previously demonstrated [14], [15].

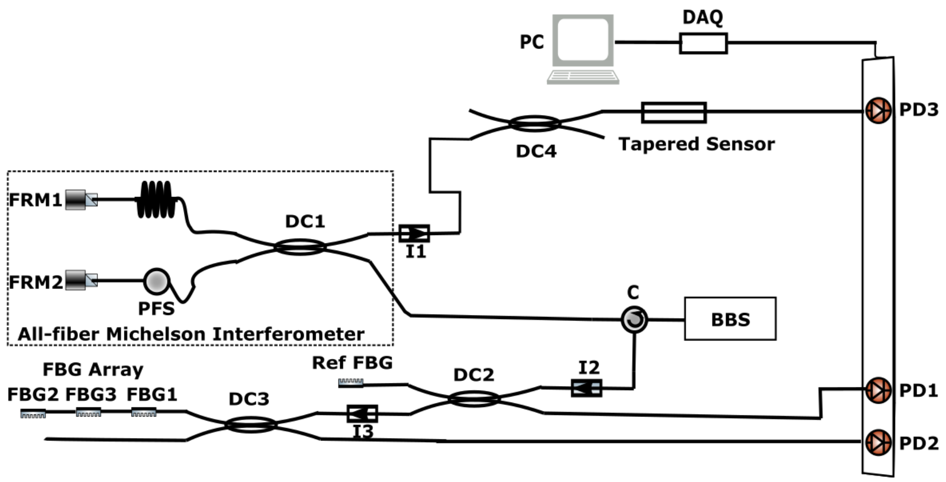

Figure 6-1: Experimental setup

The interferometer is illuminated with a broadband source (BBS) centred at ~1550nm via Circulator (C). The circulator directs the light from the source into the interferometer, and the interferogram generated by the interferometer towards the sensors. While directional couplers (DC) are used to illuminate the various arms of the interferometer, isolators I1, I2 and I3 prevent back reflections from coupling into other sensor arrays.

Photodiodes, PD1, PD2 and PD3 (Newfocus 2053) are used to convert the light reflected by reference FBG and the light transmitted by TFOS into electrical signals. A high-speed data acquisition card (DAQ) (NI-USB-6341) was used to record 1M samples of interferometric signals on to a computer at 100kHz such that, each fringe was sampled 4 times.

The measurement scheme is based on subtraction of measurement interferograms from the broadband source interferogram. Hence, an FBG (Ref FBG) with a centre wavelength of ~1550nm is used for referencing the measurement tapered sensor and measurement FBG array comprising of FBG1 (~1550nm), FBG2 (~1560nm) and FBG3(~1566nm). All the FBGs used had an FWHM of ~0.19nm.

For demonstrating the efficacy of the system, the tapered sensor was used to monitor ethanol evaporation at room temperature and FBG2 was used to sense temperature changes from 30^0C to 100^0C in 10^0C increments. The tapered sensor measurement setup described in Chapter-4 was used in this experiment as well and a Periodically Poled Lithium Niobate (PPLN) oven was used for subjecting FBG2 to the above-mentioned temperature changes. The interferometric test data was recorded in 15-minute intervals and throughout the test duration, the reference FBG was stabilised on a Peltier module.

6.4 Results

The fibre stretcher when modulated goes through a cycle of stretching and relaxation. Thus, a single pulse of stretcher modulating signal yields two interferograms corresponding to the stretching and relaxation phases of the stretcher. Whilst the stretching of the fibre is gradual, the relaxation is abrupt due to the backlash from the stretched fibre. As a result of the non-uniform OPD sampling during fibre relaxation, only the interferograms corresponding to the stretching phase of the fibre stretcher are considered for sensor measurements.

A single stretching movement of the fibre stretcher in the experimental setup shown in Figure 6-1 yields a broadband interferogram transmitted through the tapered sensor and interferograms with narrowband reflected by the reference FBG and the measurement FBG array. Sample of the interferograms are shown in Figure 6-2. The effect of addition of multiple narrowband interferograms from the FBGs can be seen in Figure 6-2 (C). A fast Fourier transform (FFT) of the interferograms yields additional spectral content due to the non-linear motion of the fibre stretcher and uneven delay sampling as shown in Figure 6-3.

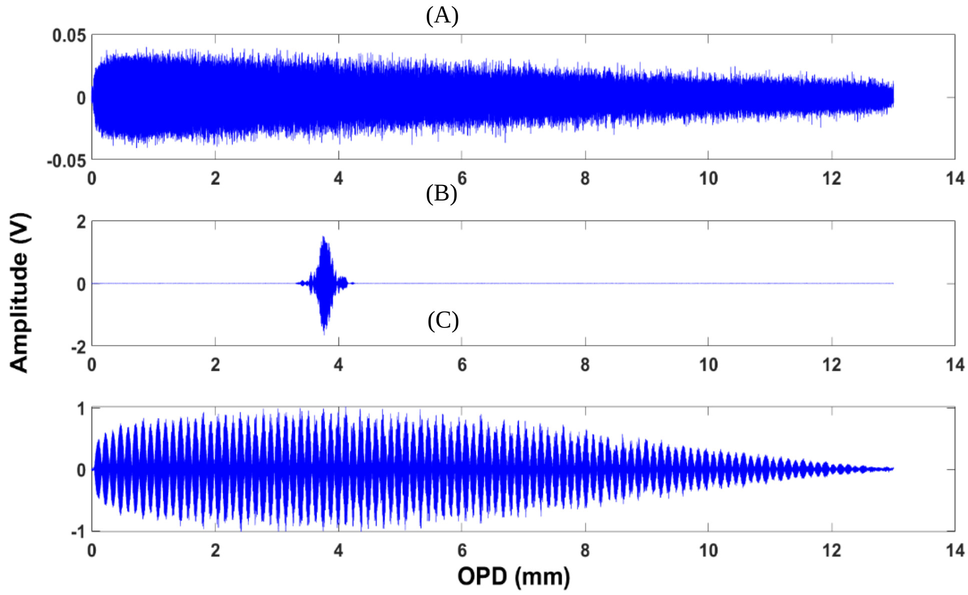

Figure 6-2: (A) - Reference FBG interferogram, (B) - Tapered sensor interferogram and (C) - Measurement FBG array interferogram

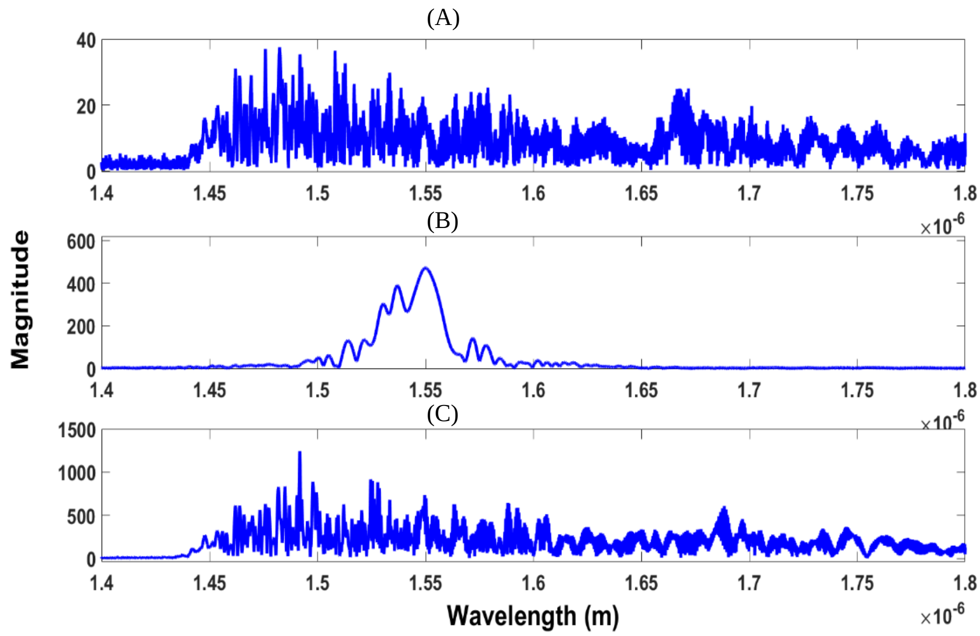

Figure 6-3: Uncalibrated spectrum of: (A) - Reference FBG, (B) - Tapered sensor and (C) - Measurement FBG array

The additional spectral content is removed by uniform OPD sampling or delay calibration using Hilbert transform processing technique (HTT). Non-linear OPD sampling prior to delay calibration and the uniform OPD sampling after delay calibration is evident from the plot of reference FBG phase vectors shown in Figure 6-4. After delay calibration, the additional spectral content is removed and sensors' spectra become clearly resolvable as shown in Figure 6-5.

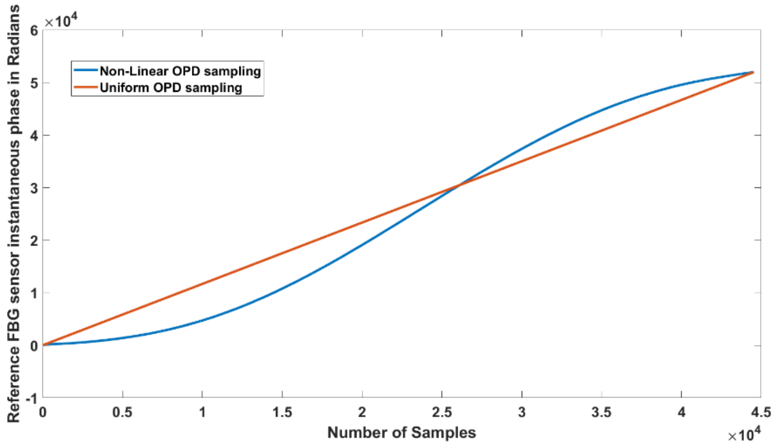

Figure 6-4: Temporal phase vector plot of reference FBG

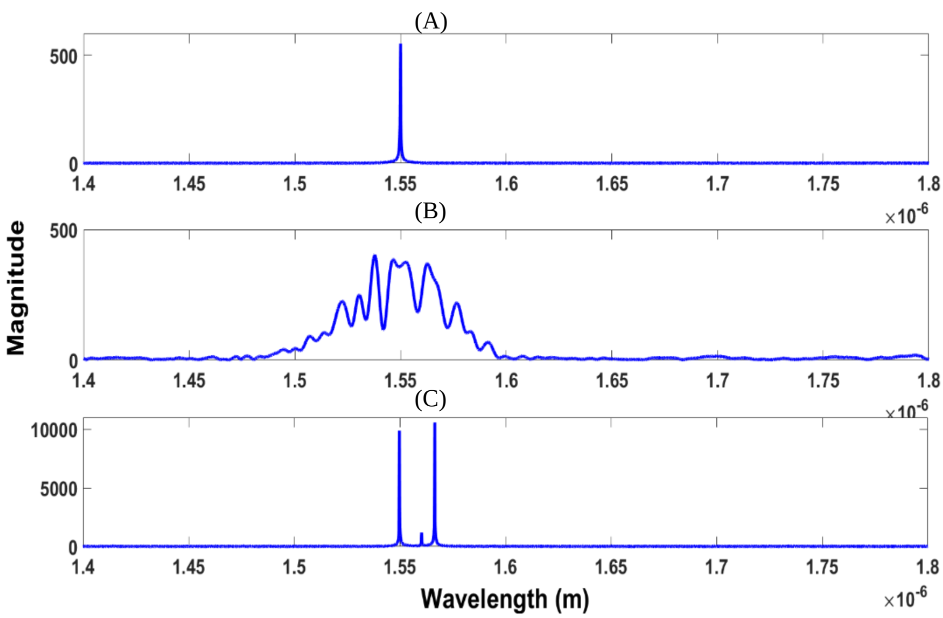

Figure 6-5: Calibrated spectrum of: (A) - Reference FBG, (B) - Tapered sensor and (C) - Measurement FBG array

Temporal phase vectors for the reference FBG and the tapered sensor are obtained from their respective delay calibrated interferograms and temporal phase vectors for the FBGs in the measurement array are obtained after individually segmenting them. The plot of reference and measurement sensors' phase vectors is shown in Figure 6-6.

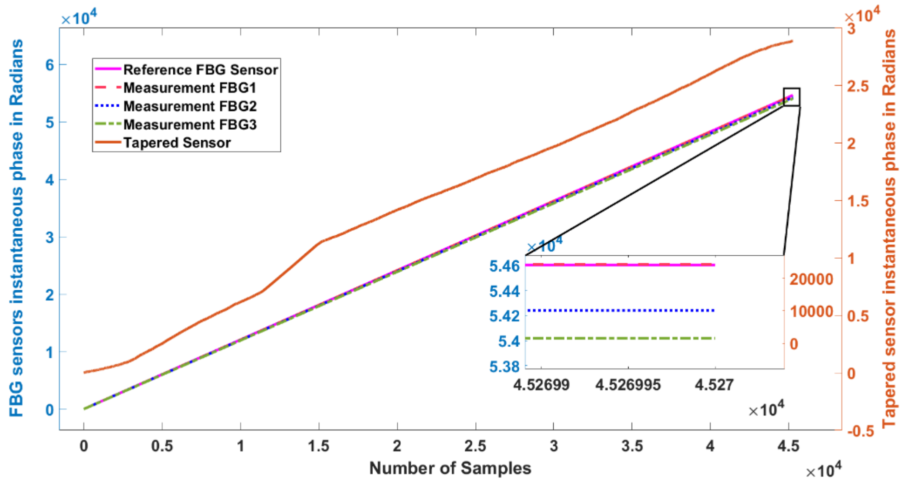

Figure 6-6: Temporal phase vectors of reference and measurement sensors

The tapered sensor's phase changes with changing ethanol concentration and FBG2's wavelength increases with increasing temperature. The tapered sensor's phase at various instances of ethanol vapour concentration is calculated by comparing the slopes of the reference FBG phase vectors against its temporal phase vector slopes. The peak reflecting wavelengths of the FBGs in the measurement array is obtained by comparing their temporal phase vectors with that of the reference FBG.

8 sets of 10 second long interferometric data were recorded at 15 minute intervals. This presents with 160 interferograms as each interferometric scan generates interferograms from both the stretching and the relaxation of the stretcher. As discussed in the previous experimental chapters, due to the non-uniformity in the fibre relaxation, only the 80 interferograms from the stretching of the fibre is considered.

The FBG and the tapered sensor values using each of the 80 interferograms are then calculated. This yields 10 data points for each instance i.e., 10 tapered sensor values each for the 0th minute, 15th minute, etc, and likewise 10 FBG sensor values for 30^{0}C, 40^{0}C, etc. The median of the data for each instance is calculated and plotted as shown in Figure 6-7 below.

(A)

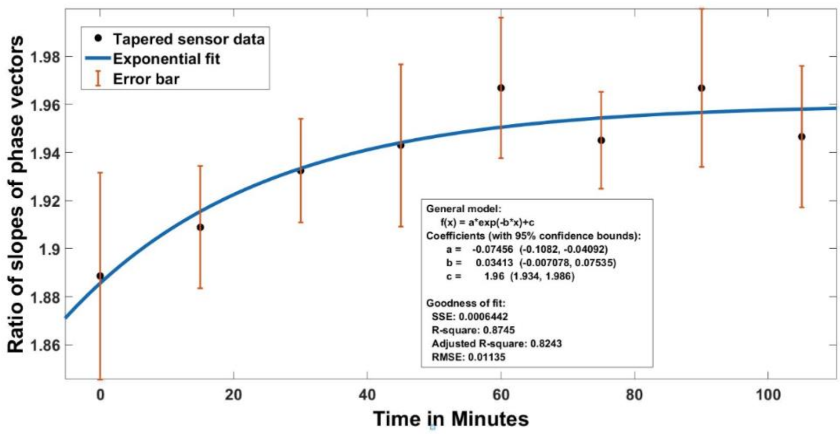

(B)

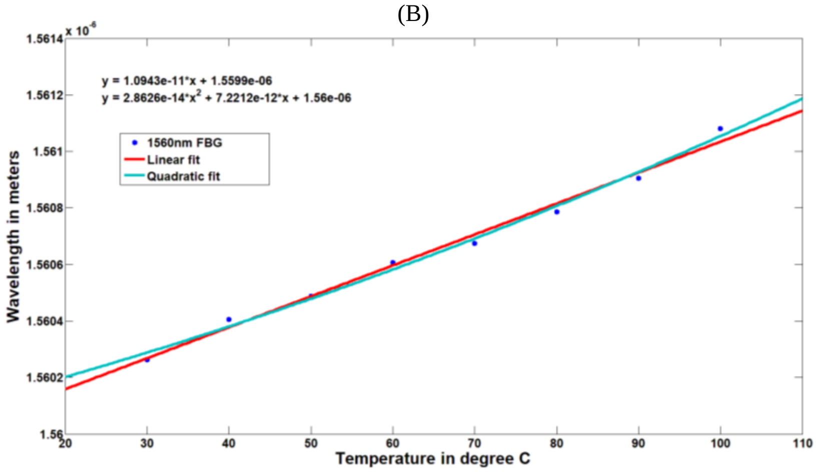

Figure 6-7: (A) - Tapered sensor and (B) - FBG2 sensor measurement data

The plot of tapered sensor data as a function of time and the plot of FBG2 data as a function of temperature is shown in Figure 6-7 (A) and Figure 6-7 (B) respectively. Owing to the exponential nature of ethanol evaporation as already discussed in Chapter-4, an exponential fit was applied to the tapered sensor data. Linear and quadratic fits were applied to the measurement FBG sensor data to determine the rate of wavelength change with temperature. The plot of residuals of the linear and exponential fit is shown in Figure 6-8.

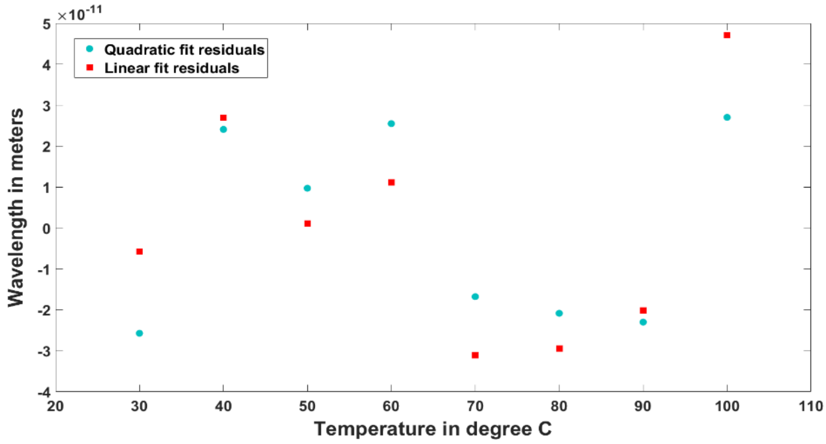

Figure 6-8: Plot of linear and quadratic fit residuals to FBG data

From the exponential fit, the rate of change of the tapered sensor's phase for changing ethanol vapour concentration was estimated to be ~(34±34)e-3/min. A linear fit to the FBG data yielded a resolution of ~(11±1)pm/^{0}C. To ascertain the quadratic nature of the FBG, the linear and quadratic fit residuals are plotted. The sum of squares of the residuals was found to be 5.33e-21 and 3.95e-21 for the linear fit and quadratic fit respectively. Thus, the linear fit demonstrates a larger deviation from the ideal when compared to the quadratic fit. From this, we can say that the FBG's response is closer to a quadratic behaviour as previously demonstrated by Flockhart [16].

The FBG2 sensor and the tapered sensor results from multiple trials have been presented in Table 6-1. All the trials can be seen to yield comparable results. Range of peak wavelength change of all the FBG sensors for all the trials is listed in Table 6-2. The range of wavelength change of the sensors not subjected to the temperature test can be seen to be lower than that of the sensor subjected to the temperature test. Discussion on the results obtained from the above experiment is presented in the following section.

Table 6-1: FBG and tapered sensor results

Trial Number	FBG2 resolution pm/^{0}C	Rate of tapered sensor phase change (/min)
1	11±1	34±34e-3
2	10±1	35±34e-3
3	10±2	36±34e-3

Table 6-2: Range of FBG sensors' wavelength changes

Trial Number	Range of FBG Sensors in pm		
	FBG1	FBG2	FBG3
1	68.80	818.73	134.72
2	92.91	691.31	83.21
3	72.75	608.02	120.60

6.5 Discussion

In the plot of the recalibrated spectrum in Figure 6-5, the FBG2(~1560nm) can be seen to be of lower amplitude than the other two sensors. This lower amplitude is due to the pinching of the fibre on the edge of the PPLN fibre oven. As an FBG reflects back its characteristic narrowband of light along the same path as the illuminating light, the attenuation due to the pinching of the fibre has a compounded effect resulting in the lower spectral amplitude as seen. To prevent the FBG3 from suffering the attenuation, the sensor has been placed ahead of FBG2 which can be seen in Figure 6-1. As the pinching is beyond the grating on the sensor it does not have any detrimental effect on the measurement process.

In the plot of the tapered sensor response seen in Figure 6-7 (A), the datapoints beyond the 60th minute can be seen to deviate from the ideal exponential behaviour. The reason for this behaviour is attributed to the reducing ethanol concentration and the increasing water concentration in evaporating solution as already discussed in the discussion section of the previous experimental chapter. The larger deviation beyond the 60th minute and the reduced number of data points has resulted in a larger uncertainty value of ±34 when compared to the previous value of ~±10 in Chapters 4 and 5.

The linear and quadratic fits to the FBG sensor data presented accuracy (deviation from ideal fit) values of ±39.08pm and ±26.3pm for the respective fits. Though the lower quadratic deviation tends towards the FBG's quadratic nature, the deviation is higher than the ~±12pm maximum deviation reported in Chapter-3. For a closer inspection, the bar plot of the FBG peak values is plotted and shown below for reference.

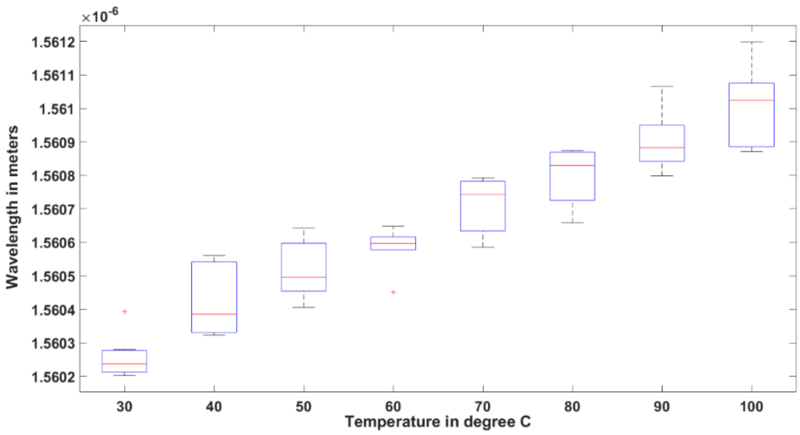

Figure 6-9: Bar plot of FBG sensor data

From the bar plot, a non-uniformity in the data spread and data outliers can be seen. The non-uniformity in the data spread can be attributed to the temperature gradient on the PPLN oven compounded by the variations in the fibre stretcher's performance. By using a mix of mean and median central tendency measures based on the merit of data spread, the quadratic deviation dropped to ±15pm, close to the value reported in Chapter-3.

Extremities in FBG peak values due to random vibrations can often influence the range and hence for closer examination of the performance of the FBGs that were not subjected to the temperature test, the standard deviation of the peak values for the test duration were obtained as given in the Table 6-3.

Table 6-3: Standard deviation of FBG peak values

Trial Number	Standard deviation in pm	
	FBG1	**FBG3**
1	19.15	42.87
2	34.65	27.30
3	24.89	39.37

Trials 1 and 3 were conducted at the same time of the day on consecutive days and Trial 2 at a different time on a different day. The tests that were conducted at the same time of the day can be seen to have similar results. Due to the prolonged duration of the test, variations can be attributed to the uncontrolled testing environment (centralised heating system, movement of personnel, etc.), changing room temperatures, and a temperature gradient along the metallic optical test table, and not due to errors in the system or data processing which would have produced a systematic variation in the results.

6.6 Conclusion

Using short-scan interferometric illumination, multi-sensor class interrogation was demonstrated by simultaneous interrogation of a tapered sensor and an FBG array without spectral overlap. The novel configuration of the interferometer used in this work demonstrated the interrogation of an increased density of the multiplexed FBG sensors i.e., interrogation of multiple FBG sensors of varied wavelengths when compared to the previous instances of multi-class sensor interrogation ([1]–[10]) where, at the most one FBG sensor was interrogated in conjunction with the tapered sensor. The efficacy of the system was demonstrated by sensing refractive index changes using a tapered optical fibre sensor while simultaneously sensing temperature changes using an FBG from an array of FBGs.

Overlap of the tapered sensor and the FBG array spectra was avoided by interferometric illumination of the sensors and by using individual photodiodes for each of the sensor measurement arms/arrays. Tests yielded results similar to the results reported in Chapter-3 for FBG and Chapter-4 and 5 for the tapered sensor. The tapered sensor's response was found to be ~(35±34)e-3/min across multiple trials and the FBG was found to have a linear sensitivity of ~(10±1)pm/^{0}C across multiple trials which is typical of an FBG inscribed on a silica fibre which has a sensitivity of ~8-12pm/^{0}C.

Simultaneous interrogation of multiple tapered optical fibres has been reported in Chapter-5 and simultaneous interrogation of multiple FBG arrays has been reported in Chapter-3. Thus, the dexterity of the interrogation scheme to demodulate multiple sensors of similar kind and multiple sensors of diverse kinds has been demonstrated.

The number of sensor arrays or sensing arms is dependent on several factors like source power, required resolution, signal to noise levels, number of photodiodes and the number of channels on the DAQ. As the OPD generated by the fibre stretcher drops off with increasing scan frequency, a low-frequency signal was used to modulate the stretcher for generating maximum OPD. By increasing the OPD, the system resolution can be further improved, and the multiplexed sensor density can be increased. However, the stretching of the fibre to a larger extent could result in wavelength changes due to dispersion arising from the changes in the fibre's strain-optic coefficient.

6.7 References

[1] Q. Yao *et al.*, ‘A sandwich fiber sensor for simultaneous measurement of RI and temperature’, in *2017 16th International Conference on Optical Communications and Networks (ICOCN)*, Wuzhen, Aug. 2017, pp. 1–4, doi: 10.1109/ICOCN.2017.8121353.

[2] Y. Cao, C. Zhao, and Z. Tong, ‘All fiber sensor based on Mach-Zehnder interferometer for simultaneous measurement of temperature and refractive index’, *Optoelectronics Letters*, vol. 11, no. 6, pp. 438–443, Nov. 2015, doi: 10.1007/s11801-015-5175-y.

[3] F. Ahmed, V. Ahsani, A. Saad, and M. B. G. Jun, ‘Bragg Grating Embedded in Mach-Zehnder Interferometer for Refractive Index and Temperature Sensing’, *IEEE Photonics Technology Letters*, vol. 28, no. 18, pp. 1968–1971, Sep. 2016, doi: 10.1109/LPT.2016.2580582.

[4] X. Zhang, W. Peng, Y. Liu, and Q. Yu, ‘Core-offset-based fiber Bragg grating sensor for refractive index and temperature measurement’, *Optical Engineering*, vol. 52, no. 2, p. 024402, Feb. 2013, doi: 10.1117/1.OE.52.2.024402.

[5] C. R. Liao, Y. Wang, D. N. Wang, and M. W. Yang, ‘Fiber In-Line Mach–Zehnder Interferometer Embedded in FBG for Simultaneous Refractive Index and Temperature Measurement’, *IEEE Photonics Technology Letters*, vol. 22, no. 22, pp. 1686–1688, Nov. 2010, doi: 10.1109/LPT.2010.2079924.

[6] X. Yu, X. Chen, D. Bu, J. Zhang, and S. Liu, ‘In-Fiber Modal Interferometer for Simultaneous Measurement of Refractive Index and Temperature’, *IEEE*

Photonics Technology Letters, vol. 28, no. 2, pp. 189–192, Jan. 2016, doi: 10.1109/LPT.2015.2489559.

[7] Yanfang Lu, Changyu Shen, Chuan Zhong, Debao Chen, Xinyong Dong, and Jinhui Cai, 'Refractive Index and Temperature Sensor Based on Double-Pass M–Z Interferometer With an FBG', *IEEE Photonics Technology Letters*, vol. 26, no. 11, pp. 1124–1127, Jun. 2014, doi: 10.1109/LPT.2014.2315804.

[8] Q. Yao *et al.*, 'Simultaneous measurement of refractive index and temperature based on a core-offset Mach–Zehnder interferometer combined with a fiber Bragg grating', *Sensors and Actuators A: Physical*, vol. 209, pp. 73–77, Mar. 2014, doi: 10.1016/j.sna.2014.01.017.

[9] Y. Bai, B. Yin, C. Liu, S. Liu, Y. Lian, and S. Jian, 'Simultaneous Measurement of Refractive Index and Temperature Based on NFN Structure', *IEEE Photonics Technology Letters*, vol. 26, no. 21, pp. 2193–2196, Nov. 2014, doi: 10.1109/LPT.2014.2350023.

[10] M. Zhou, X. Dong, and X. Liu, 'Simultaneous measurement of temperature and refractive index with thin-core fiber MZI containing fiber Bragg grating', in *2017 16th International Conference on Optical Communications and Networks (ICOCN)*, Wuzhen, Aug. 2017, pp. 1–3, doi: 10.1109/ICOCN.2017.8121291.

[11] P. Fellgett, 'Spectromètre interférentiel multiplex pour mesures infra-rouges sur les étoiles', *Journal de Physique et le Radium*, vol. 19, no. 3, pp. 237–240, 1958, doi: 10.1051/jphysrad:01958001903023700.

[12] P. Jacquinot, 'New developments in interference spectroscopy', *Reports on Progress in Physics*, vol. 23, no. 1, p. 267, 1960.

[13] J. Connes and P. Connes, ‘Near-Infrared Planetary Spectra by Fourier Spectroscopy. I. Instruments and Results’, *J. Opt. Soc. Am.*, vol. 56, no. 7, pp. 896–910, Jul. 1966, doi: 10.1364/JOSA.56.000896.

[14] X. Zhou, W. Zhou, W. Tang, and X. Ye, ‘Eliminating polarization-induced fading in interferometric fiber optic arrays by modulation’, Beijing, China, Aug. 1998, pp. 174–179, doi: 10.1117/12.318155.

[15] A. D. Kersey, M. J. Marrone, and M. A. Davis, ‘Polarisation-insensitive fibre optic Michelson interferometer’, *Electronics Letters*, vol. 27, no. 6, p. 518, 1991, doi: 10.1049/el:19910325.

[16] G. M. H. Flockhart *et al.*, ‘Quadratic behavior of fiber Bragg grating temperature coefficients’, *Applied Optics*, vol. 43, no. 13, p. 2744, May 2004, doi: 10.1364/AO.43.002744.

Chapter 7

Summary and Conclusion

7.1 Research outcome

Objectives achieved

The fundamental goal of this research was to overcome the various limitations of existing interrogation schemes for the different optical fibre sensors and facilitate the development of a one of a kind low-cost interrogation system capable of interrogating multiple sensor classes simultaneously. The broader research goal was broken down into smaller goals which were: to implement an interrogation system capable of interrogating multiple arrays of multiple FBG sensors, to demonstrate high-resolution interferometric interrogation of one or more tapered sensors in a single scan, to interrogate multiple fibre optic sensor classes simultaneously. Results presented in Chapters 3-6 not only demonstrate the achievement of the set research goals but also the dexterity, scalability, and sensing capabilities of the developed novel all-fibre interferometric interrogation system.

Fourier transform spectroscopy (FTS) is a typical implementation of interferometry for spectroscopic measurements. Intra-grating and inter-grating measurements of wavelength division multiplexed (WDM) FBGs and the tapered sensors' highly sensitive phase measurements have been performed by exploiting the advantages of FTS such as multiplexablity (Fellgett advantage) [1], high throughput (Jacquinot advantage) [2] and spectral accuracy (Connes advantage) [3] using an all-fibre Michelson interferometer. Unlike the conventional interferometric interrogation systems, the interferometer constructed was first illuminated with a broadband superluminescent diode and then by filtering of the low coherence interferogram generated, multiple sensors of the same class and sensors of multiple classes were simultaneously interrogated.

Mechanical scans in FTS results in spectral degradation due to uneven delay sampling. HTT has been shown to perform accurate calibration of the delay, thereby negating the effects of spectral degradation arising from the mechanical scans. Resolution of an FTS based measurement scheme is directly proportional to the OPD of the interrogating interferometer. However, by heterodyne detection, high-resolution sensor measurements have been obtained for shorter scans of the interferometer.

High-resolution measurements were possible using HTT which involved the comparison of the measurement temporal phase vectors against the temporal phase vector of the high coherence reference interferogram. The configuration of the all-fibre interferometer did not allow the use of an additional source with larger coherence length for referencing. As a result, an FBG was used to filter a high coherence interferogram from the low coherence interferogram generated by the interferometer for referencing the sensor measurements.

Conclusion and summary of results

Chapter-1 provides an overview of the later chapters. The problem statement and the research goals formulated to address the problem statement are presented in the first chapter also along with the research methodology. The concepts of interference, optical fibres, optical fibre sensors, interferometry and the start-of-the-art in fibre optic sensors' interrogation is reviewed in Chapter-2.

By interferometric illumination, interrogation of multiple arrays of WDM FBG sensors is demonstrated in Chapter-3. High-resolution intra-grating and inter-grating measurements using a combination of FTS and HTT are obtained for a short scan (~13mm) of the interferometer. The designed interrogation system was found to be efficient in demodulating FBGs with similar wavelengths across multiple arrays. Whilst being interrogated by the all-fibre interferometer, measurement FBGs when subjected to a temperature change from 30^0C through 150^0C were found to have a temperature sensitivity of ~9pm/^{0}C. The OPD generated by the fibre stretcher was found to drop off with increasing frequency and hence, the scanning frequency of the fibre stretcher was determined to be a factor limiting the density of the sensors multiplexed in an array.

By modifying and applying the interrogation scheme from Chapter-3 to interrogate a tapered sensor, in Chapter-4 high-resolution interrogation of a tapered sensor, is investigated. The sensing system was characterised by using an evanescent wave based sensor to monitor the changing ethanol vapour concentration. To simulate measurements performed using an OSA, the changes to the sensor's spectral phase were calculated from the FFT of the sensor's interferograms.

The spectral phase change measurements of ~(67±35)e-3/min, ~(54±18)e-3/min ~(68±35)e-3/min were obtained using the spectral fringes of the sensor. For measurements using the temporal fringes, a ratio of the reference FBG and the sensor temporal phase vector slopes are obtained. The measurements from the processing of the temporal fringes of the sensor ~(36±10)e-3/min, ~(28±12)e-3/min and ~(36±18)e-3/min) were found to have a accuracy ~15% superior to the ones obtained using the spectral fringes.

In due course of the experiments, the label-free tapered sensor's fringes were found to revert to its initial state upon the removal of the phase change inducing stimulus thereby highlighting the sensor's reusability.

The interrogation setup used in Chapter-4 is extrapolated to simultaneously interrogate multiple tapered sensors in Chapter-5, thus overcoming the major limitation of interrogation using OSA which does not permit simultaneous interrogation of multiple tapered sensors due to spectral overlap. When two tapered sensors were used for monitoring ethanol evaporation, the measurement results of ~(26±12)e-3/min and ~(29±10)e-3/min for the two sensors were found to be in concurrence with the findings from Chapter-4. When submersed in an environment whose refractive index is close to that of the cladding of a tapered sensor, the sensor's fringe visibility reduces. Reduced fringe visibility limits sensor interrogation using OSA as measurements using OSA is based on the sensor's spectral fringes.

The efficacy of the all-fibre interrogation system under reduced spectral fringe visibility is demonstrated by using two tapered sensors to sense changes to glucose solution concentration in a bath. Sensors with different FSRs were chosen to demonstrate the interrelationship between sensor's sensitivity and its FSR. For the addition of serially diluted glucose solutions with concentration from 2% through 64%, the sensitivities of the sensors were found to ~(3.0±1.4)e-7/ppm and ~(5.2±2.3)e-7/ppm. The sensor with lower FSR was found to have a marginally higher resolution than the sensor with a larger FSR demonstrating the inverse proportionality between the sensor's sensitivity and FSR.

Chapter-6 combines the FBG interrogation method demonstrated in Chapter-3 and tapered sensor interrogation method demonstrated in Chapter-4 to interrogate a combination of FBG arrays and a tapered sensor. By interferometric illumination of the sensors and by using separate photodiodes for the sensor classes, the simultaneous interrogation of the different sensors was possible without spectral overlap. One of the FBGs from the sensor array was used for temperature sensing and the tapered sensor was used for sensing changing ethanol vapour concentration. When subjected to a change in temperature from 30^0C to 100^0C in 10^0C increments, the FBG sensor's wavelength shifted by ~800pm and a linear fit to the data provided a sensitivity of ~(11±1)pm/^{0}C. From the test data, the quadratic nature of the FBG was also demonstrated. The tapered sensor's phase was found to change exponentially with the changing ethanol vapour concentration at the rate of ~(35±34)e-3/min. Multiple trials yielded comparable results. The tapered sensor sensitivity to ethanol was found to be in concurrence with the findings from Chapters 4 and 5.

7.2 Scope for improvements and future investigations

Multi-sensor interrogation capabilities of a portable all-fibre interrogation system have been demonstrated in this thesis. Unlike the bulk-optic setups, the all-fibre system is less susceptible to vibrations and presents a potential for use in field studies and commercialization.

The tapered sensors used in this work were manually fabricated on a fibre coupler workstation (E-TEK FCPW-2000) with limited control over the taper characteristics. Sophisticated automated systems can offer better control over the tapering process whereby a sensor with desired parameters can be precisely fabricated.

The path delay generated by the fibre stretcher used in this work varies logarithmically with the frequency of the modulating signal. To maximise the OPD, low-frequency scans (~1Hz) were used. Alternative fibre based arrangements with a faster scanning rate and a larger stretching capability can further improve the system resolution.

Lasers with coherence length in the range of tens of centimetres provide measurement resolutions far higher than that provided by an FBG. Addition of a second high coherent source can provide high-resolution measurements and self-referencing capability for FBG sensing, but the additional source will result in a spectral overlap when used with tapered sensors. However, unlike a Mach–Zehnder interferometer configuration which permits the use of two sources, the interferometer setup used in this study is in Michelson configuration and is illuminated with the source via a circulator which permits the use of only one source. Alternatively, by replacing the reference FBG in the existing setup with an ultra-narrowband transmission filter, the measurement accuracy can be improved.

7.3 References

[1] P. Fellgett, ‘Spectromètre interférentiel multiplex pour mesures infra-rouges sur les étoiles’, *Journal de Physique et le Radium*, vol. 19, no. 3, pp. 237–240, 1958, doi: 10.1051/jphysrad:01958001903023700.

[2] P. Jacquinot, ‘New developments in interference spectroscopy’, *Reports on Progress in Physics*, vol. 23, no. 1, p. 267, 1960.

[3] J. Connes and P. Connes, ‘Near-Infrared Planetary Spectra by Fourier Spectroscopy. I. Instruments and Results’, *J. Opt. Soc. Am.*, vol. 56, no. 7, pp. 896–910, Jul. 1966, doi: 10.1364/JOSA.56.000896.

Appendix-A

Single mode fibre field equations

The derivation for the following equations has been discussed in detail in Chapter-2 of this document. For a stepwise derivation, the reader is referred to Section 2.7.2 of Chapter-2. The electric field vector $\boldsymbol{E}$ and magnetic field vector $\boldsymbol{H}$ have three components each. The components are interdependent as per Maxwell's equations. The following treatment to Maxwell's equations is closely based on, *Fundamentals of optical fibers* by J. A. Buck. The Maxwell's equations in the integral form given in Section 2.3.2 of Chapter-2 can be expressed in differential form as follows,

$$\nabla \times \boldsymbol{E} = -\frac{\partial \boldsymbol{B}}{\partial t} \tag{A - 1}$$

$$\nabla \times \boldsymbol{H} = \frac{\partial \boldsymbol{D}}{\partial t} \tag{A - 2}$$

$$\nabla . \boldsymbol{D} = 0 \tag{A - 3}$$

$$\nabla . \boldsymbol{B} = 0 \tag{A - 4}$$

The longitudinal components are expressed as independent components and the transverse components can be expressed in terms of the longitudinal components. Longitudinal components are given by (derivation given in Chapter-2, Section 2.7.2),

$$E_z = \begin{cases} AJ_l(k_T r) e^{jl\phi} e^{-j\beta z}, & r < a \\ CK_l(\gamma r) e^{jl\phi} e^{-j\beta z}, & r > a \end{cases} \tag{A - 5}$$

$$H_z = \begin{cases} BJ_l(k_T r)e^{jl\phi}e^{-j\beta z}, & r < a \\ DK_l(\gamma r)e^{jl\phi}e^{-j\beta z}, & r > a \end{cases}$$

(A - 6)

By the substitution of longitudinal components into Maxwell's equations, the transverse components for the core modes are expressed in terms of the longitudinal components as follows,

$$E_r = \frac{i}{{k_T}^2}\left[\beta\ \frac{\partial E_z}{\partial r} + \mu_0 \frac{\omega}{r}\frac{\partial H_z}{\partial \phi}\right]$$

(A - 7)

$$E_\phi = \frac{i}{{k_T}^2}\left[\frac{\beta}{r}\ \frac{\partial E_z}{\partial \phi} - \mu_0 \omega \frac{\partial H_z}{\partial r}\right]$$

(A - 8)

$$H_r = \frac{i}{{k_T}^2}\left[\beta\ \frac{\partial H_z}{\partial r} - \varepsilon_0 n^2 \frac{\omega}{r}\frac{\partial E_z}{\partial \phi}\right]$$

(A - 9)

$$H_\phi = \frac{i}{{k_T}^2}\left[\frac{\beta}{r}\ \frac{\partial H_z}{\partial \phi} - \varepsilon_0 n^2 \omega \frac{\partial E_z}{\partial \phi}\right]$$

(A - 10)

The cladding mode components are obtained by replacing k_T in the above equations with γ.

Appendix-B

Piezo fibre stretcher specification

The list of specifications of the piezo fibre stretcher is attached below as given by the manufacturer Evanescent Optics INC. The logarithmic dependency between piezo voltage and the modulating frequency is shown in Figure B-1.

Model 914-1 Piezo Controller and 916 Assembly

Serial no. 1377

Front panel connections/indicator:

-916 Piezo Out. Connect one end of the cable (provided) to the input jack labeled 916. Connect the other end to the jack mounted on the piezo assembly.

-916 BNC. The shell of the BNC is grounded. Factory set to give full swing of piezo voltage (0 to +150V) for an input signal of 0 to +5volts.

-915 BNC and 915 Piezo Out N/C

Fig.1 shows the signal response of the driver voltage applied to the piezo. Input 0 to +5 volts sinusoidal.

-Green LED. Dimly lit LED indicates controller power ON. Brightly lit LED indicates piezo is connected and the controller is driving below the current limit. If LED blinks on and off the controller has reached the current limit and is intermittently supplying current to the piezo as well as indicating a fault in the system. This should only happen if the piezo becomes shorted or resistive.

Rear Panel connections:

- AC line plug. An AC cord is provided. Unit set for 220-230V AC input.

-Ground post.

Fiber stretch:

Serial no. 5846-1

Fiber Type: SMF-28

Number of windings: 86

Fiber stretch (optical path measurement) for 0 to +150 volts= 5mm

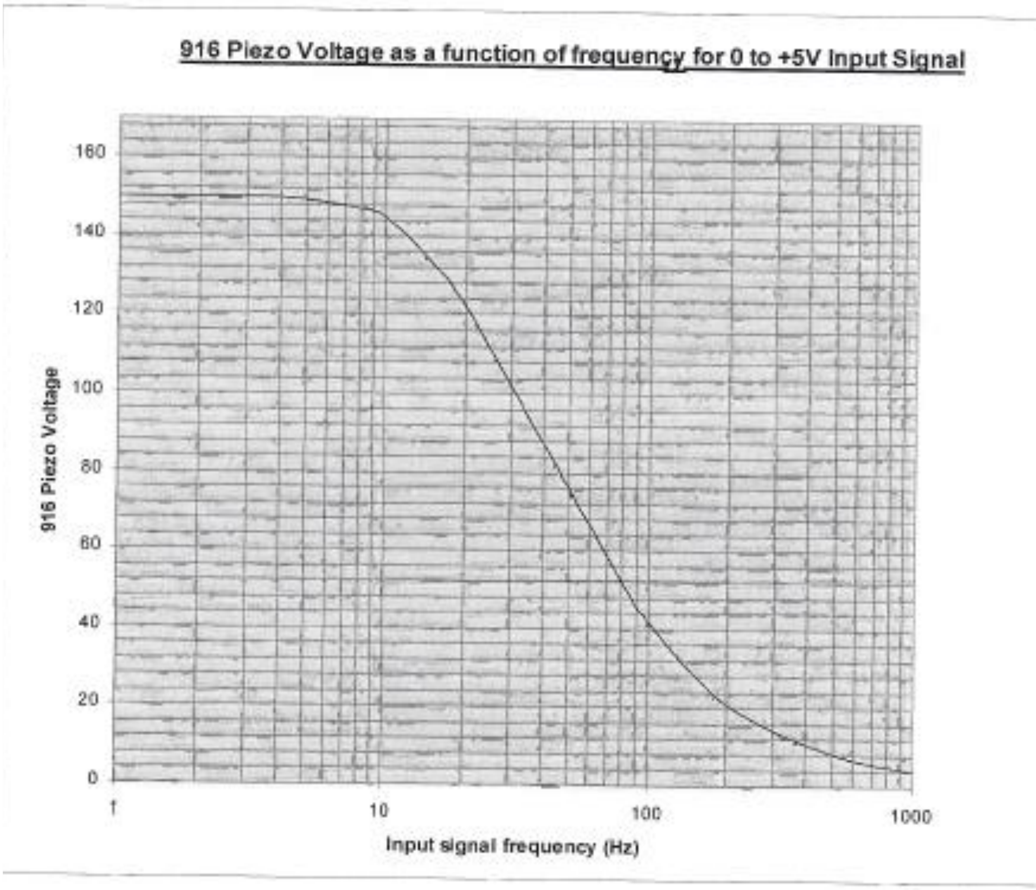

Figure B-1: Plot of piezo voltage vs frequency of the modulating signal